

CCI
BIOMASS

PRODUCT VALIDATION & ALGORITHM SELECTION REPORT
YEAR 1
VERSION 1.0

DOCUMENT REF:	CCI_BIOMASS_PVASR_V1
DELIVERABLE REF:	D2.1 -PVASR
VERSION:	1.0
CREATION DATE:	2019-02-01
LAST MODIFIED	2019-04-04

1 Document Authorship

	NAME	FUNCTION	ORGANISATION	SIGNATURE	DATE
PREPARED	T. Le Toan M. Planells A. Bouvet S. Mermoz	WP Leader	CESBIO		
PREPARED	R. Lucas		Aberystwyth Uni.		
PREPARED	C. Ryan		Edinburgh Uni.		
PREPARED	C. Pathe		FSU Jena		
PREPARED	C. Dubois		FSU Jena		
PREPARED	J. Carreiras		Sheffield Uni.		
PREPARED	S. Bowers		Edinburgh Uni.		
PREPARED	H. Kay		Aberystwyth Uni.		
PREPARED	P. Bunting		Aberystwyth Uni		
PREPARED					
VERIFIED	S. Quegan	Science Leader	Sheffield University		
APPROVED					

2

3 Document Distribution

ORGANISATION	NAME	QUANTITY
ESA		

4

5 Document History

VERSION	DATE	DESCRIPTION	APPROVED
0.1	2019-02-01	First draft version	
1.0	2018-11-15		

6

7 Document Change Record (from Year 1 to Year 2)

VERSION	DATE	DESCRIPTION	APPROVED
		First draft version	

8

9

10

	Ref	CCI Biomass Product Validation and Algorithm Selection Report		
	Issue	Page	Date	
	1.0	3	10.02.2019	

11 [Table of Contents](#)

12 **List of figures 5**

13 **List of tables 11**

14 **Symbols and acronyms..... 12**

15 **1 Introduction 14**

16 **1.1 Purpose and scope 14**

17 **2 Biomes evaluations 16**

18 **2.1 Wet tropics/subtropics and mangroves 16**

19 2.1.1 Forest Inventory (plot) data 16

20 2.1.2 AGB estimated from airborne LiDAR 18

21 2.1.3 Comparison with existing AGB Maps 29

22 2.1.4 Summary – Wet Tropics 31

23 **2.2 Dry Tropics and Subtropics 32**

24 2.2.1 Site comparisons (Mozambique, Tanzania and South Africa)..... 32

25 2.2.2 Inventory Data Comparisons (South Africa, Australia, Guinea Bissau and Kenya). 33

26 2.2.3 Summary - Dry Tropics and Subtropics 38

27 **2.3 Temperate and Boreal Biomes 39**

28 2.3.1 Inventory data comparison (Finland)..... 39

29 2.3.2 Influence of land cover class 41

30 2.3.3 Summary - Boreal/Temperate Forests..... 42

31 **2.4 Mangroves 42**

32 **3 Generic Issues 48**

33 **3.1 The Water Cloud Model..... 48**

34 3.1.1 Model Overview..... 48

35 3.1.2 Vegetation..... 49

36 3.1.3 At-Ground Surface States and Structures 50

37 3.1.4 At Surface and Within Volume Environmental Conditions 51

38 **3.2 Topographic Effects 51**

39 **3.3 Conversion of GSV to AGB 52**

40 **3.4 Knowledge of AGB Distributions Globally 53**

	Ref	CCI Biomass Product Validation and Algorithm Selection Report		
	Issue	Page	Date	
	1.0	4	10.02.2019	

41	3.5	High Biomass Forests.....	54
42	3.6	Summary and Considerations	57
43	4	<i>Improvements to the GlobBiomass Algorithm.....</i>	57
44		Improving Soil Moisture component	58
45	4.1.....		58
46	4.2	Inundated forests - Temporal trend of ALOS-2 PALSAR-2 backscatter	64
47	4.3	Direct retrieval of AGB using the WCM.	68
48	4.3.1	The WCM	68
49	4.3.2	Formulation of the WCM for Volume Retrieval	69
50	4.3.3	Reformulation of the WCM for AGB retrieval.....	72
51	4.4	Summary.....	72
52	5	<i>Complementary Approaches.....</i>	73
53	5.1	Backscatter decreasing trend.....	73
54	5.2	Use of L-Band VOD	76
55	5.3	Use of Structural information as a New Global Indicator	80
56	5.4	Use of canopy height for mangroves.....	91
57	6	<i>Conclusions and recommendations.....</i>	98
58	7	<i>Appendix 1.....</i>	99
59	8	<i>References</i>	102
60			
61			

	Ref	CCI Biomass Product Validation and Algorithm Selection Report		
	Issue	Page	Date	
	1.0	5	10.02.2019	

62 LIST OF FIGURES

63 Figure 1: Comparison of the AGB estimated using the BIOMASAR algorithm from a) 38 plots
64 located near Tapajos, Brazil, b) 36 plots located in Colombia and Thailand National forest
65 inventory plots (of 0.1 ha) from c) 2004-2010 and d) 2010-2015..... 18
66 Figure 2: The location of study sites in (a) French Guiana and (b) Gabon. 19
67 Figure 3: AGB estimated from a) LiDAR and b) the GlobBiomass algorithm for Lope, Gabon
68 (from 0 (blue) to 450 Mg ha⁻¹ (red)), c) the frequency distribution and d) comparison between
69 the two AGB products. 20
70 Figure 4: AGB derived over Mabounie, Gabon from a) LiDAR and b) the BIOMASAR product
71 (from 0 Mg ha⁻¹ (blue) to 450 Mg ha⁻¹; red), c) the frequency distribution and d) comparison
72 between the two AGB products. 21
73 Figure 5: AGB derived over Mondah, Gabon from a) LiDAR and b) the BIOMASAR product, c)
74 the frequency distribution and d) comparison between the two AGB products. Blue areas in
75 a) correspond to the non-forest areas. Colour code ranges from 0 (blue) to 450 (red) Mg ha⁻¹
76 22
77 Figure 6: AGB derived over Rabi, Gabon from a) LiDAR and b) the BIOMASAR product, c) the
78 frequency distribution and d) comparison between the two AGB products. Blue areas in a)
79 correspond to the non-forest areas. Colour code ranges from 0 (blue) to 450 (red) Mg ha⁻¹.
80 23
81 Figure 7: AGB derived from Nouragues, French Guyana using a) LiDAR and b) the BIOMASAR
82 product, c) the frequency distribution and d) comparison between the two AGB products.
83 Blue areas in a) correspond to the non-forest areas and values range from 0 (blue) to 450
84 (red) Mg ha⁻¹. 25
85 Figure 8: AGB derived over Paracou, French Guyana from a) LiDAR and b) the BIOMASAR
86 product. Blue areas in a) correspond to the non-forest areas and values range from 0 (blue)
87 to 450 (red) Mg ha⁻¹. 26
88 Figure 9: Quantitative assessment of the residuals stratified by reference AGB range.
89 Comparison between LiDAR-based and GlobBiomass AGB maps over a) Lope, b) Mabounie,
90 c) Mondah and d) Rabi in Gabon and e) Nouragues and f) Paracou in French Guiana (note the
91 top left hand plot had AGB < 100t/ha). 27
92 Figure 10: Comparison of the AGB estimated from LiDAR and using the GlobBiomass
93 algorithm (GlobBiomass map) for 4 sites in Gabon and 2 sites in French Guiana (Paracou and
94 Nouragues). 29
95 Figure 11: AGB product for the DRC (Xi et al., 2017) highlighting tree-grass savannahs (darker
96 blues; ~20-50 Mg ha⁻¹), swamp forests (light blue; ~230-300 Mg ha⁻¹) and humid tropical

	Ref	CCI Biomass Product Validation and Algorithm Selection Report		
	Issue	Page	Date	
	1.0	6	10.02.2019	

97 forests (yellow-orange; AGB of ~300-400 Mg ha⁻¹ and > 400 Mg ha⁻¹ (red); b) mean estimates
98 of AGB for savannahs, swamp forest and humid forests as well as Miombo and Shrub forest;
99 and c) comparison between LiDAR-derived AGB and the AGB mapped using the algorithm of
100 Xu et al. (2017). d) shows the GlobBiomass map e) the map of difference in AGB and f) the
101 pixel-by-pixel scatterplot and histograms comparison of the GlobBiomass and Xu et al. (2017)
102 AGB maps..... 30
103 Figure 12. GlobBiomass AGB product for a) Kruger NP (South Africa), b) Lake Urema-Central
104 Mozambique and c) central Mozambique (highlighting overestimation in agricultural
105 (treeless) areas) and d) Kuger NP, South Africa (where banding is evident in the AGB map).
106 34
107 Figure 13: Comparison of in situ AGB and GlobBiomass AGB for a) southern African savannas
108 (SEOSAW network (<https://seosaw.github.io>) and b) low biomass forests and c) all forests in
109 Australia (TERN/Ausplots). 35
110 Figure 14: Scatterplot of reference (plot data measured in 2007-2012) vs mapped (100-m
111 GlobBiomass 2010) above-ground biomass in Guinea-Bissau. A) n = 282, reference vs.
112 GlobBiomass 2010 observations; B) n = 163, reference vs. GlobBiomass 2010 observations;
113 C) n = 18, each point representing the average of at least five *in situ* measurements at 0.1-
114 degree scale against the corresponding pixel average from GlobBiomass 2010. The dashed
115 line represents perfect agreement and the red line a linear fit to those observations. The
116 error bars around each observation show half the standard deviation (SD) in the reference
117 (horizontal) and mapped (vertical) datasets. 37
118 Figure 15 Scatterplot of reference (233 plot data measured in 2014-16) vs mapped (100-m
119 GlobBiomass 2010) above-ground biomass in Kenya. 38
120 Figure 15. a) Location of forest. Comparison of 2010 Globbiomass map and NFI plots for
121 Finland..... 40
122 Figure 16. Comparison of 2010 GlobBiomass map and NFI plots for different regional forest
123 centres in Finland. 41
124 Figure 17: LiDAR-derived CHM for mangroves at the mouth of a) the Leichardt River and b)
125 West Alligator River (Kakadu NP), Australia. In both cases, the taller (> 10-15 m) forests are
126 dominated primarily by *Rhizophora stylos*. c) Differences in ALOS PALSAR L-band HH and HV
127 backscatter as a function of canopy height and dominant species, Leichhardt River and d) the
128 trend in L-band HH and HV backscatter as a function of dominant species type, West Alligator
129 River, as observed from AIRSAR data acquired at different incidence angles in 1996 and 2000.
130 43
131 Figure 18: The enhanced L-band HH backscatter (white) following commercial harvesting,
132 Matang Mangrove Forest Reserve (MMFR), Malaysia. Note the gradual return of the
133 backscatter to pre-disturbance levels. 44

	Ref	CCI Biomass Product Validation and Algorithm Selection Report		
	Issue	Page	Date	
	1.0	7	10.02.2019	

134 Figure 19: a) RapidEye image (near infrared, red edge and blue in RGB) of mangroves along
135 the West Alligator river showing taller mangroves dominated by *Rhizophora stylosa* (orange)
136 and shorter mangroves dominated by *Sonneratia alba* (seaward; olive) and *Avicennia marina*
137 (landward, yellow). b) The corresponding GlobBiomass AGB map showing lower AGB
138 retrieved for the taller *Rhizophora*-dominated mangroves. 45
139 Figure 20: a) The trend in L-band HH and HV backscatter prior to and following commercial
140 harvest of *Rhizophora*-dominated forests, MMFR, Malaysia. B). The correspondence between
141 the AGB estimated for 2010 using the BIOMASAR algorithm and from age-adjusted TanDEM-
142 X CHM..... 46
143 Figure 21: Estimates of AGB for the MMFR, Malaysia, based on a) the GlobBiomass algorithm
144 and b) the age-adjusted TanDEM-X CHM. 47
145 Figure 22: Influence of the slope on the GSV estimation for test sites in the boreal (British
146 Colombia, Siberia) and the temperate (Poland, Thuringia) biomes. 52
147 Figure 23: a) Forest structural formation classification of Australia (Scarth et al., 2019), based
148 structural formations adapted from Australia’s National Vegetation Information System
149 (NVIS), c) the Australian Plant Biomass Library (APBL) showing plot locations, c) continental
150 AGB estimated using ICESAT-derived height and cover estimates within a machine learning
151 algorithm (trained using 50 % of samples from the APBL) and d) the correspondence in the
152 AGB estimated using ML and the APBL (50 % of samples). 55
153 Figure 24: Comparison of the AGB map generated using the BIOMASAR algorithm and
154 machine learning using ICESAT-derived height and cover for a) northern New South Wales
155 indicating areas of overestimation for low and open woodland and b) Western Australia,
156 showing over and underestimation in areas harvested for timber. 56
157 Figure 25: Comparison between the AGB estimated from in situ data (APBL) and the
158 BIOMASAR algorithm. The correspondence between AGB and the product of canopy cover
159 (%) and height (m) is also indicated). 56
160 Figure 26: Proposed calibration sites for eWCM-sm in the dry tropics. Calibration sites (□)
161 combines two regional networks (SEOSAW and DRYFLOR) with data from 22 project partners.
162 At each site plots have already been established and data collected in the ALOS1 and 2
163 epochs. Green areas with AGB < 150 t/ha; yellow = arid; grey = wet tropics. Source:(Avitabile
164 et al., 2015). 60
165 Figure 27: Results of the application of the eWCM in southern Africa. Black dots show
166 observed σ_0 at calibration plots. The estimated contribution from the soil is shown in blue
167 and from vegetation in green, with the sum (σ_0) in red. Two features consistent with WCM
168 theory are the zero contribution of σ_{veg} at zero biomass and the decline in σ_{soil} with increasing
169 biomass. Source: (Gou, 2017). 61

	Ref	CCI Biomass Product Validation and Algorithm Selection Report		
	Issue	Page	Date	
	1.0	8	10.02.2019	

170 Figure 28: Model predictions of σ^0 for quintiles of biomass (0-200 tC/ha) and soil moisture
171 (0-100%). Source: (Gou, 2017) 61
172 Figure 29: Example of the application of the eWCM-sm over the Zambezi delta in Marrameu,
173 Mozambique using ALOS-1 HV data and ESA’s ECV soil moisture product. The soil moisture
174 correction is able to remove the banding visible with the eWCM is used with no soil moisture
175 correction. The AOI is 100 km N-S and 70 km E-W. Source: (Gou, 2017) 62
176 Figure 30: BIOMASAR Retrieval Principle 63
177 Figure 31: Temporal variation of σ_{gr0} 64
178 Figure 32 Left: PALSAR-2 composite showing striping effects. Right: Annual mosaics from
179 PALSAR/PALSAR-2 over a river area in the Colombian amazon showing the variability of
180 backscatter due to inundation of riparian vegetation..... 65
181 Figure 33. PALSAR-2 mosaic correction for a given pixel. The red dot corresponds to an
182 artificially high backscatter return. Red line is the temporal trend of the signal (excluding large
183 outliers), and the black lines correspond to twice the standard deviation. Note that the
184 backscatter return observed in the year 2015 is artificially high so it is corrected. However,
185 the large drop in backscatter return observed in 2017 is not corrected, because it is
186 potentially related to a disturbance event..... 66
187 Figure 34 Example of the early implementation of the method over the Amazon region. Left:
188 PALSAR-2 original mosaic. Right: PALSAR-2 corrected version (right)..... 67
189 Figure 35 Left: PALSAR mosaic 2007-10. Centre: PALSAR-2 original mosaic 2015-17. Right:
190 PALSAR-2 corrected mosaic 2015-17. Note that only artificially high backscatter returns
191 (compared to PALSAR mosaic) are corrected, while deforestation events (backscatter drop)
192 are not corrected..... 68
193 Figure 36: (Left) Left axis: Simulated HV backscatters versus AGB, plotted in green (with
194 attenuation from the vegetation) and cyan (without attenuation from the vegetation). Right
195 axis: Simulated attenuations at horizontal (blue) and vertical (red) polarizations, accounting
196 for the signal loss (in dB) due to the wave propagation forth and back. The uncertainties
197 related to wood density variations (3.5% around mean value of 0.58 g.cm⁻³) are represented
198 by the filled colour domains surrounding the curves. (Right): SAR backscatter at HV
199 polarization versus in situ above ground biomass (AGB) after the selection process. Twenty-
200 one savanna and 5 forest 1-ha field plots, acquired from the REDDAF project (Haeusler et al.,
201 2012), in 2011 in the Adamawa Province, Cameroon and in 2013 in the Central Province,
202 Cameroon, were added..... 74
203 Figure 37 (left) AGB estimates at 500m resolution, compared to (right) the LiDAR-derived
204 AGB map of Xu et al. (2017) at 100m resolution 76

	Ref	CCI Biomass Product Validation and Algorithm Selection Report		
	Issue	Page	Date	
	1.0	9	10.02.2019	

205 Figure 38: SMOS L-VOD plotted with respect to ALOS HV backscatter at low resolution over
206 the Congo basin (Left) and for each biome/ecosystem (Right). Various regression models (log,
207 exp and linear) were tested for relating VOD to SAR backscatter 77
208 Figure 39: SMOS VOD as a function of AGB in the DRC, as derived from the DRC map by Xu et
209 al. (2017). 78
210 Figure 40: Disaggregated SMOS L-VOD at 1 km resolution over the Congo Basin 79
211 Figure 41: Colour scheme and legend for the classification based on height and cover
212 categories placed at intervals of 2-5 m and 5 m thereafter and >10 % and 10 % thereafter.
213 81
214 Figure 42: Structural classification based on cross tabulation of the Hansen et al. (2013)
215 canopy cover and Simard et al. (2013) canopy height layers for a) the World, b) central Africa,
216 c) Amazonia and d) Peninsular Malaysia and Indonesia. The legend is shown in Figure 41.82
217 Figure 43: The association of forest structural classes in the Democratic Republic of Congo
218 (DRC) with AGB (estimated by Xu et al., (2017). Dense forests are associated with classes 58,
219 68, 78 (TC>90%, H>25-30 m; TC>90%, H>30-35 m, TC>90%, H>35-40 m), with these also
220 supporting a higher AGB. 83
221 Figure 44: An approach to establishing the relationship between AGB to tree cover (%),
222 canopy height (m), volume fraction and wood volumetric density..... 84
223 Figure 45: Sensitivity to Tree cover where the color denotes the forest height (left). On the
224 right with colour expressing different TC..... 85
225 Figure 46: AGB versus volumetric indicator TC(%) x H (m) 86
226 Figure 47: The correspondence between VOD (left) and AGB (right) and tree canopy cover
227 (TC, %) x canopy height (H, m) for a) the Congo Basin and b) globally. 86
228 Figure 48: Estimates of AGB generated a) globally and for b) South America and c) the Congo
229 Basin based on TC and H..... 87
230 Figure 49: AGB comparison between TCxH AGB map and the Xu et al. (2017) AGB map
231 obtained for the DRC..... 88
232 Figure 50. Land cover classification of selected 1 x 1° latitude/longitude tiles for a) Tasmania,
233 b) central north coastal Queensland, c) central Gabon and d) Perak State, Malaysia with e),
234 f), g) and h) representing the GlobBiomass AGB maps for 2010. Note that in Malaysia,
235 mangroves are depicted as one class but biophysical information is contained within the
236 attribute table..... 89
237 Figure 51. a) GlobBiomass estimate of AGB for Sydney NSW and the northern forests, b) the
238 difference in AGB estimated using the GlobBlomass product and through machine learning
239 (height and cover) and c) the FAO LCCS classification indicating areas of taller and denser
240 (closed canopy) forests (dark purple), with these typically associated with higher AGB in the
241 GlobBiomass product. 91

	Ref	CCI Biomass Product Validation and Algorithm Selection Report		
	Issue	Page	Date	
	1.0	10	10.02.2019	

242 Figure 52: The relationship between Hba and AGB (Mg ha-1) established at a global and
243 regional levels (Simard et al., 2019) 93
244 Figure 53: GMW mangrove baseline for 2010 and distribution of mangroves in longitude and
245 latitude (WGS-84; epsg:4326) (Bunting et al., 2010). 94
246 Figure 54: The correspondence between AGB estimated using the BIOMASAR algorithm
247 (GlobBiomass) and CHMs generated from Shuttle Radar Topographic Mission (SRTM)
248 interferometric SAR (Simard et al., 2019) a) across their global range (as mapped through the
249 GMW; Bunting et al., 2018) and for b) Australia, c) Indonesia, d) Malaysia, e) Papua New
250 Guinea, f) Gabon, g) Nigeria, h) Sierra Leone, i) the Democratic Republic of Congo, j) Brazil,
251 k) Columbia, l) Venezuela and m) French Guyana. 96
252 Figure 55: Comparison of field-based estimates of AGB (collected in 2010 and 2011 ;
253 Hamden et al., 2014) and AGB estimated in 2016 from TanDEM and 2010 using the
254 GlobBiomass algorithm. 98
255

	Ref	CCI Biomass Product Validation and Algorithm Selection Report		
	Issue	Page	Date	
	1.0	11	10.02.2019	

256 LIST OF TABLES

257 Table 1. Applicable documents..... 13

258 Table 2: Statistics in the comparison of AGB estimated from LiDAR (TropiSAR and AfriSAR

259 campaigns) and using the BIOMASAR algorithms. AGB is stratified into 4 classes: < 100 Mg

260 ha⁻¹, 100-200 Mg ha⁻¹, 200-300 Mg ha⁻¹, > 300 Mg ha⁻¹. For each class, N= number of pixels

261 (100m); E(B)= mean AGB from the LiDAR derived map in Mg ha⁻¹, E(^B)= mean AGB from

262 GlobBiomass in Mg ha⁻¹, E (Resi)= difference in Mg ha⁻¹. ¹mean LiDAR-derived AGB (Mg ha⁻¹);

263 ²mean GlobBiomass AGB (Mg ha⁻¹); ³AGB difference (Mg ha⁻¹). N represents the number of

264 100 m pixels. 28

265 Table 4: Correction factor for σ_{gr0} 64

266 Table 5.List of data layers for reclassification of the global landscape and informing retrieval

267 of AGB. 90

268 Table 6: Allometric models relating mangrove canopy height metrics (Hx; either Hmax or

269 Hba) to AGB. Simard et al (2019) used the power equations that did not use Hmax. 92

270 Table 7: Allometric equations relating SRTM height data to mangrove canopy height metrics.

271 93

272

	Ref	CCI Biomass Product Validation and Algorithm Selection Report		
	Issue	Page	Date	
	1.0	12	10.02.2019	

273 SYMBOLS AND ACRONYMS

ADP	Algorithm Development Plan
AGB	Above-Ground Biomass
ALOS	Advanced Land Observing Satellite
APBL	Australian Plant Biomass Library
ASAR	Advanced Synthetic Aperture Radar
BCEF	Biomass Conversion & Expansion Factor
BEF	Biomass Expansion Factor
CCI	Climate Change Initiative
CCI-Biomass	Climate Change Initiative – Biomass
CCI-LC	Climate Change Initiative – Land Cover
CEOS	Committee on Earth Observation Satellites
CHM	Canopy Height Model
DARD	Data Access Requirements Document
DEM	Digital Elevation Model
DRC	Democratic Republic of Congo
DSM	Digital Surface Model
DTM	Digital Terrain Model
DUE	Data User Element
E3UB	End to End ECV Uncertainty Budget
ECV	Essential Climate Variables
EO	Earth Observation
ESA	European Space Agency
FAO	Food and Agriculture Organization
FBD	Fine Beam Dual
FRA	Forest Resources Assessment
GCOM	Global Change Observation Mission
GEDI	Global Ecosystems Dynamics Investigation
GEZ	Global Ecological Zones
GFW	Global Forest Watch
GLAS	Geoscience Laser Altimeter System
GMW	Global Mangrove Watch
GSV	Growing Stock Volume
ICESAT	Ice, Cloud, and Land Elevation Satellite
IPCC	Intergovernmental Panel on Climate Change

	Ref	CCI Biomass Product Validation and Algorithm Selection Report		
	Issue	Page	Date	
	1.0	13	10.02.2019	

JAXA	Japanese Aerospace Exploration Agency
LAI	Leaf Area Index
LCCS	Land Cover Classification System
LiDAR	Light Detection and Ranging
MAAP	Multi-Mission Algorithm and Analysis Platform
MOLI	Multi-footprint Observation LiDAR and Imager
MODIS	Moderate Resolution Imaging Spectroradiometer
NASA	National Aeronautics and Space Administration
OLI	Operational Land Imager
PALSAR	Phased Array L-band Synthetic Aperture Radar
PSD	Product Specifications Document
PVASR	Product Validation and Algorithm Selection Report
RAT	Raster Attribute Table
RSGISLib	Remote Sensing and Geographical Information System Library
RMSE	Root Mean Square Error
SAR	Synthetic Aperture Radar
SLC	Scan Line Corrector
SMOS	Soil Moisture & Ocean Salinity
SRTM	Shuttle Radar Topography Mission
USD	User Specifications Document
USGS	United States Geological Survey
VCF	Vegetation Continuous Fields
VOD	Vegetation Optical Depth
VSV	Vegetation Stock Volume
WCM	Water Cloud Model
WWF	World Wildlife Fund

274 Table 1. Applicable documents

ID	TITLE	ISSUE	DATE
RD-1	User Requirements Document		
RD-2	Product Specification Document		
RD-3	Data Access Requirements Document		
RD-4	Algorithm Development Plan		
RD-5	Algorithm Theoretical Basis Document		
RD-6	End to End ECV Uncertainty Budget		

	Ref	CCI Biomass Product Validation and Algorithm Selection Report		
	Issue	Page	Date	
	1.0	14	10.02.2019	

RD-7	Product Validation Plan		
RD-8	Algorithm Theoretical Basis Document of GlobBiomass Project		

275 1 Introduction

276 1.1 Purpose and scope

277 The European Space Agency's (ESA) Climate Change Initiative (CCI) Biomass Project aims to
278 a) generate global estimates of above-ground biomass (AGB; Mg ha⁻¹) for the epochs
279 2017/18, 2018/19 and 2010 and b) quantify AGB change between these. This will be achieved
280 using spatially and temporally consistent Earth Observation (EO) datasets and state-of-the-
281 art models and aligning with other datasets produced through the CCI Program. The
282 requirement [RD-1] is for AGB to be provided wall-to-wall over the entire globe for all major
283 woody biomes, with a spatial resolution between 500 m and 1 km (based on satellite
284 observations of 100-200 m), a relative error of less than 20 % where AGB exceeds 50 Mg ha⁻¹,
285 and a fixed error of 10 Mg ha⁻¹ where the AGB is below that limit. This differs from the ESA
286 Data User Element (DUE) GlobBiomass project, where the emphasis was also on a global
287 product, but the requirement was for the relative error in AGB being ≤ 30% and the spatial
288 resolution ≤ 500 m. Hence, in CCI Biomass, greater accuracy is required in biomes supporting
289 lower levels of AGB (e.g., the dry tropics/subtropics and boreal zones).

290
291 For 2017/18, use is being made of available Sentinel-1 C-band Synthetic Aperture Radar (SAR)
292 and Advanced Land Observing satellite (ALOS)-2 Phased Array Type L-band Synthetic
293 Aperture Radar (PALSAR)-2 data and a slightly modified version of the GlobBiomass algorithm
294 [RD-8]. The ICESAT Geoscience Laser Altimeter System (GLAS), Moderate Resolution Imaging
295 Spectroradiometer (MODIS) Vegetation Continuous Fields (VCF; or MOD44B; DiMiceli et al.,
296 2015) are also used as auxiliary datasets to parameterise the models. For 2018/19, these
297 same data are being considered alongside other satellite sensors, including the National
298 Aeronautics and Space Administration's (NASA) Global Ecosystem Dynamics Investigation
299 (GEDI) and ICESAT-2. For 2010, and as with the GlobBiomass product, ENVISAT Advanced SAR
300 (ASAR) and ALOS PALSAR data for 2010 and Landsat sensor data and derived products
301 (namely canopy cover products from Hansen et al. (2013) and the United States Geological
302 Survey; USGS) will be used. Consideration will also be given, if proven superior to current
303 the method, to the use of Vegetation Optical Depth (VOD) from passive microwave sensors,

	Ref	CCI Biomass Product Validation and Algorithm Selection Report		
	Issue	Page	Date	
	1.0	15	10.02.2019	

304 and soil moisture data from either the Soil Moisture & Ocean Salinity (SMOS) sensor, the
305 Global Change Observation Mission (GCOM) or CCI Soil Moisture products. The focus for the
306 CCI project team is the development of retrieval algorithms that best integrate data from
307 these sensors at a global level with appropriate reference to *in situ* data (including those
308 scaled using airborne datasets).

309
310 The GlobBiomass algorithm developed through the ESA DUE GlobBiomass [RD-8; Rodríguez-
311 Veiga et al., 2019] project was based on the use of the Water Cloud Model (WCM), which
312 relates the radar backscatter at C- and L- band to the forest Growing Stock Volume (GSV).
313 AGB was then estimated through reference to wood density (g cm^{-3}) and Biomass Expansion
314 Factors (BEF), with these considering the relative amounts of biomass contained within the
315 non-stem components [RD-5]. The algorithm development aimed at optimization of the
316 automatic model calibration approach to derive model parameters, while minimizing the
317 need for *in situ* data when calibrating the relation between EO observations and AGB.
318 However, a limitation of the BIOMASAR algorithms built in the GlobBiomass algorithm is that
319 the parameterisations of the WCM have been approximations [RD-5]. Furthermore, the
320 WCM is relatively simple and, in the current form, is less able to capture the spatial variability
321 of GSV within its modelling framework and calibration procedure.

322
323 The Product Validation and Algorithm Selection Report (PVASR) investigates potential ways
324 to improve the estimation of AGB, building on the algorithms described in the Algorithm
325 Theoretical Basis Document (ATBD) [RD-5], which outlines the data and algorithms used for
326 generating the global AGB and AGB change products specified above. The ATBD is based on
327 the indications of the Users Requirements Document (URD) [RD-1], the Product
328 Specifications Document (PSD) [RD-2] and the Data Access Requirements Document (DARD)
329 [RD-3].

330
331 The scope of the PVASR is to:

- 332
- 333 a) Assess the current BIOMASAR-C and BIOMASAR-L algorithms in terms of their
334 performance globally and for specific biomes (e.g., wet tropics/subtropics) and forest
335 types (e.g., mangroves) including reviewing the 2010 GlobBiomass AGB product and
336 highlighting the reasons for good or weak performance (whether generic or
337 biome/forest type specific).
 - 338 b) Review the assumptions used in the WCM and the procedure for estimating the
339 model parameters.
-

	Ref	CCI Biomass Product Validation and Algorithm Selection Report		
	Issue	Page	Date	
	1.0	16	10.02.2019	

- 340 c) Identify the impact of EO data issues and environmental conditions on the retrieval
341 of AGB.
342 d) Suggest improvements to the WCM and calibration procedure and indicate other EO
343 data and environmental information (including variables generated through other
344 ESA CCI projects) that might support AGB retrieval.
345

346 The Project Team made use of their extensive knowledge of forest structure and functioning
347 across different biomes and forest types to assess performance of the GlobBiomass
348 algorithm but also provided an independent review of the GlobBiomass map by exploiting
349 reference datasets (mainly *in situ* and airborne LiDAR but also other AGB maps) to provide a
350 more quantitative assessment of errors.
351

352 Following this introduction, Section 2 provides the assessment of the GlobBiomass Product
353 for five major forest biomes (the wet tropics/subtropics, dry tropics/subtropics, temperate,
354 boreal, and mangroves). Section 3 outlines some of the general issues associated with AGB
355 retrieval across all biomes. Improvements to the Global AGB Retrieval Algorithm are
356 indicated in Section 4 and complementary approaches are outlined in Section 5. Section 6
357 provides recommendations and conclusions.

358 2 Biomes evaluations

359 2.1 Wet tropics/subtropics and mangroves

360 For the wet tropics and sub-tropics, the 2010 GlobBiomass map was evaluated against: a)
361 forest inventory (plot) data for Brazil, Colombia and Thailand and b) AGB biomass maps for
362 Gabon, French Guiana and the Democratic Republic of Congo (DRC), including those
363 generated with reference to airborne LiDAR and *in situ* data.

364 2.1.1 Forest Inventory (plot) data.

365 Forest Inventory (plot) data were a) limited in number and geolocation, and of relatively small
366 size which can be a major source of analysis error (Villard and Le Toan, 2014), b) generated
367 by applying a non-standardized range of allometric equations and c) not acquired at or close
368 to the time of the SAR data. Many plots were also located in forests that were not

	Ref	CCI Biomass Product Validation and Algorithm Selection Report		
	Issue	Page	Date	
	1.0	17	10.02.2019	

369 representative of the forest ecosystem (Réjou Méchain et al., 2016). Nevertheless,
 370 comparison of the AGB estimated by the BIOMASAR algorithm and in the field provided some
 371 indication of retrieval performance.

372

373 For Tapajos, Brazil, a poor correspondence between AGB estimated from 38 0.25 ha plots
 374 and the BIOMASAR algorithm was observed, with an overestimation occurring where the *in*
 375 *situ* AGB was < 250 Mg ha⁻¹ (Figure 1a). A similar overestimation was observed when the
 376 GlobBiomass product was compared to the AGB estimated from 36 plots (0.25 ha) located in
 377 the Pacifico region (Colombia) (Figure 1b). In this case, discrepancies can be attributed to the
 378 7-8 year gap between the image acquisitions (2010) and the collection of inventory data
 379 (2017) from degraded forests.

380

381 Comparison with the AGB estimated from thousands of 0.1 ha plots measured through the
 382 Thailand National Forestry Inventory in 2004-2010 and 2010-2015 again indicated significant
 383 overestimation and underestimation in areas of low (< 100 Mg ha⁻¹) and high (> 150 Mg ha⁻¹)
 384 AGB respectively. Whilst small in size (0.1 ha), the large number of inventory plots
 385 highlighted the overestimation of AGB for low AGB areas in the GlobBiomass product and
 386 underestimation of AGB for high AGB areas.

387

388

389

390

391

392

393

394

395

396

397

398

399

400

401

402

403

404

405

	Ref	CCI Biomass Product Validation and Algorithm Selection Report		
	Issue	Page	Date	
	1.0	18	10.02.2019	

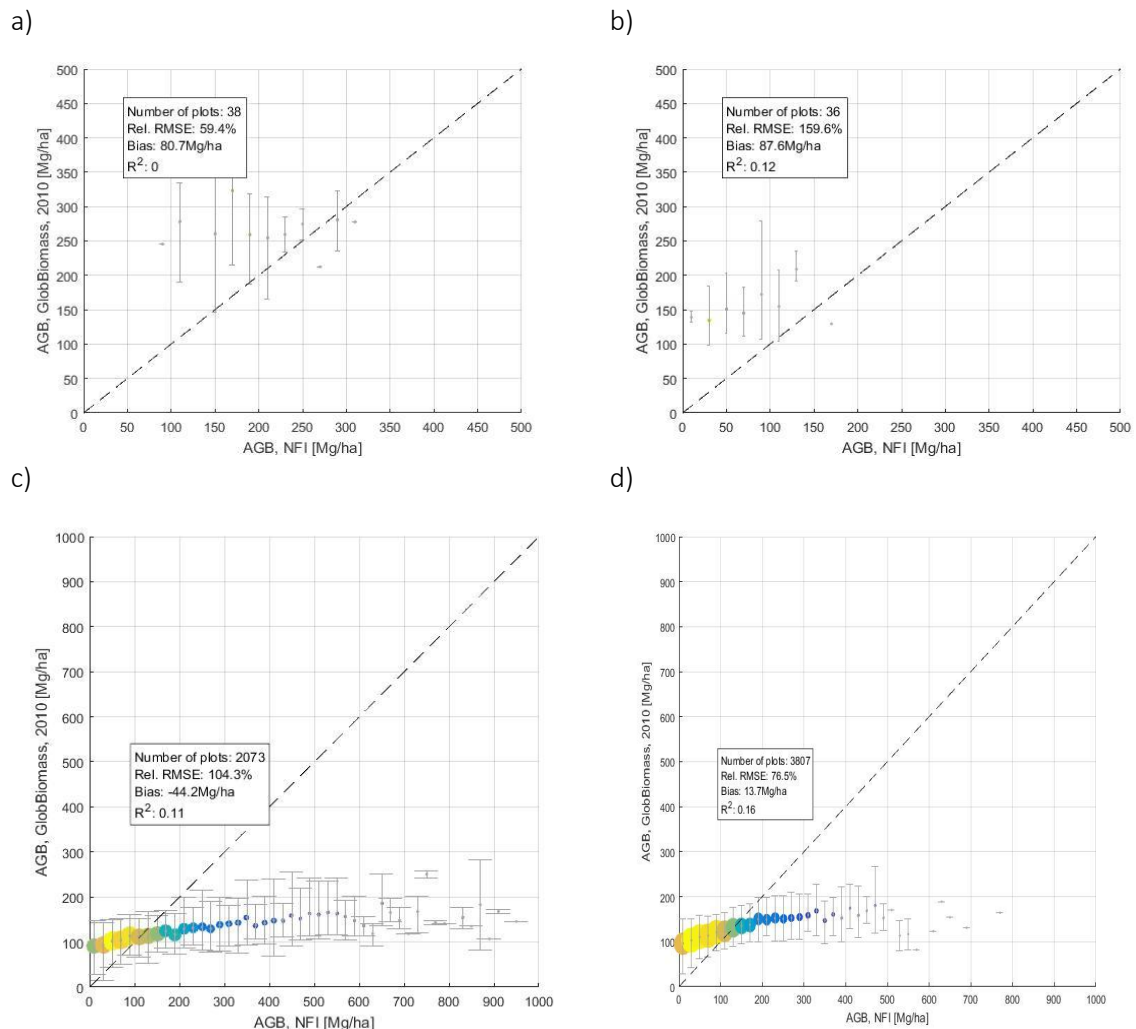


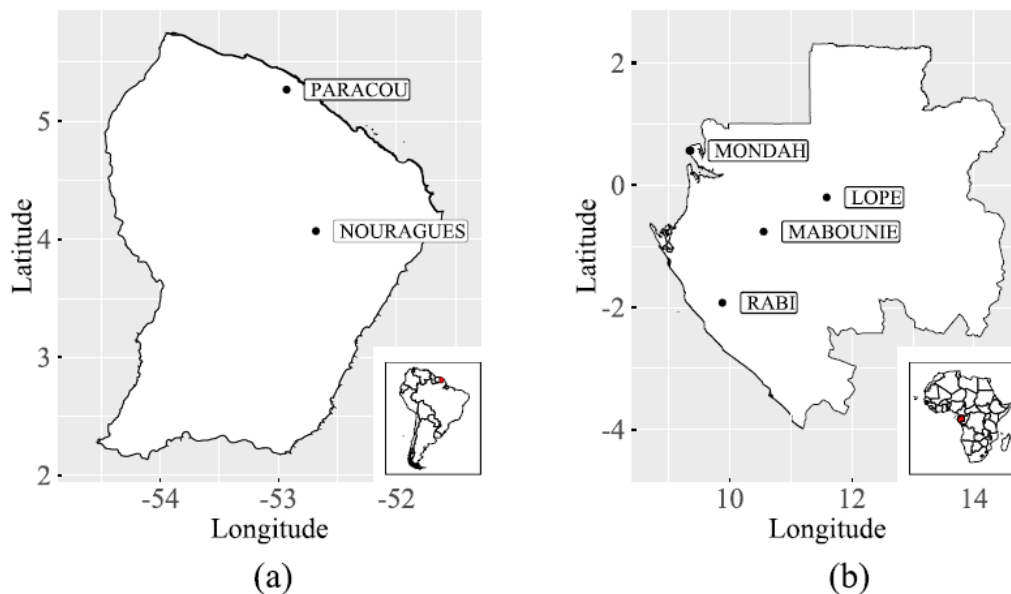
Figure 1: Comparison of the AGB estimated using the BIOMASAR algorithm from a) 38 plots located near Tapajos, Brazil, b) 36 plots located in Colombia and Thailand National forest inventory plots (of 0.1 ha) from c) 2004-2010 and d) 2010-2015.

406 2.1.2 AGB estimated from airborne LiDAR

407 AGB was estimated from airborne LiDAR maps in Gabon (2015-16; AfriSAR campaign – 4
408 maps) (Labrière et al., 2018) and the DRC (numerous acquisitions; Xu et al., 2017) (Figure 2).
409 These maps of AGB were representative of larger areas than could be achieved using forest
410 inventory data alone but were derived by referencing these. For each site, the LiDAR-derived

	Ref	CCI Biomass Product Validation and Algorithm Selection Report		
	Issue	Page	Date	
	1.0	19	10.02.2019	

411 maps of AGB were resized to the 100 m resolution of the GlobBiomass product and a Fast
412 Fourier Transform was used to correct for image shifts.



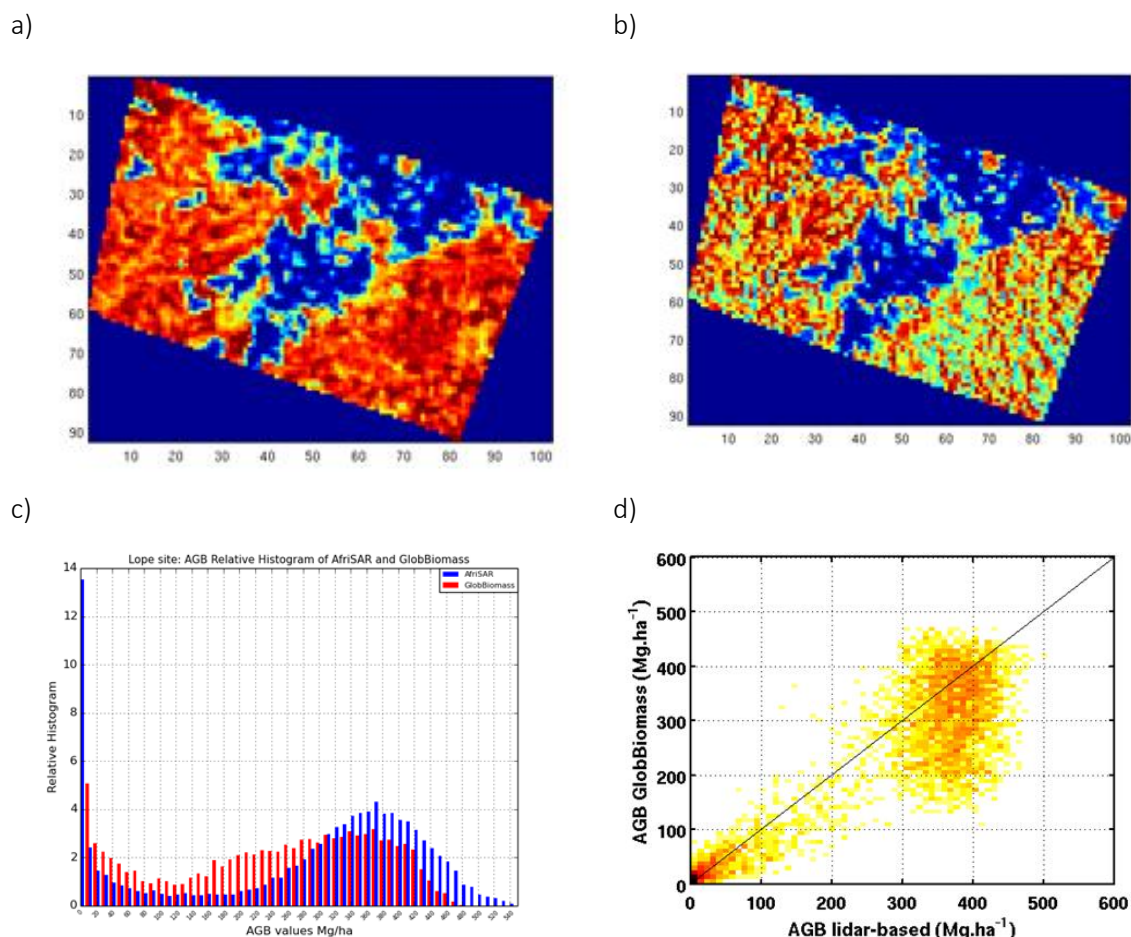
413
414 Figure 2: The location of study sites in (a) French Guiana and (b) Gabon.

415 Gabon -Lopé

416 Lopé is located near the geographical centre of Gabon (0.20° S, 11.59° E). The hilly landscape
417 (altitude ranging from 200 to 600 m a.s.l.) is dominated by a forest-savannah mosaic (e.g.,
418 Aucoumea-dominated and/or Marantaceae forests) where the AGB can exceed 600 Mg ha⁻¹,
419 whilst savannah (with lower AGB) occurs over flat terrain. Comparison between the AGB
420 estimated from LiDAR and the GlobBiomass algorithms indicated an abrupt transition
421 between savannah and forests. Good agreement was observed between the ranges of AGB
422 of savannah (despite small-scale variability occurring in the GlobBiomass product, which was
423 not observed in the LiDAR-derived map). However, for higher AGB, the LiDAR-derived AGB
424 was greater than that estimated using the GlobBiomass product (Figure 3) but there was a
425 closer correspondence for forests with a LiDAR-derived AGB estimate in the range 100-300
426 Mg ha⁻¹.

427
428
429
430
431

	Ref	CCI Biomass Product Validation and Algorithm Selection Report		
	Issue	Page	Date	
	1.0	20	10.02.2019	



432 Figure 3: AGB estimated from a) LiDAR and b) the GlobBiomass algorithm for Lope, Gabon (from 0 (blue) to 450
433 Mg ha^{-1} (red)), c) the frequency distribution and d) comparison between the two AGB products.

434 Gabon -Mabounie

435 Mabounie is located ca. 180 km Southeast of Libreville (0.76°S , 10.56°E), where the altitude
436 ranges from 25 to 230 m a.s.l. The landscape is mostly forested (of which swamp and
437 temporarily flooded forests constitute a large proportion) but shows evidence of degradation
438 locally. Comparison between the AGB derived from LiDAR and the GlobBiomass algorithm
439 indicated weak agreement (Figure 4), with less variation observed in the latter. Higher values
440 of AGB were underestimated by the GlobBiomass algorithm and exaggerated estimates were
441 noted for swamp and forests close to water (attributed to greater double-bounce
442 interactions). Differences in the timing between the observations might have led to
443 discrepancies as a result of degradation and/or regrowth. As with Lopé, an underestimation
444 of high AGB (Figure 4 a and b), large differences of the AGB in all classes and no correlation

	Ref	CCI Biomass Product Validation and Algorithm Selection Report		
	Issue	Page	Date	
	1.0	21	10.02.2019	

445 for all the forest classes (including the low biomass degraded forest) were observed (in Lopé,
446 savannahs were associated with the low AGB class).
447

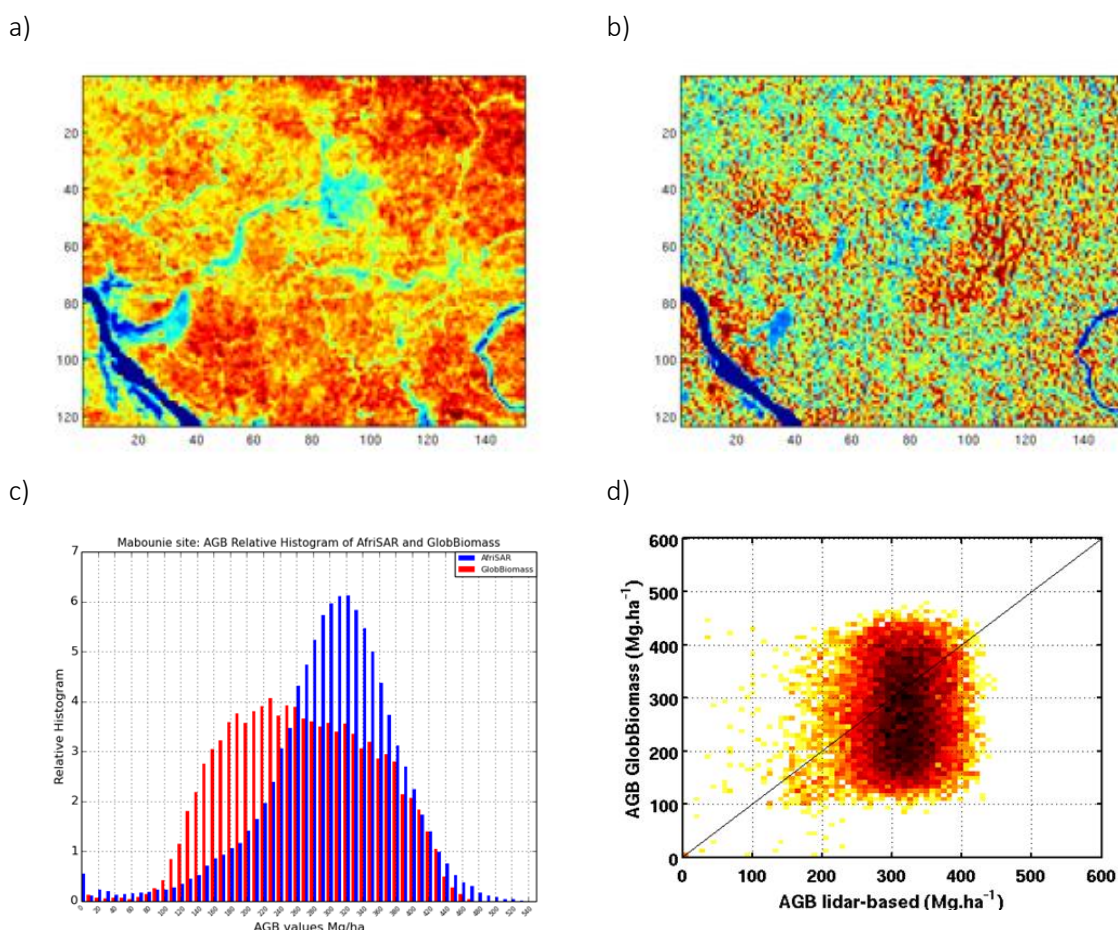


Figure 4: AGB derived over Mabounie, Gabon from a) LiDAR and b) the BIOMASAR product (from 0 Mg ha⁻¹ (blue) to 450 Mg ha⁻¹; red), c) the frequency distribution and d) comparison between the two AGB products.

448 The LiDAR-derived AGB and the GlobBiomass product have little correspondence between
449 the two estimates. The GlobBiomass AGB presents a broad distribution centred around 250
450 Mg ha⁻¹ whereas the LiDAR map AGB distribution is narrower and centred around 320 Mg
451 ha⁻¹, partly because of the predominance of high AGB forests.

452 Gabon -Mondah

453 Mondah is located ca. 25 km Northwest of Libreville toward Cap Esterias (0.57°N, 9.35°E) and
454 the altitude seldom exceeds 50 m a.s.l. Different vegetation types occur in this coastal
455 landscape, including Aucoumea-dominated and mixed forests, and whilst significant
456 disturbance occurs, some patches are protected. The comparison of the AGB estimated from

	Ref	CCI Biomass Product Validation and Algorithm Selection Report		
	Issue	Page	Date	
	1.0	22	10.02.2019	

457 LiDAR and using the GlobBiomass algorithm indicated discrepancies in the spatial patterning
458 (Figure 5). Higher AGB in the GlobBiomass map was observed in the areas close to the river,
459 which was attributed to an enhanced SAR response from inundated vegetation or moist soil.
460 The higher AGB in the north west of the LiDAR image was not adequately captured in the
461 GlobBiomass map. However, the time difference between the LiDAR data (2013) and ALOS
462 data (2010) at this site where significant degradations occurred prevents from further
463 interpretation of the quantitative comparison (disagreement can be seen in the histograms
464 of AGB from the two datasets (Figure 5c). A low correlation (r^2 of 0.31) and high Root Mean
465 Square Error (RMSE) of 130.9 Mg ha^{-1} were observed between the two AGB estimates). There
466 was also significant variability from topography.
467

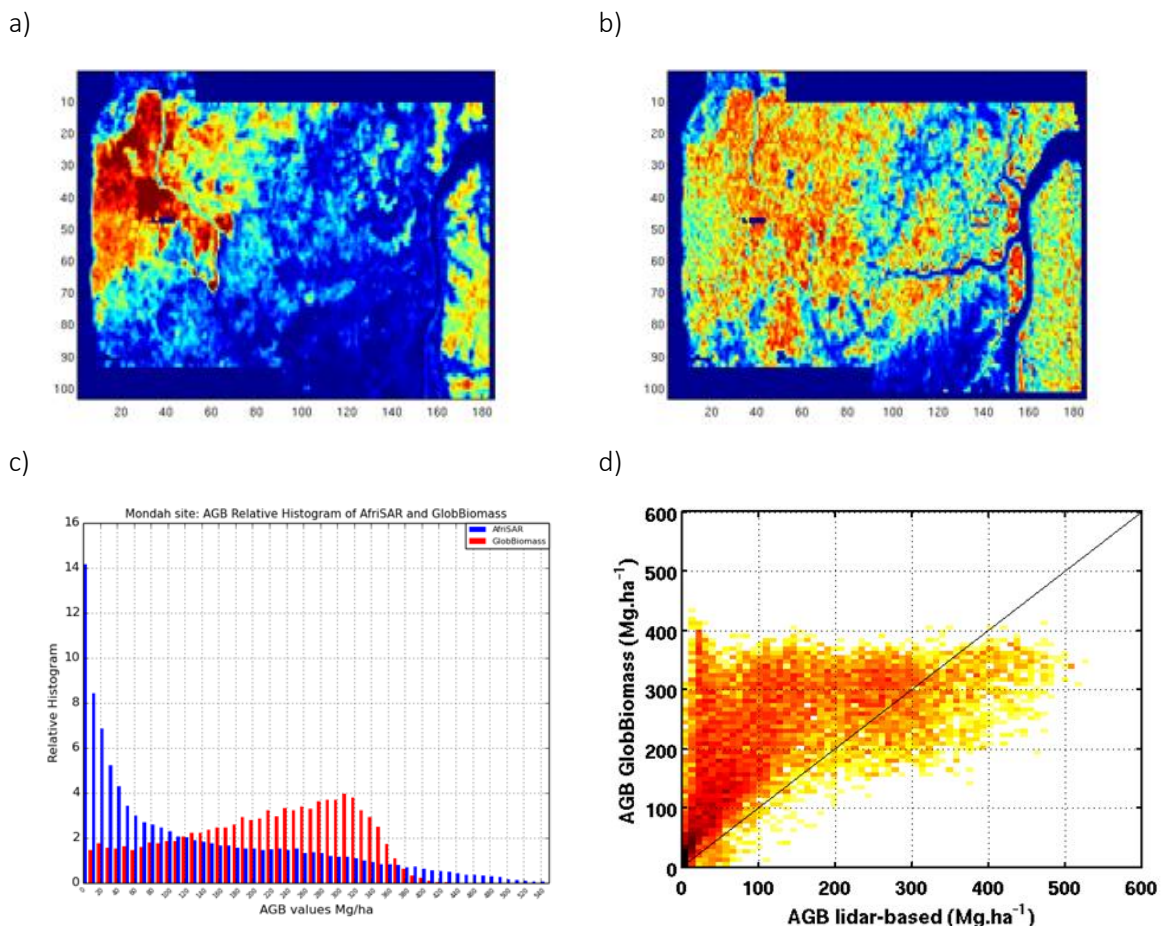


Figure 5: AGB derived over Mondah, Gabon from a) LiDAR and b) the BIOMASAR product, c) the frequency distribution and d) comparison between the two AGB products. Blue areas in a) correspond to the non-forest areas. Colour code ranges from 0 (blue) to 450 (red) Mg ha⁻¹.

	Ref	CCI Biomass Product Validation and Algorithm Selection Report		
	Issue	Page	Date	
	1.0	23	10.02.2019	

468 **Gabon - Rabi**

469 Rabi is located ca 260 km south of Libreville (1.92°S, 9.88°E) where the altitude ranges from
 470 30 to 80 m a.s.l. The vegetation is comprised largely of lowland old growth rainforest.
 471 Underestimation of AGB was noted in the GlobBiomass map. The Gaussian distribution of
 472 AGB centred on 280 Mg ha⁻¹ found from LiDAR-based AGB data was typical of lowland
 473 tropical rain forest whereas the GlobBiomass AGB distribution had a mean of 220 Mg ha⁻¹
 474 and was skewed towards lower values (100-200 Mg ha⁻¹; Figure 6).
 475

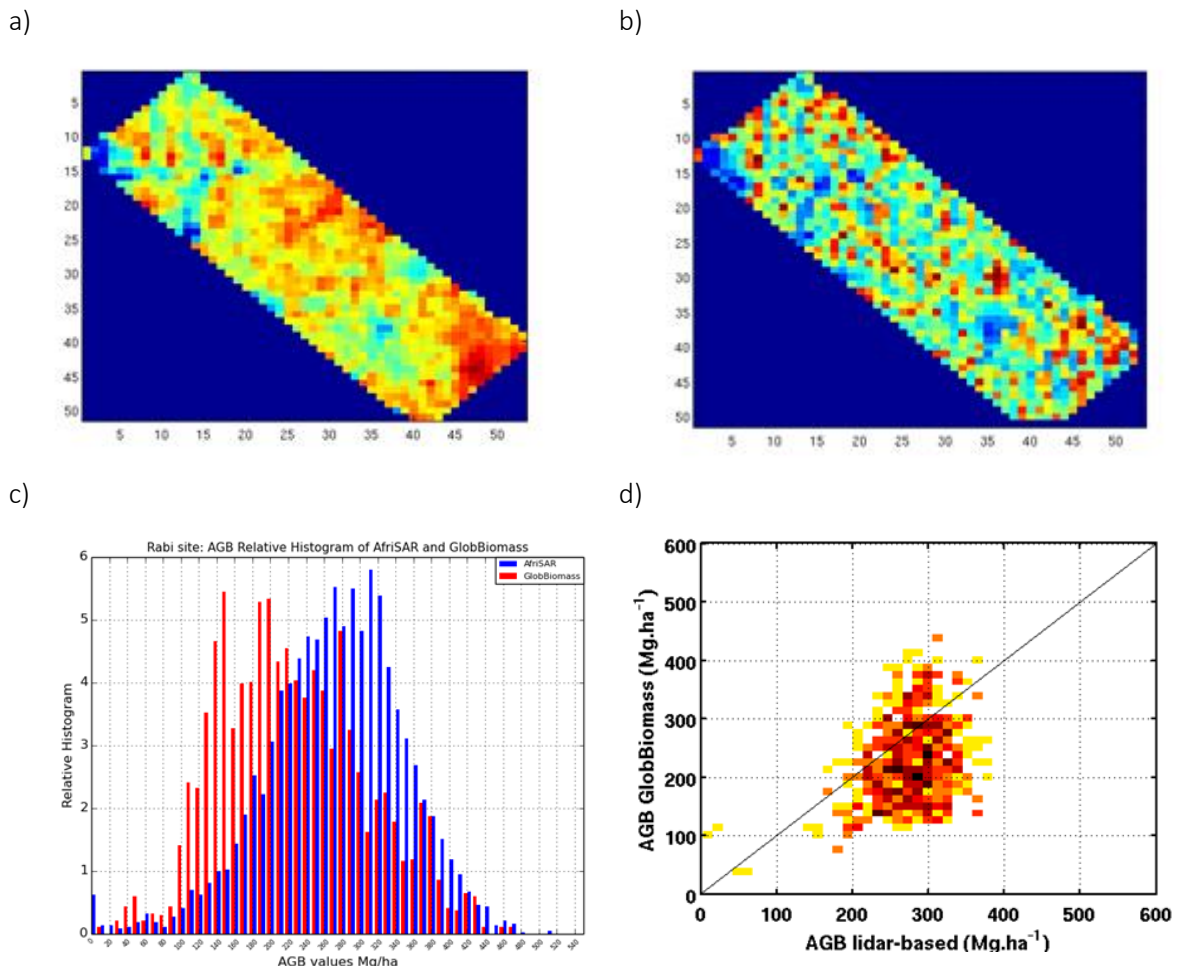


Figure 6: AGB derived over Rabi, Gabon from a) LiDAR and b) the BIOMASAR product, c) the frequency distribution and d) comparison between the two AGB products. Blue areas in a) correspond to the non-forest areas. Colour code ranges from 0 (blue) to 450 (red) Mg ha⁻¹.

	Ref	CCI Biomass Product Validation and Algorithm Selection Report		
	Issue	Page	Date	
	1.0	24	10.02.2019	

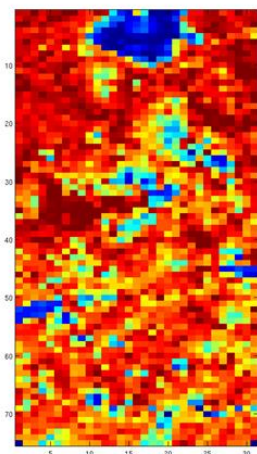
476 **French Guiana - Nouragues**

477 Nouragues is located ~ 100 km south of Cayenne, French Guiana (4.06°N, 52.68°W). The
478 terrain is gently hilly, with an altitude ranging between 26 and 280 m a.s.l. except in the
479 northern part of the area where a granitic outcrop (inselberg) reaches 430 m a.s.l. Forest
480 formations include high-canopy old-growth forest and lower-canopy forest formations,
481 including periodically flooded forest dominated with palm trees, liana forest, and bamboo
482 thickets. There are typically about 145 tree species (with diameter at breast height c.10 cm)
483 per ha. The AGB was underestimated at higher levels by the GlobBiomass algorithm, spatial
484 patterns were not similar to those from LiDAR, and topography had a major influence on the
485 mapped distribution (AGB being particularly overestimated in the unvegetated outcrop in
486 the northern part of the scene). Very low correlation (r^2 of 0.1) between the two maps was
487 observed for all AGB classes (Figure 7).

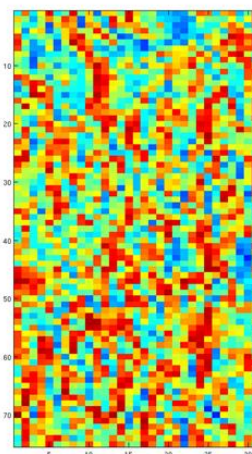
488
489
490
491
492
493
494
495
496
497
498
499
500
501
502
503
504
505
506
507
508
509
510
511
512

	Ref	CCI Biomass Product Validation and Algorithm Selection Report		
	Issue	Page	Date	
	1.0	25	10.02.2019	

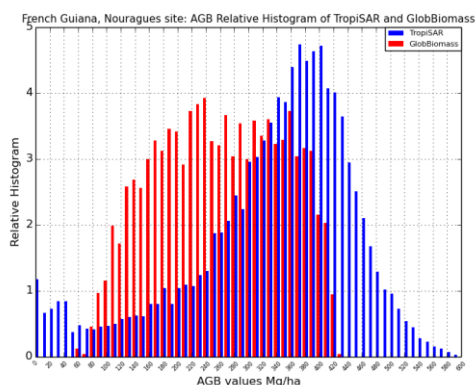
a)



b)



c)



d)

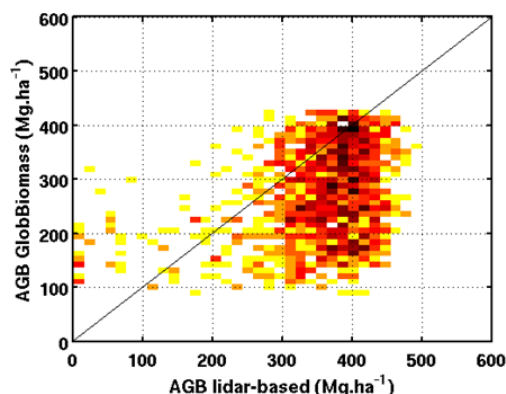


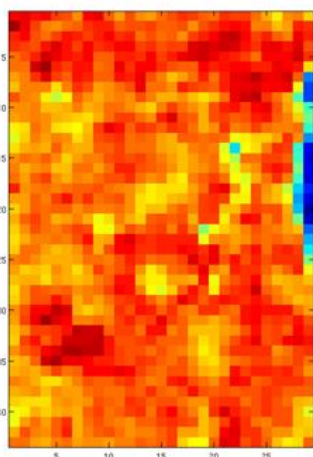
Figure 7: AGB derived from Nouragues, French Guyana using a) LiDAR and b) the BIOMASAR product, c) the frequency distribution and d) comparison between the two AGB products. Blue areas in a) correspond to the non-forest areas and values range from 0 (blue) to 450 (red) Mg ha^{-1} .

513 French Guiana - Paracou

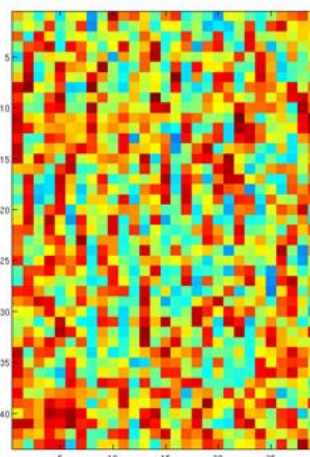
514 Paracou (is located ca. 75 km West of Cayenne (5.27°N, 52.93°W), where the altitude ranges
 515 between 5 and 45 m a.s.l. over an undulating terrain. Mean tree species richness (ca. 140
 516 species per ha) is comparable to that in Nouragues. The research station was established in
 517 1984 in an area of disturbance-free moist evergreen rain forest to initiate an experimental
 518 disturbance program. The AGB ranges from 250 to 450 Mg ha^{-1} , the lower range of which
 519 corresponds to the plots partially degraded in 1984. The pattern of partially degraded forest,
 520 visible on the LiDAR data, are difficult to recognize in the GlobBiomass product and there was
 521 an over-estimation of AGB in the range 100-300 Mg ha^{-1} (Figure 8).
 522

	Ref	CCI Biomass Product Validation and Algorithm Selection Report		
	Issue	Page	Date	
	1.0	26	10.02.2019	

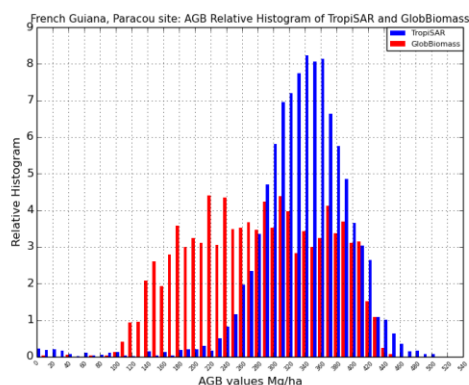
a)



b)



c)



d)

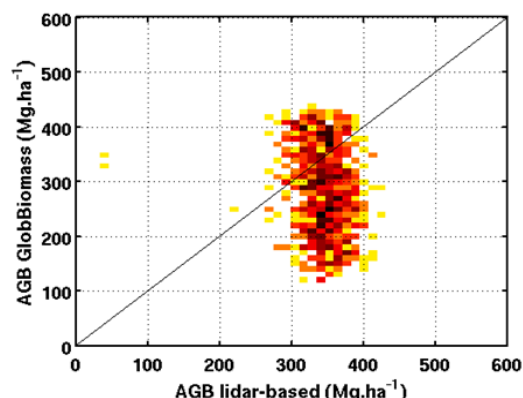


Figure 8: AGB derived over Paracou, French Guyana from a) LiDAR and b) the BIOMASAR product. Blue areas in a) correspond to the non-forest areas and values range from 0 (blue) to 450 (red) Mg ha^{-1} .

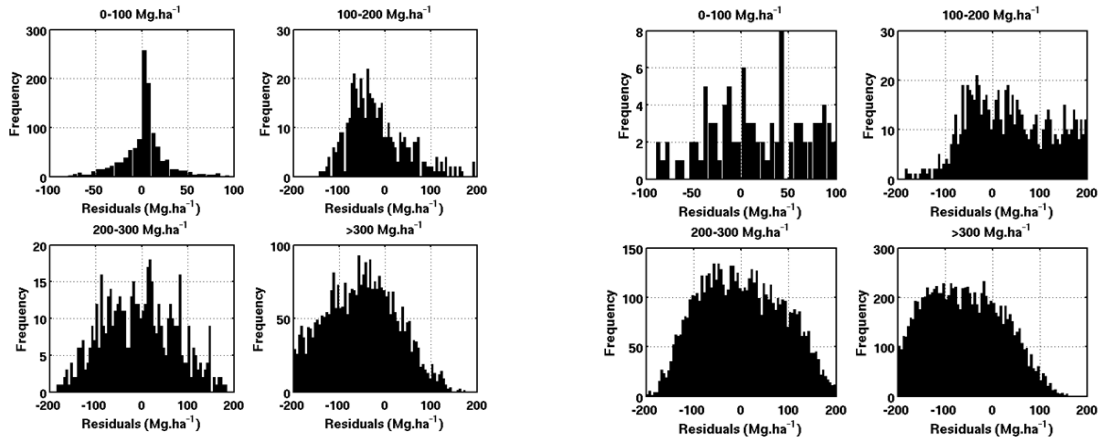
523

524 A comparison of the frequency distributions for the GlobBiomass product and LiDAR derived
525 products was undertaken for different AGB ranges: 0-100, 100-200, 200-300 and $> 300 \text{ Mg ha}^{-1}$
526 ha^{-1} for Lopé, Mabounie, Mondah and Rabi in Gabon, and Nouragues and Paracou in French
527 Guiana (Figure 9; Table 2). For all sites, differences were greatest where the AGB ranged from
528 200-300 or was $> 300 \text{ Mg ha}^{-1}$. Within the 0-100 Mg ha^{-1} , differences were noted with the
529 exception of the Lopé savannah. Many non-forest sites in Mondah were associated with high
530 values of AGB. At the landscape scale (the LiDAR maps covering from 1000 ha to 18000 ha)
531 a broad correspondence is observed between mean AGB values from GlobBiomass and from
532 LiDAR, with an underestimation of AGB fro GlobBiomass in all sites except Mondah (Figure
533 10).

a) Lopé

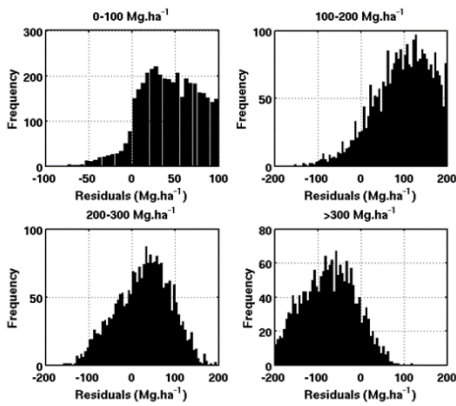
b) Mabounie

	Ref	CCI Biomass Product Validation and Algorithm Selection Report		
	Issue	Page	Date	
	1.0	27	10.02.2019	



c) Mondah

d) Rabi



e) Nouragues

f) Paracou

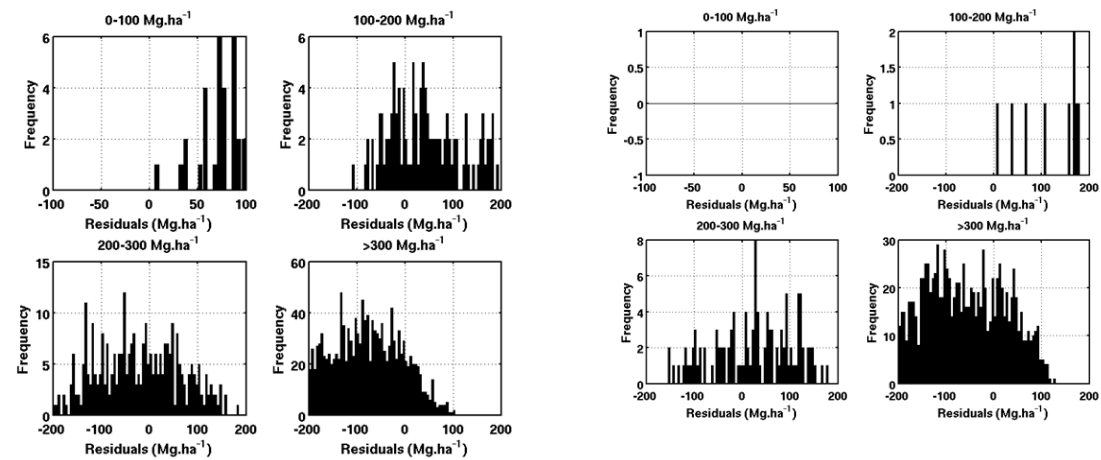


Figure 9: Quantitative assessment of the residuals stratified by reference AGB range. Comparison between LiDAR-based and GlobBiomass AGB maps over a) Lope, b) Mabounie, c) Mondah and d) Rabi in Gabon and e) Nouragues and f) Paracou in French Guiana (note the top left hand plot had AGB < 100t/ha).

	Ref	CCI Biomass Product Validation and Algorithm Selection Report		
	Issue	Page	Date	
	1.0	28	10.02.2019	

534 Table 2: Statistics in the comparison of AGB estimated from LiDAR (TropiSAR and AfriSAR campaigns) and
535 using the BIOMASAR algorithms. AGB is stratified into 4 classes: < 100 Mg ha⁻¹, 100-200 Mg ha⁻¹, 200-300 Mg
536 ha⁻¹, > 300 Mg ha⁻¹. For each class, N= number of pixels (100m); E(B)= mean AGB from the LiDAR derived map
537 in Mg ha⁻¹, E(^B)= mean AGB from GlobBiomass in Mg ha⁻¹, E (Resi)= difference in Mg ha⁻¹. ¹mean LiDAR-
538 derived AGB (Mg ha⁻¹); ²mean GlobBiomass AGB (Mg ha⁻¹); ³AGB difference (Mg ha⁻¹). N represents the
539 number of 100 m pixels.
540

Site	Range	N	E(B) ¹ Mg ha ⁻¹	E(^B) ² Mg ha ⁻¹	E(Resi) ³ Mg ha ⁻¹	RMSE Mg ha ⁻¹	R ²
Lope	all	5659	277.6	237.8	-39.8	90.7	0.70
	<100	1160	32.3	36.4	4.1	29.5	0.41
	100-200	452	146.7	130.2	-16.5	44.9	0.14
	200-300	541	258.6	252.7	-5.9	79	0.15
	>300	3506	378.6	316.1	-62.5	106.8	0.01
Mabounie	all	18320	305.9	269.8	-36.1	105.2	0.02
	<100	198	59.3	191.5	132.1	188.4	0.07
	100-200	842	165.6	225.5	59.9	109.2	0.01
	200-300	6255	267.7	269	1.4	88.1	0
	>300	11025	342.8	275	-67.8	110.6	0
Mondah	all	15493	140.1	216.2	76.1	130.9	0.31
	<100	7714	43.1	160.7	117.6	150.1	0.13
	100-200	3334	142.7	253	110.3	80.5	0.02
	200-300	2425	250.5	276.7	26.2	67.5	0
	>300	2020	373.6	294.6	-79	103	0.09
Rabi	all	1047	273.5	232.5	-41	93.3	0.12
	<100	17	49.8	71.9	22.1	50.5	0.01
	100-200	79	171	173.6	2.6	67.5	0
	200-300	612	260	233.1	-26.9	80.9	0.04
	>300	339	332.9	253.3	-79.7	117	0
Nouragues	all	2220	336.7	263.9	-72.8	133.7	0.1
	<100	119	42.4	192.1	149.7	165.3	0.06
	100-200	117	155.4	207.6	52.2	75.3	0.02
	200-300	303	261	239.7	-21.3	75.3	0.03
	>300	1681	383.8	277.3	-106.5	139.9	0.02
Paracou	all	1284	340.2	284.8	-55.4	114.5	0.02
	<100	11	50.8	309.5	258.6	264.7	0.42
	100-200	14	158.9	320.4	161.5	136.8	0
	200-300	116	280.6	307.3	26.6	88.1	0
	>300	1143	351.3	281.9	-69.4	113.5	0.02

541

542

	Ref	CCI Biomass Product Validation and Algorithm Selection Report	
	Issue	Page	Date
	1.0	29	10.02.2019



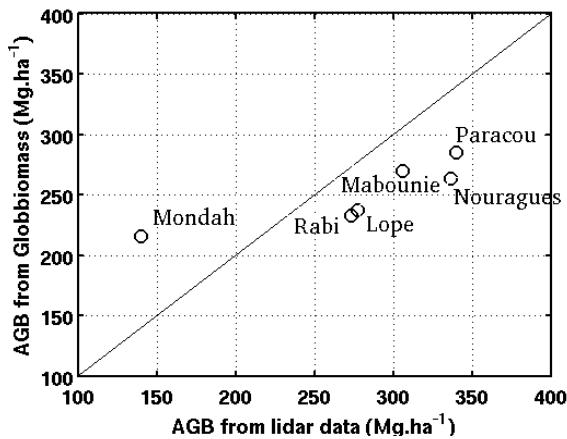


Figure 10: Comparison of the AGB estimated from LiDAR and using the GlobBiomass algorithm (GlobBiomass map) for 4 sites in Gabon and 2 sites in French Guiana (Paracou and Nouragues).

543

544 2.1.3 Comparison with existing AGB Maps

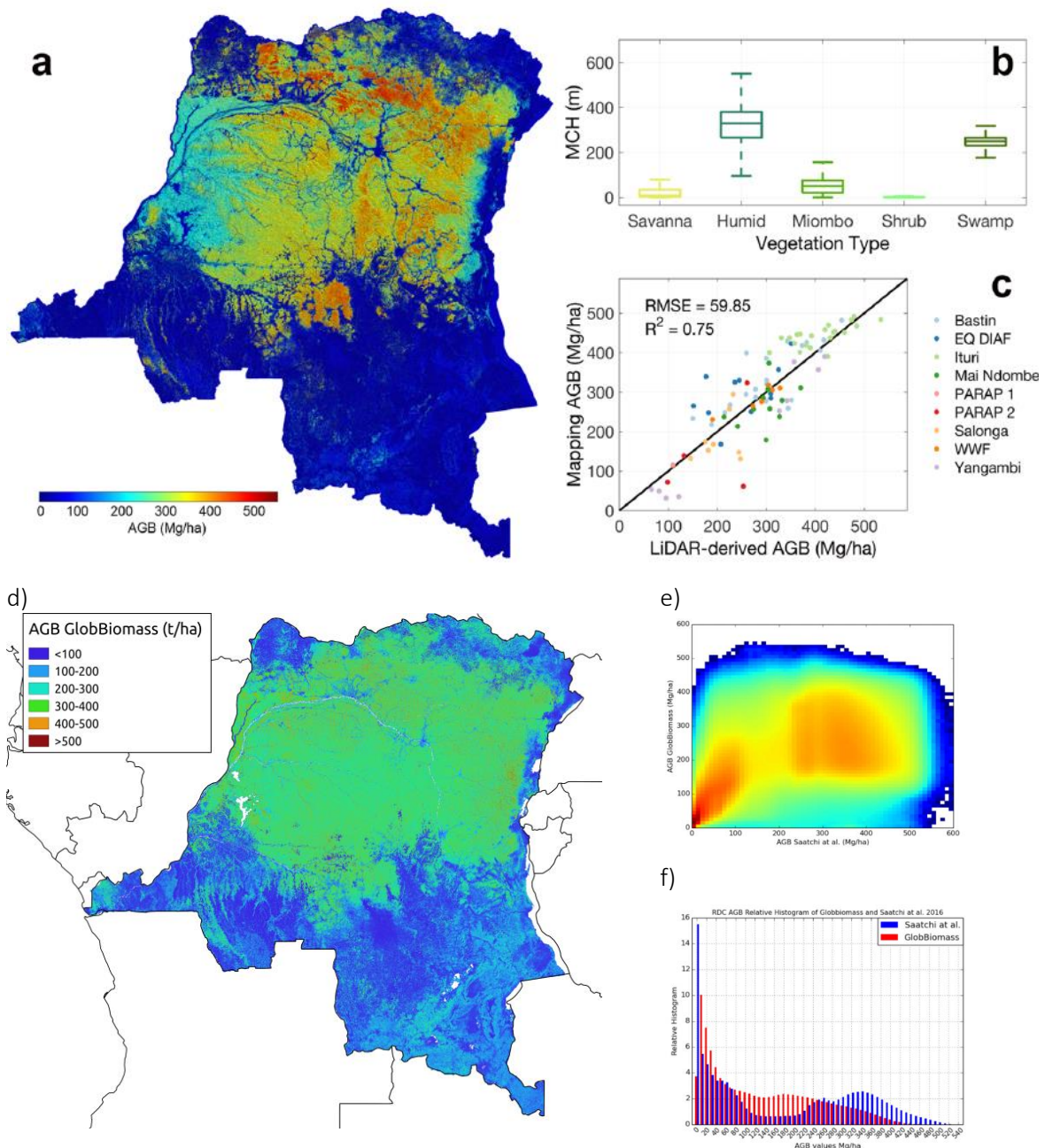
545 Comparison with existing AGB Maps (DRC)

546 The larger scale AGB map from Xu et al. (2017) over the DRC was compared against the
547 GlobBiomass AGB product. The GlobBiomass map showed no obvious spatial patterns of
548 carbon stored in forests of the DRC as those obtained using airborne LiDAR inventory
549 acquired over more than 432,000 ha of forests (using a probability sampling approach). 92
550 1-ha ground plots were available to support the scaling of AGB, with these distributed across
551 key forest types in DRC. Xu et al. (2017) scaled from LiDAR estimates of AGB using a
552 combination of Landsat, ALOS PALSAR and Shuttle Radar Topography Mission (SRTM) data.
553 Since both the Xu et al. (2017) and the GlobBiomass maps use ALOS PALSAR and SRTM data
554 in their production, and both were at 100 m resolution, the comparison focused on the large-
555 scale spatial pattern with a view of highlighting the differences between products, with and
556 without extensive ground and LiDAR data.

557

558 In the west of the DRC, swamp forests cover ~9.5 million hectares distributed along the rivers
559 and lakes (light blue in Figure 11), and support an AGB in the range of 230-300 Mg ha⁻¹. The
560 humid tropical forests of DRC (yellow/orange in Figure 11) support a much higher AGB
561 density (~300 Mg ha⁻¹), higher wood density (~0.66gcm³), and a relatively lower stem density
562 (~400 trees ha⁻¹) compared to tropical forests in Amazonia and south east Asia. The taller
563 forest (typically exceeding 60 m; red areas in Figure 11) typically have a mean wood density
564 > 0.7gcm⁻³ and AGB values > 400 Mg ha⁻¹. In the southern provinces of DRC, the land cover
565 is dominated by a mosaic of tree grass savanna and riparian forests, where the AGB is
566 significantly lower (20-50 Mg ha⁻¹).

	Ref	CCI Biomass Product Validation and Algorithm Selection Report		
	Issue	Page	Date	
	1.0	30	10.02.2019	



567 Figure 11: AGB product for the DRC (Xi et al., 2017) highlighting tree-grass savannahs (darker blues; ~20-50 Mg
568 ha⁻¹), swamp forests (light blue; ~230-300 Mg ha⁻¹) and humid tropical forests (yellow-orange; AGB of ~300-400
569 Mg ha⁻¹ and > 400 Mg ha⁻¹ (red); b) mean estimates of AGB for savannahs, swamp forest and humid forests as
570 well as Miombo and Shrub forest; and c) comparison between LiDAR-derived AGB and the AGB mapped using
571 the algorithm of Xu et al. (2017). d) shows the GlobBiomass map e) the map of difference in AGB and f) the
572 pixel-by-pixel scatterplot and histograms comparison of the GlobBiomass and Xu et al. (2017) AGB maps.

	Ref	CCI Biomass Product Validation and Algorithm Selection Report		
	Issue	Page	Date	
	1.0	31	10.02.2019	

573

574 The comparisons with the GlobBiomass product highlighted overestimation of AGB in the
575 low AGB range $<100 \text{ Mg ha}^{-1}$, and underestimation at the higher AGB levels (primarily
576 rainforest). The AGB range was reduced in the GlobBiomass product (250-265 Mg ha^{-1})
577 compared to Xu et al. (2017; 283-344 Mg ha^{-1}).

578 2.1.4 Summary – Wet Tropics

579 Within the Wet Tropics, the AGB is typically underestimated for forests with AGB $> 150\text{-}200$
580 Mg ha^{-1} . This can be attributed to saturation of C- and L-band SAR backscattering, the level
581 of which is generally lower in moist environments, but also because of decrease in L-band
582 backscatter due to increased attenuation of microwaves in denser forests (Mermoz et al.,
583 2015). Hence, using the WCM across the entire range of AGB will result in lower AGB
584 retrievals at the higher end of the AGB range.

585

586 Overestimation of the AGB is common at the lower end of the range ($< 150\text{-}200 \text{ Mg ha}^{-1}$) and
587 is attributed to under-estimation of the attenuation by vegetation (σ_{veg}^0) and overestimation
588 of the backscatter from the ground surface (σ_{gr}^0) in the WCM. In the case of σ_{gr}^0 , the
589 parameterisation utilises bare areas which have different surface conditions in terms of
590 topography, moisture and roughness as compared to the ground under the forest canopy.

591

592 The GlobBiomass product shows greater uniformity in AGB across the DRC than LiDAR-
593 derived maps (i.e., Xu et al., 2017), which could be attributable to the use of median filtering
594 to remove striping applied to dense forest [RD-8]. Nevertheless, the large differences in the
595 AGB of savannas and humid forests are detected in both products. Furthermore, there is
596 weak or no sensitivity of backscatter to AGB in the upper AGB ranges. Hence, small
597 differences in backscatter can lead to large changes in the estimate of GSV. As a
598 consequence, the pixel scale variability can arise from the residual effect of speckle in the
599 SAR data (due to an insufficient number of looks) or topographic variability particularly in
600 hilly landscapes (as illustrated for Nouragues and Paracou, where variability at the pixel scale
601 only appears in the GlobBiomass product).

602

603 For the retrieval using the WCM with L- and C-band SAR data for the range of AGB $> 150\text{-}200$
604 Mg ha^{-1} , alternative approaches using other data sources will be proposed. To improve the
605 retrieval for AGB $< 150\text{-}200 \text{ Mg ha}^{-1}$, the improvements to be proposed will be common to
606 those suggested in the dry tropics/subtropics. Multi-temporal data from Sentinel-1 C-band
607 SAR as planned are expected to reduce the speckle noise. Multi-temporal L-band SAR data

	Ref	CCI Biomass Product Validation and Algorithm Selection Report		
	Issue	Page	Date	
	1.0	32	10.02.2019	

608 are currently not available but could be exploited in the future (e.g., using ScanSAR data).
609 The use of Japanese L-band scene rather than mosaic data would also facilitate better
610 correction for topography and moisture effects.

611

612 For inundated vegetation, land cover maps could be used to identify areas with high C- or L-
613 band σ^0 but with no or sparse vegetation. These maps (with classes indicative of forest
614 structure as a function of height and cover) can also identify inundated vegetation,
615 particularly that of low to medium density where double bounce scattering leads to an
616 enhanced L-band HV and particularly HH response. The parameterisation of the WCM could
617 be reformulated to account for contributions through this scattering mechanism.

618 2.2 Dry Tropics and Subtropics

619 For the dry tropics and subtropics, the 2010 GlobBiomass map was visually assessed for
620 Mozambique (three regions), southeast Tanzania and South Africa (specifically Kruger
621 National Park; NP). The validity of the map was also assessed against forest inventory (plot)
622 data for several regions (southern Africa, Australian and Guinea-Bissau), for which site-
623 specific allometry relating tree size to AGB was also available. Whilst the GlobBiomass
624 product provides an acceptable representation of AGB, several artefacts were identified,
625 with these relating to variability in soil moisture and topography.

626 2.2.1 Site comparisons (Mozambique, Tanzania and South Africa).

627 **Mozambique**

628 Within the flood plain of Lake Urema in central Mozambique, anomalies in the AGB map
629 were attributed to variability in soil moisture (Böhme et al., 2006) (Figure 12b). The flood
630 plain, which is located within Gorongosa National Park, is treeless and has near zero AGB.
631 However, the AGB of inundated soils in proximity to the lake was estimated to be ~30-40 Mg
632 ha⁻¹. Similar overestimates of AGB were observed in the floodplains of the Limpopo (Gaza)
633 and Zambezi and in wet sugar cane farms in central Mozambique (Figure 15c).

634

635 Topographic variability (at 100-500 m scale) also led to discrepancies in the GlobBiomass AGB
636 map. For example, in the northern end of the Chimanimani mountains, forests with a high
637 AGB on steep slopes were generally well represented, albeit with slight errors in location.

	Ref	CCI Biomass Product Validation and Algorithm Selection Report		
	Issue	Page	Date	
	1.0	33	10.02.2019	

638 However, the areas of bare rock (unvegetated) in the south were associated with an AGB of
639 $\sim 20 \text{ Mg ha}^{-1}$). In this same area, geolocation errors were evident and led to anomalies in the
640 GlobBiomass product (e.g., south of the Chimanimanis).

641

642 **South Africa (Kruger NP)**

643 Within Kruger NP the GlobBiomass AGB product captured many of the spatial patterns
644 expected due to ecological theory and field measurement. This includes the east-west
645 divided (dictated by geology and soil type), and also the north-south gradient (driven by
646 rainfall). However, within several areas, banding in the east-west direction was evident in the
647 GlobBiomass product which may be related to the use of the Landsat-derived canopy cover
648 product for masking forest areas, which is known to have artefacts at low AGB levels, partly
649 caused by the Scan Line Corrector (SLC) off artifact of the Landsat 7 data used to rescale C-
650 band 1 km data to 25 m.

651 **2.2.2 Inventory Data Comparisons (South Africa, Australia, Guinea Bissau and** 652 **Kenya).**

653 **Southern Africa**

654 The SOESAW network inventoried plots (Archibald & Scholes, 2007; Ryan et al., 2011; Muledi
655 et al., 2016; McNicol et al., 2018b; Nieto-Quintano et al., 2018) during the period 2010-2104
656 and AGB was estimated for individual trees using the equations of Chave et al. (2014).
657 Comparison with the GlobBiomass AGB (Figure 13a) showed an underestimation in the
658 GlobBiomass product, albeit within the error ranges provided. An overestimate was evident
659 at the very low ranges of AGB.

660

661

662

663

664

665

666

667

668

669

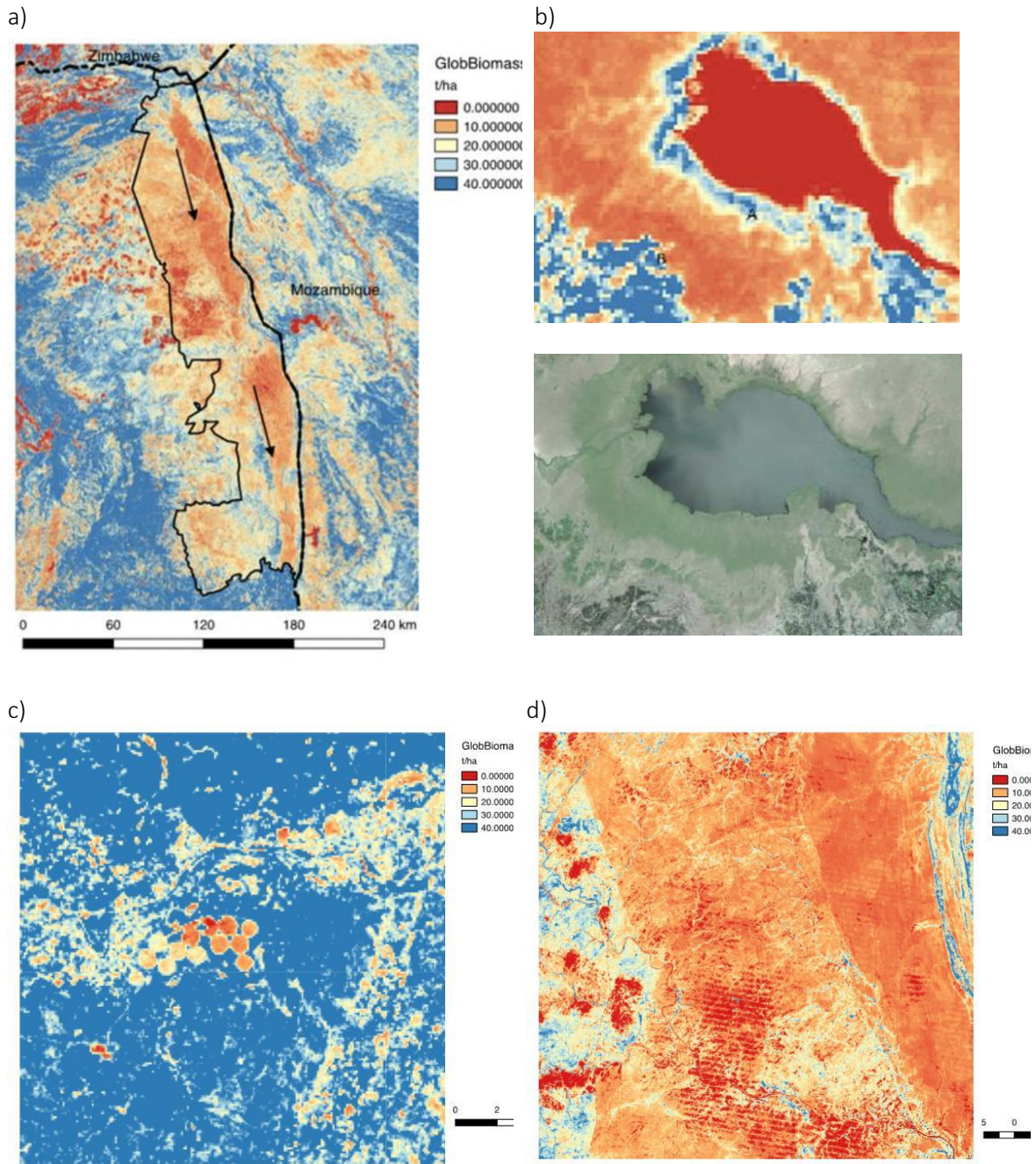
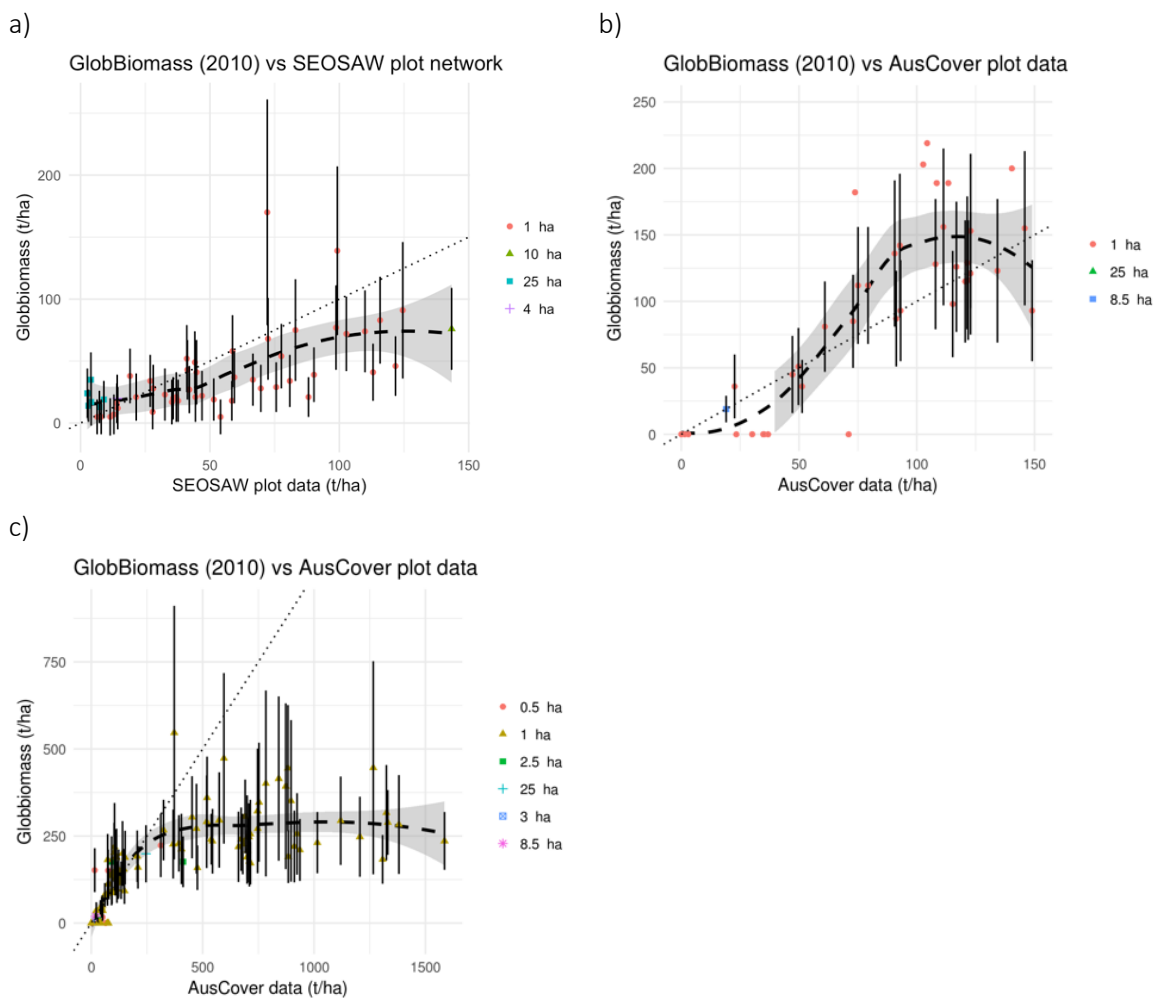


Figure 12. GlobBiomass AGB product for a) Kruger NP (South Africa), b) Lake Urema-Central Mozambique and c) central Mozambique (highlighting overestimation in agricultural (treeless) areas) and d) Kuger NP, South Africa (where banding is evident in the AGB map).

670

671 **Australia**

672 The Terrestrial Environment Research Network (TERN) Australian Plant Biomass Library
 673 (APBL), through the AusCover facility (<http://qld.auscover.org.au/public/html/field/>)
 674 provided estimates of AGB (and associated errors) for 15,706 forest inventory plots
 675 distributed throughout all States and Territories and for all forest types (for the period up to
 676 2015). The AGB was estimated from individual tree measurements (over 2 million) generated
 677 by applying a standardized set of generic equations appropriate to Australian conditions
 678 (Paul et al., 2016). The data were provided by a range of stakeholders and are freely available
 679 for public use. Only data from plots > 0.5 ha and collected after 2001 were used.
 680



681 Figure 13: Comparison of in situ AGB and GlobBiomass AGB for a) southern African savannas (SEOSAW network
 682 (<https://seosaw.github.io>) and b) low biomass forests and c) all forests in Australia (TERN/Ausplots).

	Ref	CCI Biomass Product Validation and Algorithm Selection Report		
	Issue	Page	Date	
	1.0	36	10.02.2019	

683 For wooded savannas (dry tropics and subtropics), areas assigned to zero in the GlobBiomass
684 product were associated with plots with an AGB of $< 40 \text{ Mg ha}^{-1}$, which may be attributed to
685 the tree cover dataset used for masking. An overestimate of AGB in the GlobBiomass product
686 was evident at around 100 Mg ha^{-1} , although this was within the product's error estimate.
687 When the full dataset (all forest types) was evaluated, saturation was observed. It should be
688 noted that some very high AGB estimates were provided in the APBL, with this attributed to
689 small plots focused on a few larger trees but also that stands containing many large
690 individuals are commonplace, particularly in Tasmania, Victoria and Western Australia.

691

692 **Guinea-Bissau (West Africa)**

693 Forest inventory data were collected from 282 20 m radius circular plots between 2007 and
694 2012. Comparison with the GlobBiomass product for a) all plots, b) a subset of 0.1 degree
695 cells encompassing at least 5 plots ($n = 163$) and c) an average of the mapped and reference
696 observations per 0.1 degree cell ($n=18$) highlighted an overestimate of the AGB below 50 Mg
697 ha^{-1} but underestimation above 100 Mg ha^{-1} (Figure 14). Reference AGB observations were
698 updated to 2010 using growth rate data available from the Intergovernmental Panel on
699 Climate Change (IPCC; 2019). A much greater dispersion of the reference AGB observations
700 relative to those mapped using the BIOMASAR algorithm was observed at 0.1 degree
701 resolution. This suggests that the BIOMASAR algorithm was not able to distinguish different

	Ref	CCI Biomass Product Validation and Algorithm Selection Report		
	Issue	Page	Date	
	1.0	37	10.02.2019	

702 levels of AGB at this scale or the area of each reference plot (0.19 ha) was of insufficient
703 accuracy to characterise the AGB.
704

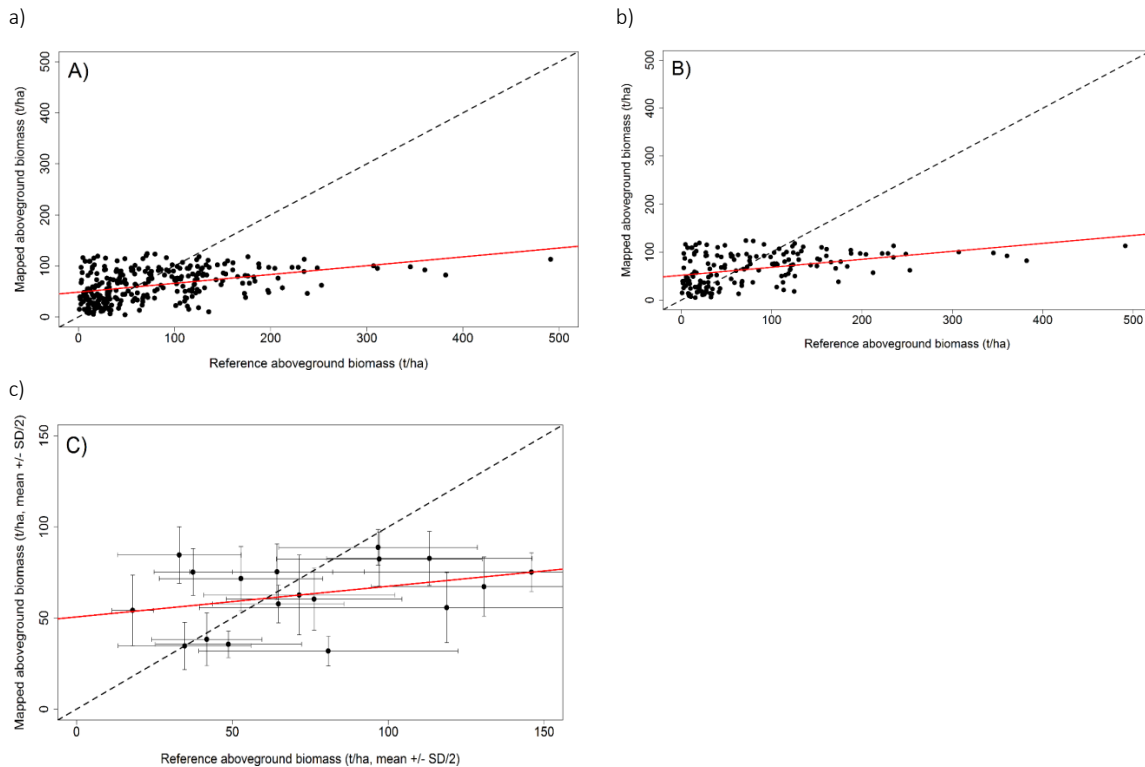


Figure 14: Scatterplot of reference (plot data measured in 2007-2012) vs mapped (100-m GlobBiomass 2010) above-ground biomass in Guinea-Bissau. a) $n = 282$, reference vs. GlobBiomass 2010 observations; b) $n = 163$, reference vs. GlobBiomass 2010 observations; c) $n = 18$, each point representing the average of at least five *in situ* measurements at 0.1-degree scale against the corresponding pixel average from GlobBiomass 2010. The dashed line represents perfect agreement and the red line a linear fit to those observations. The error bars around each observation show half the standard deviation (SD) in the reference (horizontal) and mapped (vertical) datasets.

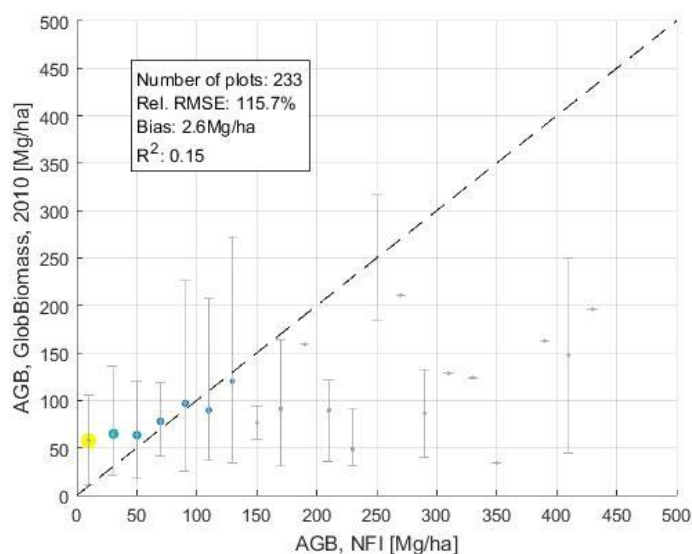
705

706 Kenya (East Africa)

707 Forest inventory plots ($N = 233$) measured in 2014-2016 from different biomes (e.g. humid
708 tropical forests, mangrove, savannah and others) were compared to the estimates from the
709 GlobBiomass AGB map 2010. The plots were circular shaped and have 30 m diameter. The
710 comparison showed overestimation of the algorithm at AGB values below 100 Mg ha^{-1} , and
711 underestimation on higher AGB values.

	Ref	CCI Biomass Product Validation and Algorithm Selection Report	
	Issue	Page	Date
	1.0	38	10.02.2019





712

713

714

Figure 15 Scatterplot of reference (233 plot data measured in 2014-16) vs mapped (100-m GlobBiomass 2010) above-ground biomass in Kenya.

715

2.2.3 Summary - Dry Tropics and Subtropics

716

717

718

719

720

721

722

723

724

725

726

727

728

729

730

731

732

733

Overall, the patterns in the GlobBiomass AGB product match with expected ecological patterns in the dry tropics and subtropics. The ALOS HH and HV backscatter mosaics (Shimada & Ohtaki, 2010; Shimada et al., 2014) provide useful information for estimating the AGB of forests in the dry tropics. However, several artefacts (e.g., terrain and moisture effects) in the data limit retrieval of AGB and are the result of using combinations of wet and dry season imagery, inappropriate histogram matching between paths and imperfect terrain correction by the provider of the ALOS mosaics. Several studies have developed methods to overcome these limitations and produce large area AGB products (Bouvet et al., 2018; McNicol et al., 2018a). Overestimation of the AGB was evident in the very low ranges in southern Africa and Kenya and centred around 100 Mg ha⁻¹ in Australia. Underestimation of the AGB in the GlobBiomass product was evident at the upper end of the range in southern Africa, Guinea Bissau, Kenya and Australia.

The BIOMASAR-L algorithm assumes a relationship between the patchiness of the vegetation and AGB, which relates to the area fill factor (aka canopy cover). Support for this relationship was found in boreal forests (Santoro et al., 2002) and NE USA (Cartus et al., 2012), but it is unlikely to hold in the dry tropics and subtropics where different forces shape landscape patchiness. Indeed, reference to ground data suggested that this relationship was very weak

	Ref	CCI Biomass Product Validation and Algorithm Selection Report		
	Issue	Page	Date	
	1.0	39	10.02.2019	

734 at two sites in Africa. Savanna ecological theory suggests that patchiness is more a function
735 of disturbance intensity (Staver et al., 2011) and edaphic conditions (Woollen et al., 2012)
736 rather than AGB, so an approach that does not assume such a relationship is required. Given
737 the importance of canopy scattering, departures from the assumed canopy cover - AGB
738 relationship have the potential to introduce substantial uncertainty into AGB estimates.

739 2.3 Temperate and Boreal Biomes

740 For the temperate and boreal biome, the global map representative for the year 2010
741 generated during the ESA DUE GlobBiomass project, was visually reviewed for areas in
742 Siberia, Canada, Germany and Poland. Further validation during the ESA DUE GlobBiomass
743 was based on reference data from Alaska, USA, the Netherlands and Sweden. An additional
744 validation was carried out by the Natural Resources Institute of Finland. Overall, the global
745 GlobBiomass map for 2010 was considered to provide a good description of the spatial AGB
746 patterns of the temperate and boreal biome. There were however issues related to
747 overestimation of AGB in low density forests and topographic anomalies associated with the
748 use of the ALOS PALSAR mosaics.

749 2.3.1 Inventory data comparison (Finland)

750 A subset of the 2010 global GlobBiomass map was shared with the Natural Resources
751 Institute, Finland, who performed a comparison with National Forest Inventory (NFI) data for
752 different AGB classes for all forests and for each of the different forest districts in Finland
753 (Figure 16a). An overestimation of AGB was observed in the 0-50 and 50-100 Mg ha⁻¹ AGB
754 classes, but this decreased in the remaining AGB classes (Figure 16b). This is in accordance
755 with findings of the GlobBiomass validation phase. Comparisons for each district (Figure 17)
756 indicated an under-estimation from around 150 Mg ha⁻¹. Whilst differences in the spatial
757 resolution of the AGB map and the size of the NFI plots may have contributed, there is still a
758 qualitative overestimation.

759

760

761

762

763

764

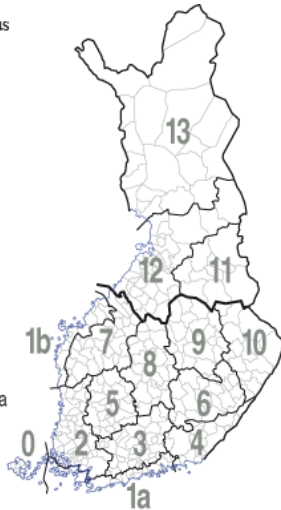
765

	Ref	CCI Biomass Product Validation and Algorithm Selection Report		
	Issue	Page	Date	
	1.0	40	10.02.2019	

a)

Suomen metsäkeskus

- 0 Ahvenanmaa
- 1 Rannikko
 - 1a Etelärannikko
 - 1b Pohjanmaa
- 2 Lounais-Suomi
- 3 Häme-Uusimaa
- 4 Kaakkois-Suomi
- 5 Pirkanmaa
- 6 Etelä-Savo
- 7 Etelä-Pohjanmaa
- 8 Keski-Suomi
- 9 Pohjois-Savo
- 10 Pohjois-Karjala
- 11 Kainuu
- 12 Pohjois-Pohjanmaa
- 13 Lappi



b)

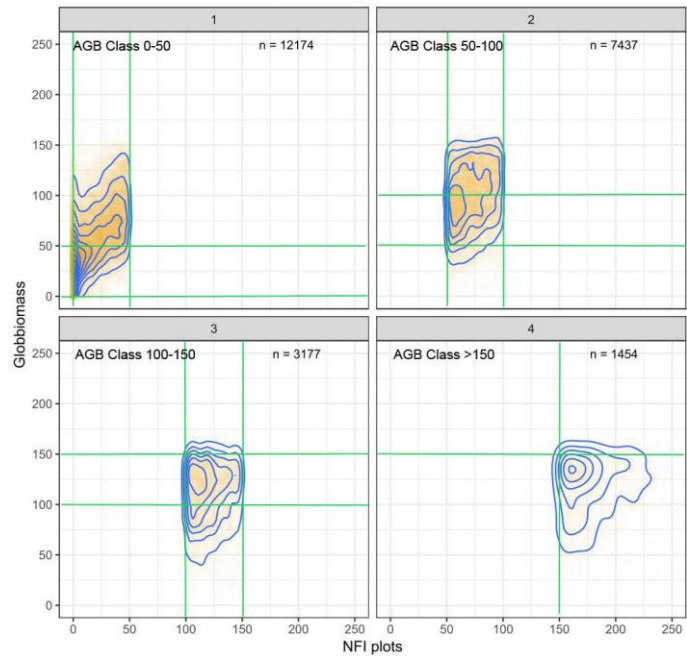
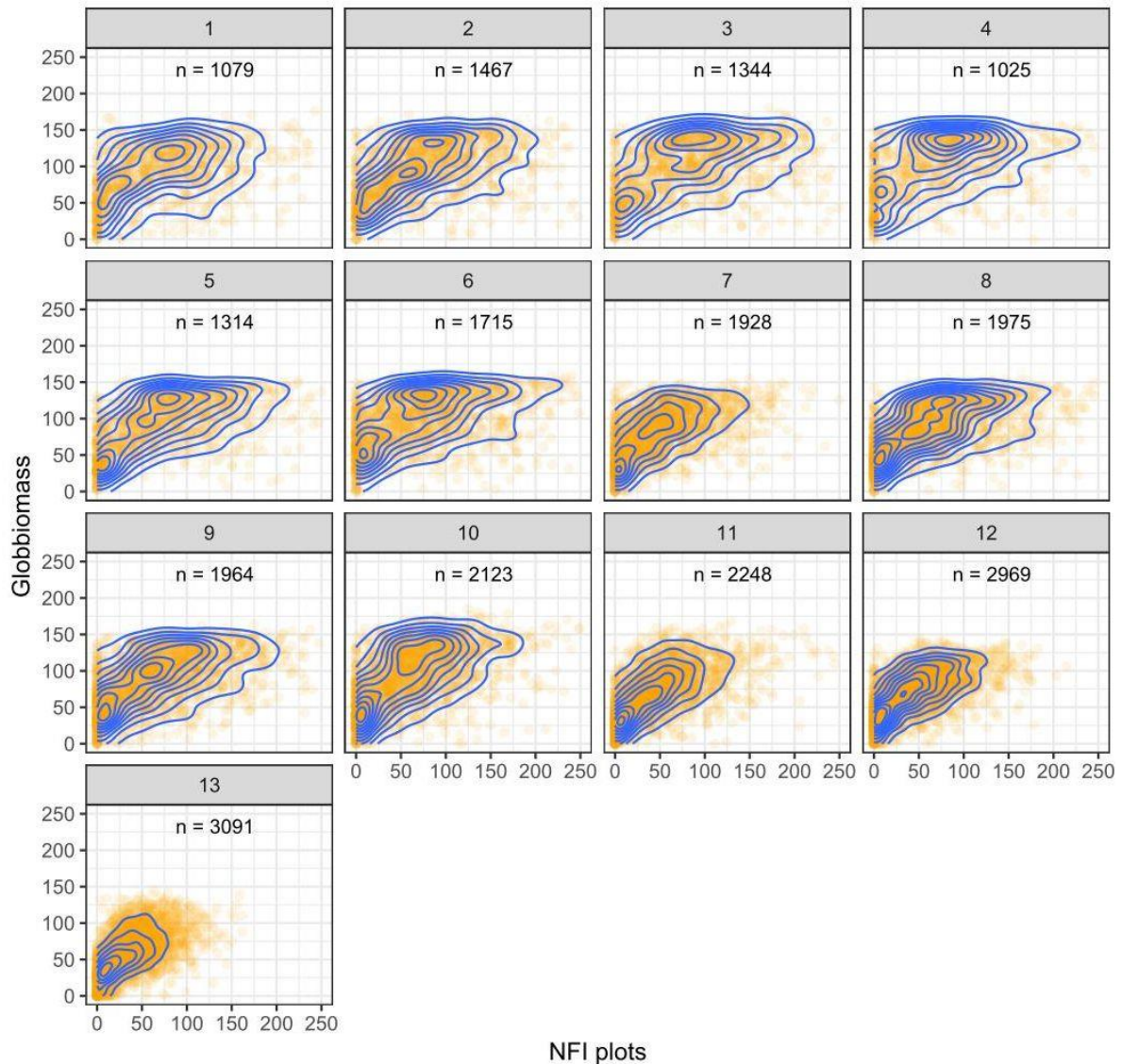


Figure 16. a) Location of forest. Comparison of 2010 Globbiomass map and NFI plots for Finland.

	Ref	CCI Biomass Product Validation and Algorithm Selection Report		
	Issue	Page	Date	
	1.0	41	10.02.2019	



767

NFI plots

768

Figure 17. Comparison of 2010 GlobBiomass map and NFI plots for different regional forest centres in Finland.

769

770 2.3.2 Influence of land cover class

771 A comparison between estimated GSV for different land cover classes (based on CCI Land
772 Cover integrated with canopy height data from Simard et al. (2011)) and the corresponding
773 GSV uncertainties (in %) has been done for all test sites in the temperate and boreal biomes.
774 Classes providing higher GSV values included broadleaved, deciduous, closed to open (>15

	Ref	CCI Biomass Product Validation and Algorithm Selection Report		
	Issue	Page	Date	
	1.0	42	10.02.2019	

775 %) forests (class 60); needle leaved, evergreen closed to open (>15 %) forests), and mixed
776 leaf type (broadleaved and needle leaved) forests. Apart from temperate forests in British
777 Columbia, the GSV error was almost uniformly distributed, with higher uncertainty rates
778 evident in needle-leaved evergreen closed to open (> 15%) classes. For Siberia, the higher
779 GSV uncertainties were associated with shrub classes, sparse mixed vegetation classes and
780 water bodies. This supports the observations of the spatial distribution of high per-pixel
781 uncertainty percentages. Across the boreal/temperate sites, the relative error in retrieved
782 GSV was evenly distributed across most land cover classes, being up to 50 % and between 35
783 and 50 % for the temperate and boreal forests respectively.

784 2.3.3 Summary - Boreal/Temperate Forests

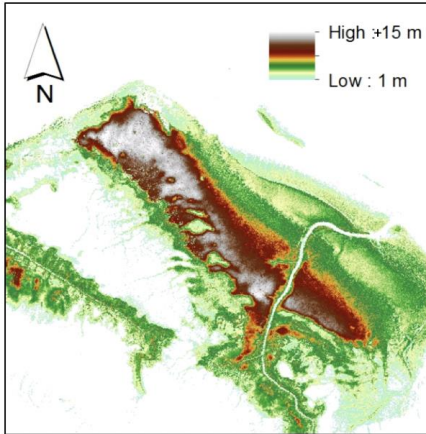
785 In general, the global GlobBiomass map for 2010 gives a good description of the spatial AGB
786 patterns for the temperate and boreal biomes. The main issues with the map for these
787 regions are assumed to be found in the variability in the moisture content of the soil and
788 vegetation (particularly in low but also higher density forests). This leads to inconsistencies
789 in retrieval, overestimation of GSV (and hence AGB) for areas with low-density forest and
790 also where no forest occurs, and artefacts induced by inappropriate compensation of
791 topographic effects (slope and aspect) on the radiometry of ALS/PALSAR data.

792 2.4 Mangroves

793 A recognised limitation of the 2010 GlobBiomass AGB map was the underestimation of the
794 AGB of mangroves above $\sim 100 \text{ Mg ha}^{-1}$ and particularly for taller forest stands in the tropics
795 and subtropics. Several studies in Australia and Southeast Asia (see Lucas et al., 2007) have
796 associated lower backscatter at L-band HH and, to a lesser extent, HV with taller mangroves
797 dominated by *Rhizophora* species (Lucas et al., 2007) due to the large size and complex
798 geometry of their prop roots. For example, Asbridge et al. (2016) observed a reduced L-band
799 HH and HV backscatter over *Rhizophora*-dominated mangroves $\geq 10 \text{ m}$ at the mouth of the
800 Leichhardt River in Queensland Australia (Figure 18a,c). Lucas et al. (2007) observed a similar
801 low response in Kakadu National Park in Australia's Northern Territory for forests $\geq 10 \text{ m}$
802 dominated by *Rhizophora* species but also noted a decrease in L-band HH and HV backscatter
803 with increases in AGB (Figure 18b,c).

804

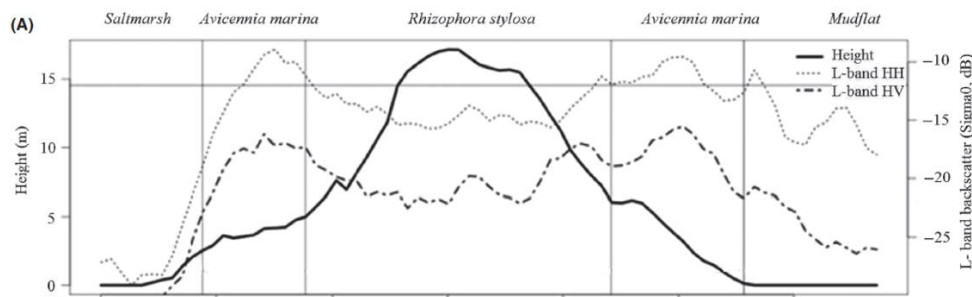
a)



b)



c)



d)

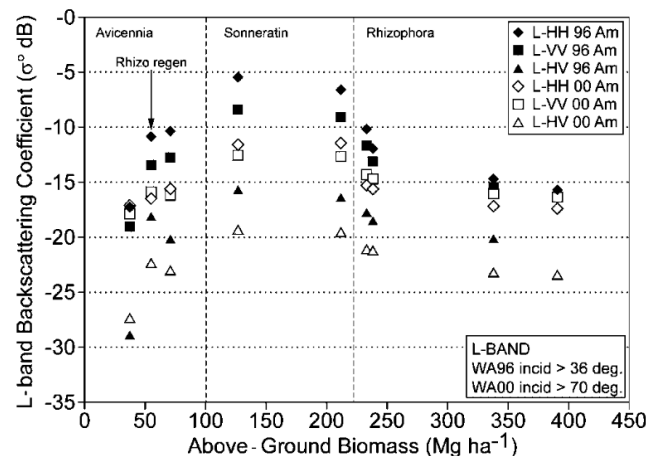


Figure 18: LiDAR-derived CHM for mangroves at the mouth of a) the Leichardt River and b) West Alligator River (Kakadu NP), Australia. In both cases, the taller (> 10-15 m) forests are dominated primarily by *Rhizophora stylos*. c) Differences in ALOS PALSAR L-band HH and HV backscatter as a function of canopy height and dominant species, Leichardt River and d) the trend in L-band HH and HV backscatter as a function of dominant species type, West Alligator River, as observed from AIRSAR data acquired at different incidence angles in 1996 and 2000.

	Ref	CCI Biomass Product Validation and Algorithm Selection Report		
	Issue	Page	Date	
	1.0	44	10.02.2019	

805 Both L-band HH and HV backscatter increased with AGB where this was $< \sim 100 \text{ Mg ha}^{-1}$ and
806 the forests were dominated by *Avicennia*, *Sonneratia* and regenerating *Rhizophora* species
807 (which lacked large prop roots). A lower L-band HH and HV response was observed for
808 *Rhizophora*-dominated mangroves in the Matang Mangrove Forest Reserve (MMFR) in Perak
809 State, Peninsular Malaysia (Lucas et al., 2019). Following commercial harvesting of the
810 mangrove forests, an exaggerated L-band HH and HV backscatter was observed (Figure 19),
811 which would contribute to an overestimation of AGB where these data are used in retrieval
812 algorithms. The L-band backscatter is also enhanced following dieback or where more
813 canopy and tidal inundation (at the time of the satellite acquisitions) occur.

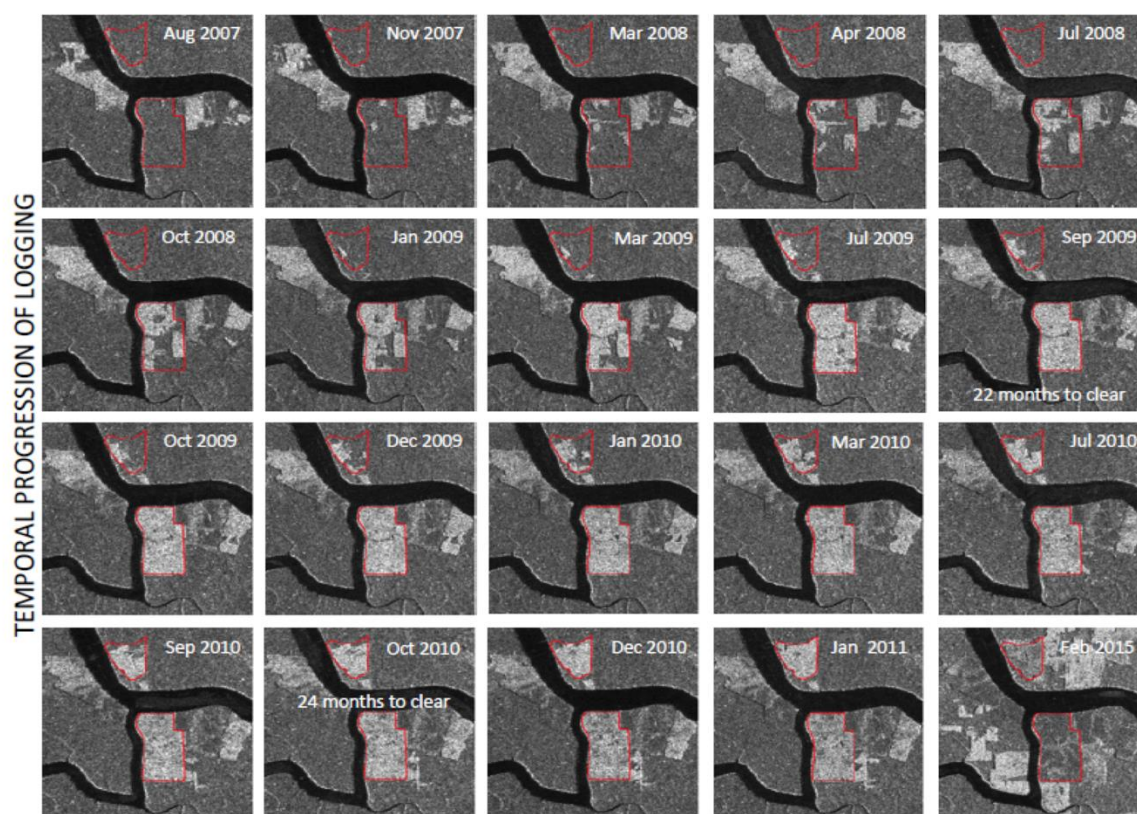
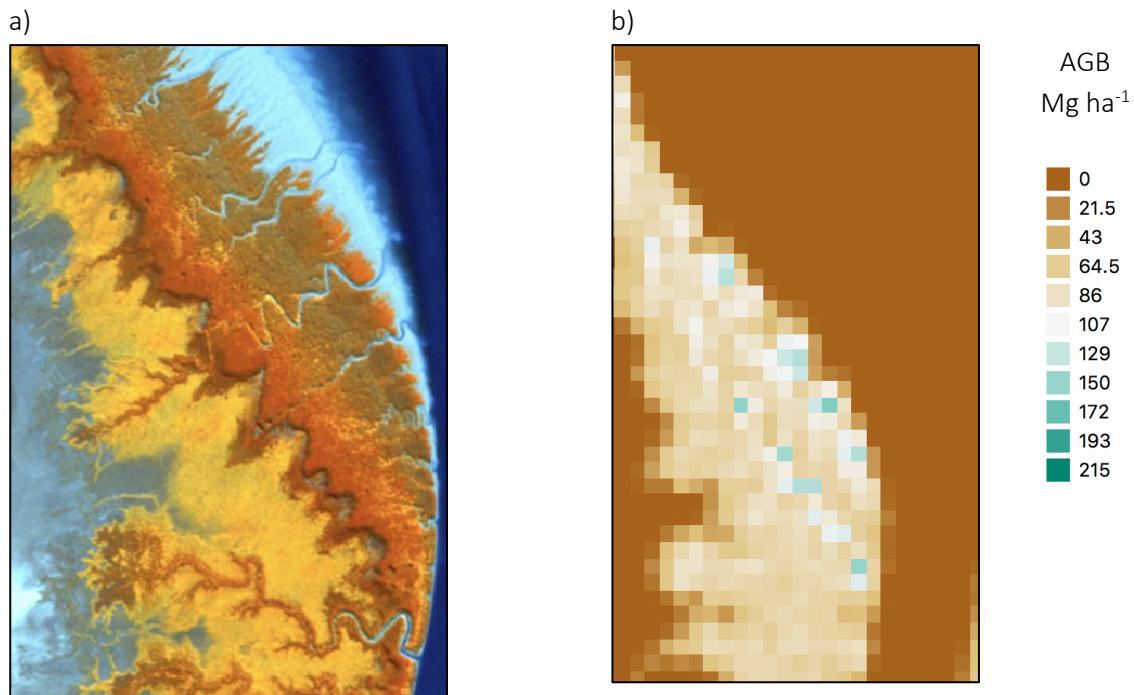


Figure 19: The enhanced L-band HH backscatter (white) following commercial harvesting, Matang Mangrove Forest Reserve (MMFR), Malaysia. Note the gradual return of the backscatter to pre-disturbance levels.

814
815 Comparison of the GlobBiomass product against *in situ* (including airborne sensor) data
816 confirmed both underestimation and overestimation of AGB using the GlobBiomass
817 algorithm at higher and lower AGB levels respectively. As an illustration, the AGB of the taller
818 mangroves dominated by *Rhizophora* species in Kakadu NP was underestimated, with the

	Ref	CCI Biomass Product Validation and Algorithm Selection Report		
	Issue	Page	Date	
	1.0	45	10.02.2019	

819 GlobBiomass map indicating an AGB of $< 90 \text{ Mg ha}^{-1}$. Field measurements indicate an AGB of
820 $> \sim 225 \text{ Mg ha}^{-1}$ (up to 375 Mg ha^{-1} ; Figure 20).



821 Figure 20: a) RapidEye image (near infrared, red edge and blue in RGB) of mangroves along the West Alligator
822 river showing taller mangroves dominated by *Rhizophora stylosa* (orange) and shorter mangroves dominated
823 by *Sonneratia alba* (seaward; olive) and *Avicennia marina* (landward, yellow). b) The corresponding
824 GlobBiomass AGB map showing lower AGB retrieved for the taller *Rhizophora*-dominated mangroves.

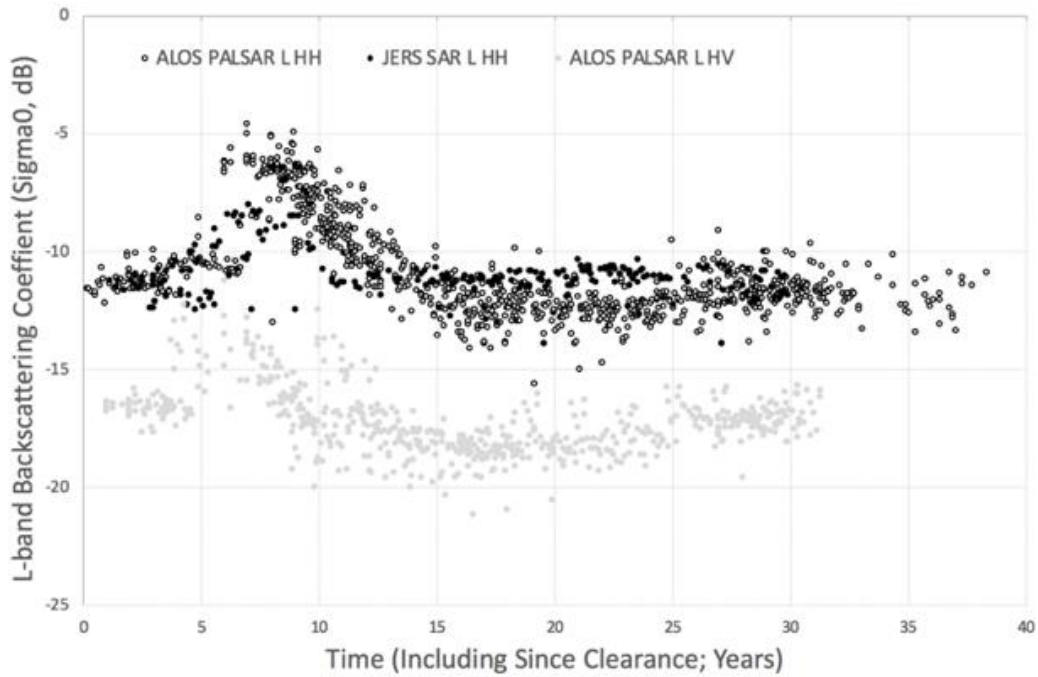
825 Within the commercially harvested areas of the MMFR in Malaysia, a rapid increase in the L-
826 band HH and HV backscattering coefficient was observed following clearance, with this
827 attributed to woody debris lying on the cleared areas (Figure 21a). The L-band HH and, to a
828 lesser extent, HV data were exaggerated compared to the pre-logged forest within all dates
829 of JERS-1 SAR, ALOS PALSAR and ALOS-2 PALSAR-2 acquisitions, but decreased to levels
830 equivalent to the pre-logged forest within 6-8 years (Lucas et al., 2019).

831
832 For these same forests, the AGB was estimated from a TanDEM-X CHM using the power
833 relationship relating these two variables (Fatoyinbo et al., 2018) that was based on the
834 allometry of Komiyama et al. (2008) where:

835
836
$$AGB = 0.07 * LH100^{2.83} \quad (1)$$

837

a)



b)

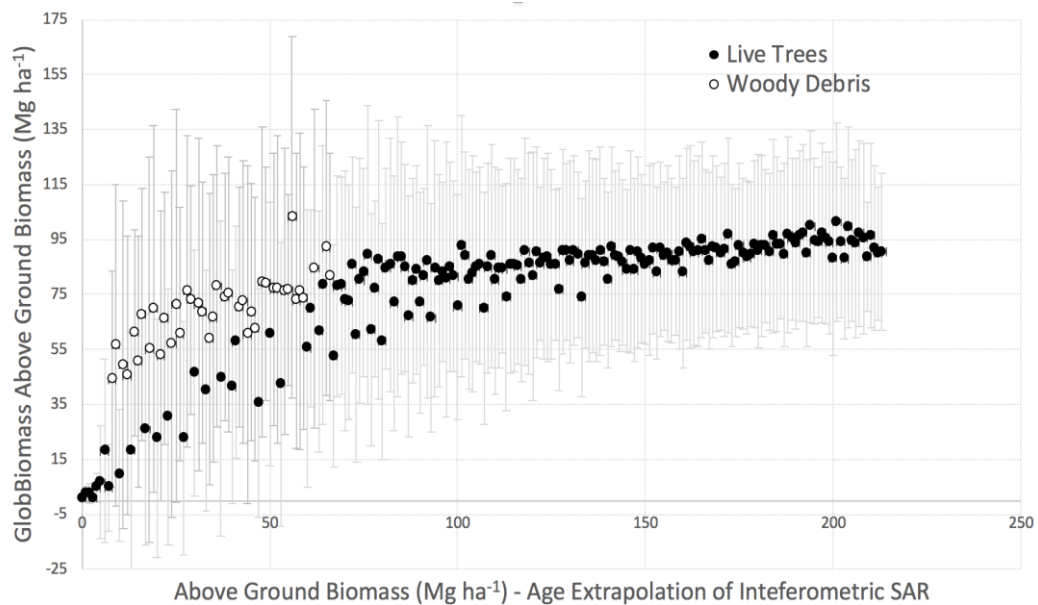
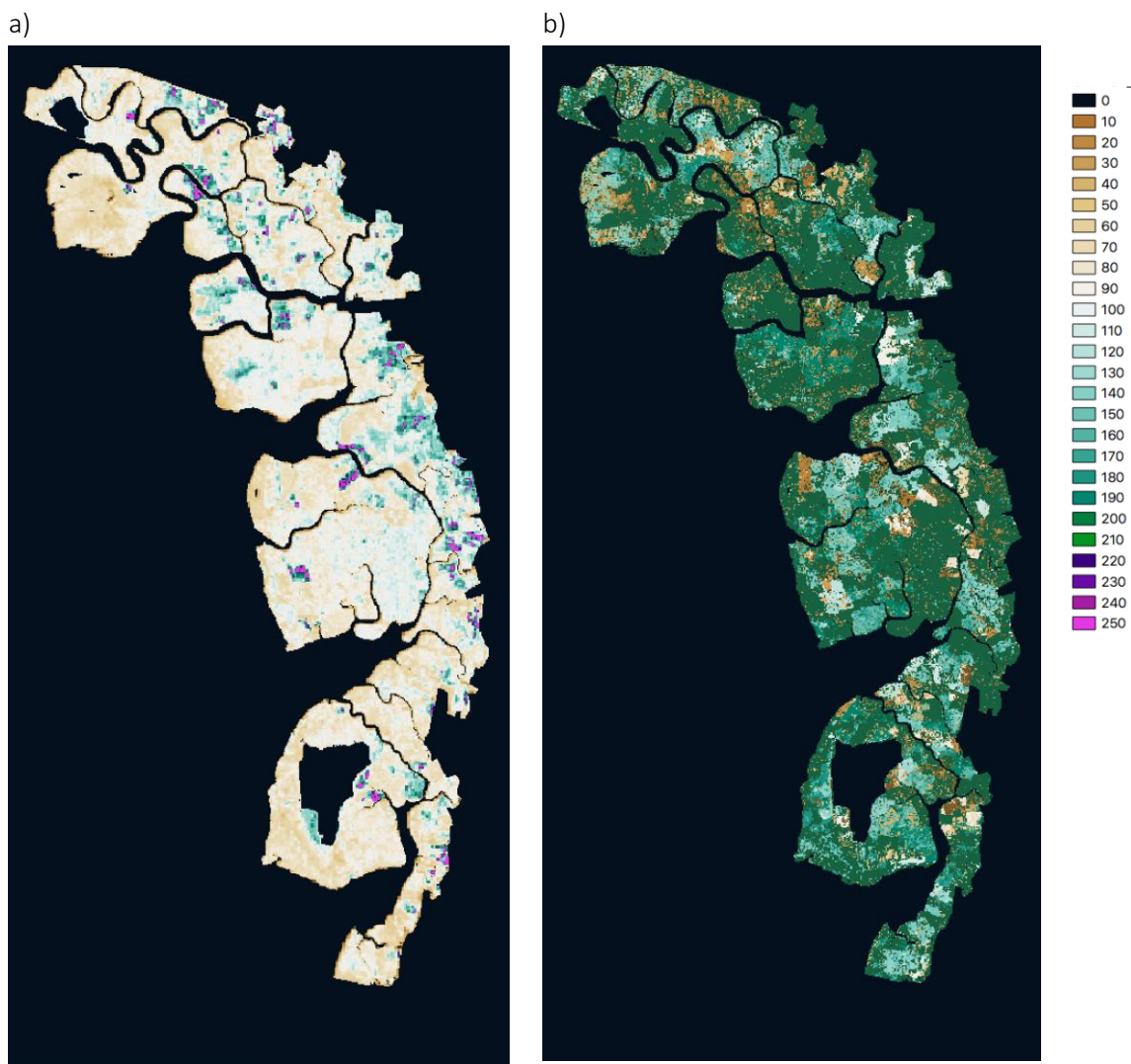


Figure 21: a) The trend in L-band HH and HV backscatter prior to and following commercial harvest of Rhizophora-dominated forests, MMFR, Malaysia. B). The correspondence between the AGB estimated for 2010 using the BIOMASAR algorithm and from age-adjusted TanDEM-X CHM.

	Ref	CCI Biomass Product Validation and Algorithm Selection Report		
	Issue	Page	Date	
	1.0	47	10.02.2019	

838 Comparison of the resulting AGB estimates against those generated using the GlobBiomass
839 algorithm (based on data extracted from 1 ha grid cells overlaying mangrove areas) indicated
840 a correspondence up to about 100 Mg ha⁻¹ but then no discrimination above this level. By
841 contrast, the AGB estimated from the TanDEM-X CHM was estimated to be 215 Mg ha⁻¹ (the
842 maximum estimated for production forests regenerating from previous logging under a 30-
843 year rotation cycle). The GlobBiomass algorithm also overestimated AGB where woody
844 debris occurred within 100 m grid cells (Figure 21b), noting that all cells were comprised of
845 mixtures of cleared and standing forest. A comparison of the maps generated using the
846 BIOMASAR algorithm and the TanDEM-X DSM is given in Figure 21.



847 Figure 22: Estimates of AGB for the MMFR, Malaysia, based on a) the GlobBiomass algorithm and b) the age-
848 adjusted TanDEM-X CHM.

	Ref	CCI Biomass Product Validation and Algorithm Selection Report		
	Issue	Page	Date	
	1.0	48	10.02.2019	

849 3 Generic Issues

850 A number of generic issues associated with the GlobBiomass AGB product can be relate to a)
851 use of the Global Ecological Zones (GEZ) for stratifying estimates of WCM models; b) the
852 WCM (relating to vegetation and ground scattering, prevailing environmental conditions and
853 topography, particularly sloping terrain); d) conversion of GSV to AGB using wood density
854 and Biomass Conversion & Expansion factors (BCEF), f) existing knowledge surrounding the
855 spatial distribution of AGB and also forest types as a function of structure, floristics and
856 function.

857 3.1 The Water Cloud Model

858 3.1.1 Model Overview

859 The BIOMASAR algorithm used in the GlobBiomass product utilizes observations of the SAR
860 backscatter to retrieve GSV and is based on a WCM with gaps. AGB is estimated from GSV
861 using information on wood density and BEF. The BIOMASAR algorithm considers
862 contributions from both the ground (forest floor; σ_{gr}^0) and vegetation (volume scattering;
863 σ_{veg}^0) such that:

864

$$865 \sigma_{for}^0 = \sigma_{gr}^0 T_{for} + \sigma_{veg}^0 (1 - T_{for}) \quad (2)$$

866

867 where

$$868 T_{for} = (1 - \eta) + \eta e^{\frac{-2K_e h}{\cos\theta}} = \exp(-\beta V) \quad (3)$$

869

870 σ_{for}^0 quantifies scattering from forest and β and V describe the two-way attenuation
871 (transmissivity) and GSV respectively. Hence, σ_{for}^0 is governed by the distributions in size,
872 density, orientation and moisture content of plant material within the volume space
873 occupied by vegetation, and the underlying topography and ground (underlying vegetation,
874 surface roughness and soil moisture – note that the dielectric properties of vegetation are
875 linked to the temperature and freeze/thaw state). The parameterisation of the WCM should
876 consider all of these, which have variable contribution to the radar backscatter within biomes
877 and forest types. The following sections outline key issues associated with these and relating

	Ref	CCI Biomass Product Validation and Algorithm Selection Report		
	Issue	Page	Date	
	1.0	49	10.02.2019	

878 to parameterisation of the WCM, many of which might be addressed using a number of
879 additional data layers [RD-3].

880 3.1.2 Vegetation

881 Use of Global Ecological Zones

882 Within the WCM, the GEZ dataset was used as a means of stratifying some of the WCM
883 parameters in the BIOMASAR retrieval and the original vector dataset was rasterized to a
884 0.01° in latitude and longitude grid with capacity to be replicated at different spatial
885 resolutions. However, the classes defined are too broad to allow fine tuning of the retrieval
886 algorithms and hence improved classification and delineation of vegetation is required which
887 also incorporates ecological properties of the landscape. For example, there is a better need
888 to:

889

890 a) Constrain GSV estimates based on knowledge of the densest forests, particularly
891 where these are difficult to identify (e.g., in the dry tropics and sub-tropics) and to
892 also identify transitions between ecosystems, whether these be relatively abrupt (as
893 in the case of the tropical forest/savanna transitions in Amazonia and central Africa),
894 or gradual (as in Australia where there is a climate-driven increase in structural
895 magnitude (size and cover) from inland towards the coast in many regions.

896 b) Capture the global variability in transmissivity as a function of forest type.

897

898 Constraining GSV

899 The BIOMASAR algorithm requires information on the maximum GSV in order to constrain
900 the retrieval to a realistic range of AGB. This currently relies on the use of existing spatial
901 datasets of GSV for the densest forests (i.e., maximum GSV), an empirical piece-wise linear
902 function (Santoro et al., 2015) based on an average reported GSV as well as *in situ* data, and
903 otherwise from the IIASA FAO 0.5° global GSV dataset [RD-8]. The approach is, however,
904 limited in transitional forests but also in the dry tropics where the forests with highest
905 backscatter may be relatively open and hence scattering contributions from the ground may
906 be significant. The GSV estimates and conversion values themselves are also associated with
907 errors.

908

909 Transmissivity

910 In Santoro et al. (2011), the range of plausible values for β in the boreal biome was
911 investigated, and a constant value of 0.006 ha m⁻³ was proposed. This assumption, which
912 may be valid in old growth forest, but may not be adapted to forest of different growth

	Ref	CCI Biomass Product Validation and Algorithm Selection Report		
	Issue	Page	Date	
	1.0	50	10.02.2019	

913 stages, and in other biomes where the effect of vegetation structure becomes significant.
914 This will lead to over- or underestimation of AGB in different biomes and as a function of
915 forest structure (and hence canopy density and height). Whilst this simple formulation
916 allowed the generation of a GSV and AGB map (estimated from wood density and BCEF), the
917 approximation assumes that there is the same attenuation from very low to high AGB. The
918 attenuation in the WCM is expressed as a product of the number of water droplets per unit
919 volume to the attenuation cross section of a single droplet, and because N varies with the
920 forest structure. The assumption is expected not to apply to forests with a large range of AGB
921 (e.g., those with young regrowth and old growth).

922 3.1.3 At-Ground Surface States and Structures

923 In GlobBiomass, σ_{gr}^0 is estimated as the median backscatter of pixels labelled as ground
924 within a window centred on the pixel of interest (Santoro et al., 2011). The window is
925 enlarged until at least 2 % of the pixels are labelled as "ground". The window size is limited
926 by an upper threshold varying between 50 and 150 pixels, which depends on the proportion
927 of unvegetated areas within the study region. Pixels are labelled as "ground" when the
928 percentage tree cover in the MODIS VCF product is below a spatially adaptive threshold (15
929 % up to 30 %).

930

931 This procedure assumes that the backscatter of the forest ground floor is the same as the
932 backscatter of bare ground (located up to 150 pixels from the forest). The assumption is very
933 coarse and could be an important source of error in AGB. The forest ground floor might not
934 present the same properties as the bare ground, since it is a soil that is under different
935 conditions of humidity, sun exposure, presence of organic matter and the biochemical
936 processes associated, etc. Furthermore, areas of 'bare ground' might be associated with
937 structured surfaces such as coarse woody debris following deforestation, rocks or buildings,
938 noting here that many areas that have remained forested are on poorer quality land and
939 often hilly terrain compared to those exploited for agriculture.

940

941 Similarly, σ_{veg}^0 is estimated from the measure of the backscatter of the densest forest within
942 a window, together with a compensation factor reflecting a residual ground backscatter of
943 the dense forest and the finite depth of the canopy. In the dry tropics, the densest forest
944 within a window could be of medium AGB values, not adapted to the WCM formulation for
945 which the backscatter tends toward this maximum σ_{veg}^0 .

	Ref	CCI Biomass Product Validation and Algorithm Selection Report		
	Issue	Page	Date	
	1.0	51	10.02.2019	

946 **3.1.4 At Surface and Within Volume Environmental Conditions**

947 Within the SAR data, significant striping was observed, attributed to differences in
 948 environmental conditions at the time of the overpass, with these including soil moisture,
 949 vegetation moisture (as a function of precipitation but also plant lifeform), freeze/thaw
 950 conditions, tidal inundation and fire. These effects have high impacts in the dry
 951 tropics/subtropics and boreal regions but may occur in any location.

952

953 Within low density forests and for all biomes (but particularly the dry tropics and subtropics),
 954 an increase in C- and L-band SAR backscatter occurs as a result of soil moisture and/or surface
 955 moisture (e.g., following rainfall events). Variations in soil moisture have been found not to
 956 be correlated to C-band backscatter for temperate high-density forest (see above). For the
 957 latter case variations in σ_{gr}^0 need to be accounted for, for example by establishing statistically
 958 the range of variations observed with Sentinel-1.

959 **3.2 Topographic Effects**

960 Analysis of the relation between terrain slope and estimated GSV presented in D24 of the
 961 ESA DUE GlobBiomass showed that there is an influence of topography on the GlobBiomass
 962 GSV/AGB values, which is attributed to the influence of insufficient topographic correction
 963 of the ALOS PALSAR mosaic data. A limitation of using the L-band SAR mosaics in particular
 964 is that topographic effects cannot be corrected for, both in terms of radiometry and
 965 geometry. This was particularly noticeable on sloped terrain and translated to higher and
 966 lower estimates of GSV (translated to AGB) on slopes facing towards and away from the SAR
 967 respectively (Figure 23). Validation of AGB maps for steeper terrain is also often limited as
 968 most forest plots are located on comparatively level land.

969

970

971

972

973

974

975

976

977

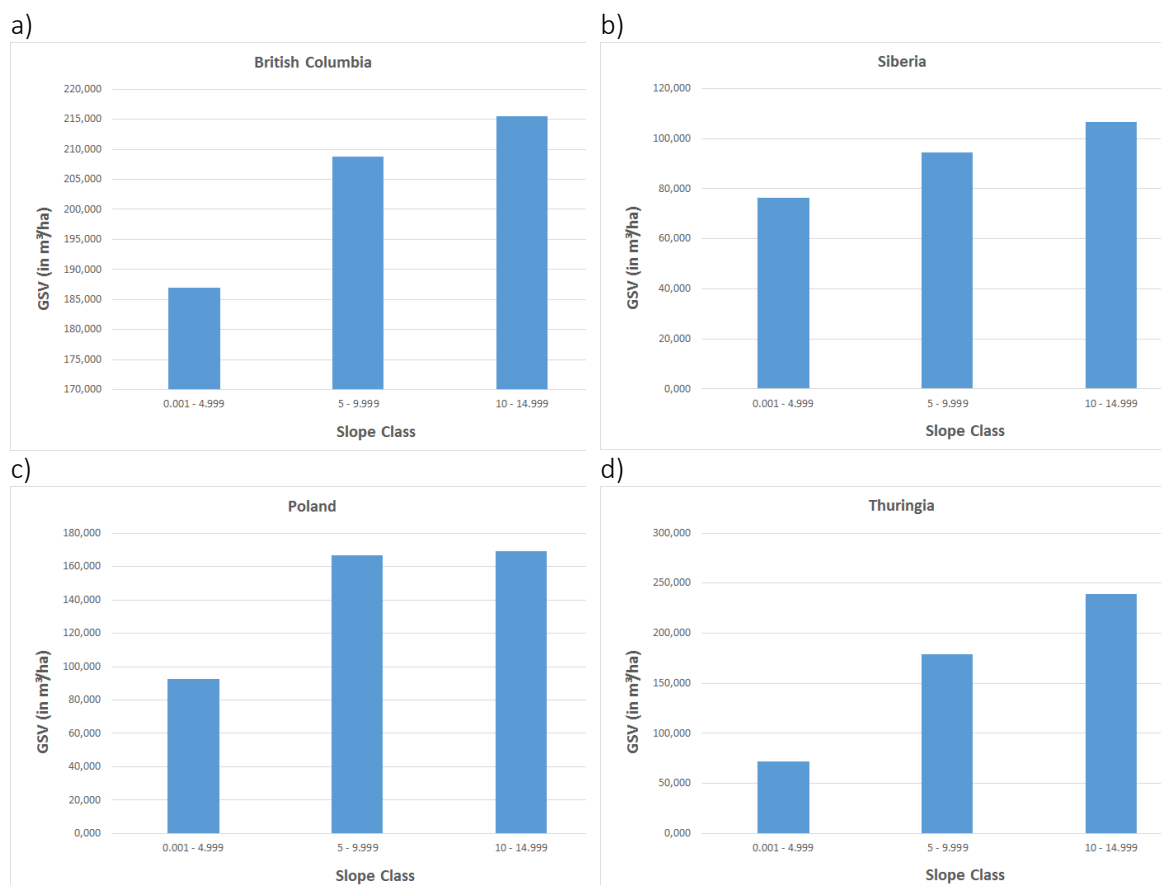


Figure 23: Influence of the slope on the GSV estimation for test sites in the boreal (British Columbia, Siberia) and the temperate (Poland, Thuringia) biomes.

978 3.3 Conversion of GSV to AGB

979 Conversion of GSV to AGB requires both wood density and BEF values. However, these vary
 980 as a function of environmental conditions, which also affect biological processes.
 981 Furthermore, the allocation of BCEF for the same plant species (as well as wood density) may
 982 vary as a function of environmental conditions.

983

984 The BIOMASAR algorithm assumed that AGB could be expressed as a function of GSV and the
 985 use of GSV was supported by its extensive reporting in many countries (FAO 2010 Forest
 986 Resources Assessment; FRA). For forests with multiple tree species and growth stages,
 987 deriving a single wood density and a single BEF value at a given spatial resolution is not
 988 straightforward, and can cause large errors in the conversion.

	Ref	CCI Biomass Product Validation and Algorithm Selection Report		
	Issue	Page	Date	
	1.0	53	10.02.2019	

989 3.4 Knowledge of AGB Distributions Globally

990 Whilst the number of regional to global AGB products is increasing, many show considerable
991 disagreement, which leads to confusion in terms of establishing distributions of AGB and
992 where modification of existing or new algorithms should be applied. Comparisons with these
993 existing maps can also lead to incorrect conclusions and interpretation, particularly if errors
994 in the 'correct' occur. For this reason, comparisons against validated reference datasets
995 (e.g., LIDAR) has been proposed through the Committee on Earth Observation Satellites
996 (CEOS) and aligns with the NASA/EDA Multi-Mission Algorithm and Analysis Platform (MAAP)
997 concept, which aims to improve (through collaboration) understanding of global above
998 ground terrestrial carbon dynamics (maap.xyz).

999
1000 Currently, the WCM is parameterised based on the FAO Global Ecological Zones (GEZ)
1001 (Simons, 2001), which are too broad to capture the variability of vegetation structure in some
1002 biomes. Hence, by providing better mapping of the spatial distribution of vegetation by type,
1003 a more informed selection and parameterisation of the models can be made. Consideration
1004 can also be given to the different types of EO data to be used (e.g., for high biomass dense
1005 forests).

1006
1007 To avoid confusion in retrieval of AGB in lower canopy density or non-vegetated areas (e.g.,
1008 water/snow cover), reference to land cover maps is useful. The CCI Land Cover (LC) project
1009 provides annual maps of land cover (1992 to 2015) at 300 m spatial resolution, which can
1010 support identification of such areas. However, whilst the overall accuracy of the CCI-LC map
1011 is 71.5 %, classification errors may be higher for some cover types, particularly where
1012 mixtures occur. For this reason, the integration of data layers acquired at higher spatial
1013 resolution is useful for refining land cover mapping, with these listed in the Data Access
1014 Requirements Document (RD-3) and including, for example, the Global Mangrove Watch
1015 (GMW) maps of mangrove extent (Bunting et al., 2018). Some land cover information can
1016 be obtained from the SAR data themselves and can be used to indicate and areas where AGB
1017 estimation from the SAR image is likely to fail, including urban areas, flooded and irrigated
1018 areas, and croplands (McNicol et al., 2018a), or particularly algorithms can be applied.

1019
1020 Whilst a forest mask is not applied to the GloBiomass product nor the forthcoming CCI
1021 BIOMASS products, many users will confine analyses to the extent of woody (primarily forest)
1022 vegetation and particularly defining forests. For example, where the product is masked with
1023 the Landsat-based tree cover product from Hansen et al. (2013), low levels of tree cover

	Ref	CCI Biomass Product Validation and Algorithm Selection Report		
	Issue	Page	Date	
	1.0	54	10.02.2019	

1024 associated with open savanna, grassland and croplands are often not captured as the
 1025 algorithm struggles to separate trees and grass cover (e.g., McNicol et al., 2018a).

1026 3.5 High Biomass Forests

1027 At a global level, forests containing the largest quantity of AGB are located primarily in the
 1028 wet tropics but also occur in subtropical (e.g., the coastal ranges of eastern Australia and
 1029 Himalayas) and temperate regions (e.g., northwest United States and southern Australia). In
 1030 these areas, AGB was significantly underestimated using the GlobBiomass algorithm, with
 1031 the difference in predicted and actual estimates increasing with AGB.

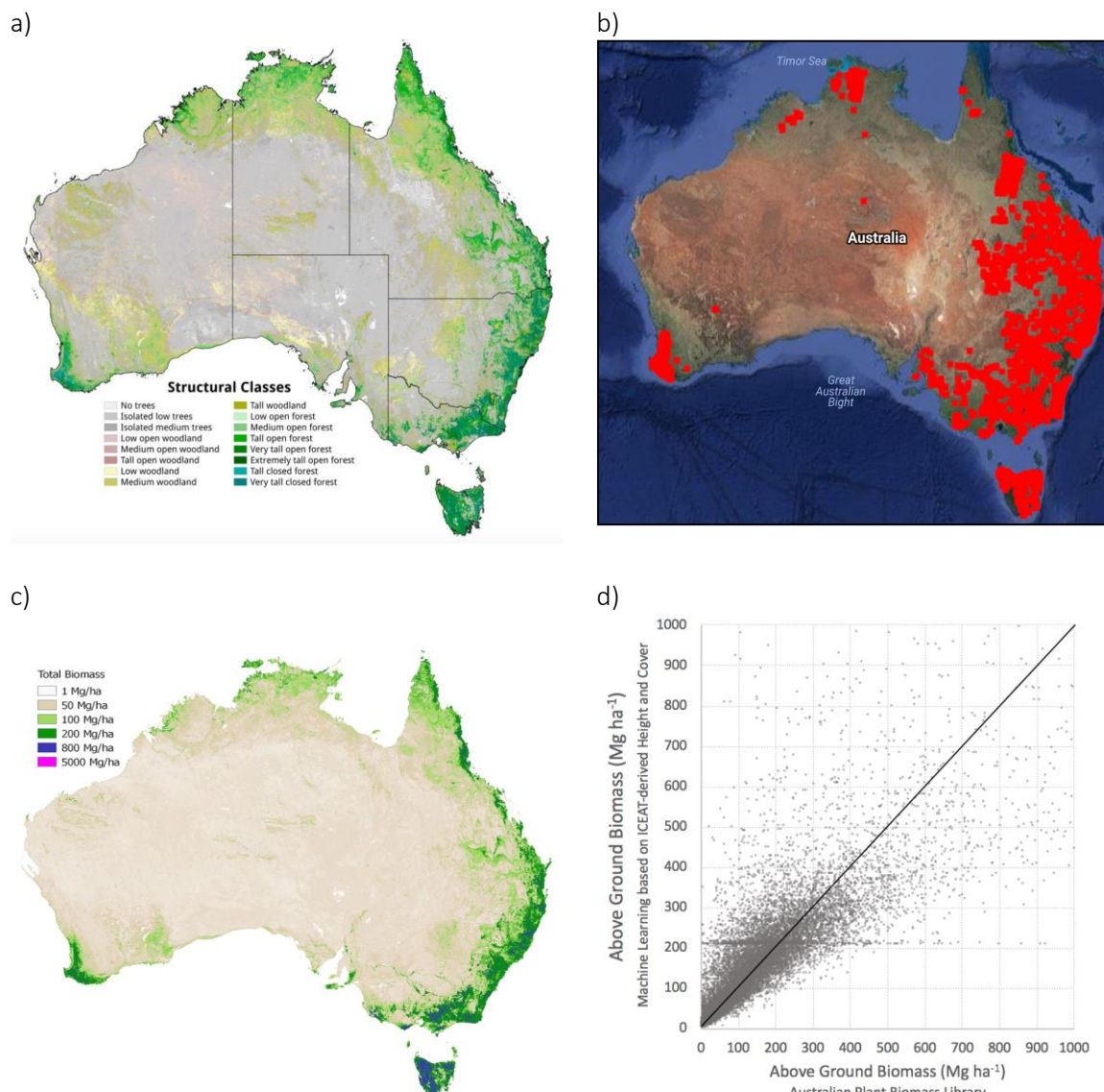
1032
 1033 The benefits of integrating height and cover information for differentiating forest structural
 1034 formation was highlighted by Scarth et al. (2019) for Australia (Figure 24). In this study, the
 1035 Australian landscape was first segmented using ALOS PALSAR L-band HH and HV and Landsat-
 1036 derived vegetation fractional cover and classified using these same data into cover categories
 1037 that were considered to be structurally similar. Each class was then associated with summary
 1038 information on height and cover, as determined from intersecting ICESAT profiles, with this
 1039 information then applied to all non-intersecting segments. A structural classification was
 1040 generated for Australia (Figure 24a) with this based on the schema of the National Vegetation
 1041 Information System (NVIS; referencing the original schema of Carnahan (1970) and Specht
 1042 (1979)). A broad correspondence between the structural classes and the distribution of AGB
 1043 was also observed.

1044
 1045 The information on forest cover and height extracted from each segment (but derived from
 1046 the ICESAT waveforms themselves) as well as 50 % of the APBL dataset (Figure 24b) was then
 1047 used within a machine learning algorithm (MLA) to generate a national estimate of ABG
 1048 (Figure 24c). A close correspondence with the AGB estimated from the 50 % of plots from
 1049 the AGB reserved for evaluating the map (Figure 24d). A comparison of the AGBs generated
 1050 using the BIOMASAR algorithm and MLA highlighted areas of overestimation in flooded
 1051 (riverine) forests and also for low and open woodland (Figure 25). Underestimation was
 1052 evident in higher biomass forests and also mangroves.

1053
 1054 A comparison of the GlobBiomass AGB product with the APBL data indicated poor
 1055 discrimination of AGB levels above approximately 140-150 Mg ha⁻¹ (Figure 26). Whilst the
 1056 MLA provides a good estimation of AGB, *in situ* data are required for training and sufficient
 1057 data of the same quality are not available in many other countries and regions. Hence,
 1058 consideration was given to the information of both canopy height and cover as variables that

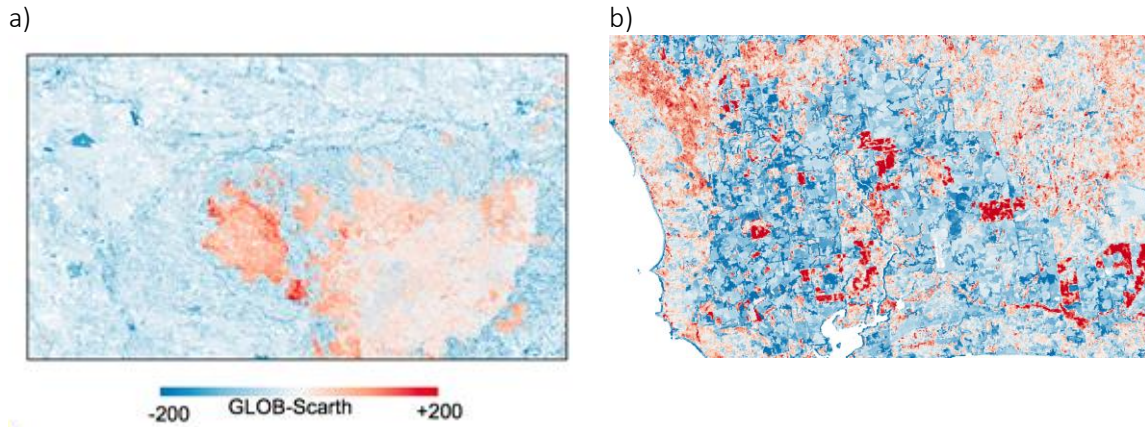
	Ref	CCI Biomass Product Validation and Algorithm Selection Report		
	Issue	Page	Date	
	1.0	55	10.02.2019	

1059 might support global retrieval of AGB. This potential was highlighted when the product of
1060 ICESAT-derived height and cover was compared against the ABPL AGB estimates (Figure 26).
1061 This indicated that higher levels of AGB could be retrieved, noting greater scatter in the
1062 relationship with increases in AGB, but also highlighted overestimation and underestimation
1063 of AGB by the BIOMASAR algorithm.
1064



1065 Figure 24: a) Forest structural formation classification of Australia (Scarth et al., 2019), based structural
1066 formations adapted from Australia's National Vegetation Information System (NVIS), c) the Australian Plant
1067 Biomass Library (APBL) showing plot locations, c) continental AGB estimated using ICESAT-derived height and
1068 cover estimates within a machine learning algorithm (trained using 50 % of samples from the APBL) and d) the
1069 correspondence in the AGB estimated using ML and the APBL (50 % of samples).

	Ref	CCI Biomass Product Validation and Algorithm Selection Report		
	Issue	Page	Date	
	1.0	56	10.02.2019	



1070 Figure 25: Comparison of the AGB map generated using the BIOMASAR algorithm and machine learning using
 1071 ICESAT-derived height and cover for a) northern New South Wales indicating areas of overestimation for low
 1072 and open woodland and b) Western Australia, showing over and underestimation in areas harvested for timber.

1073

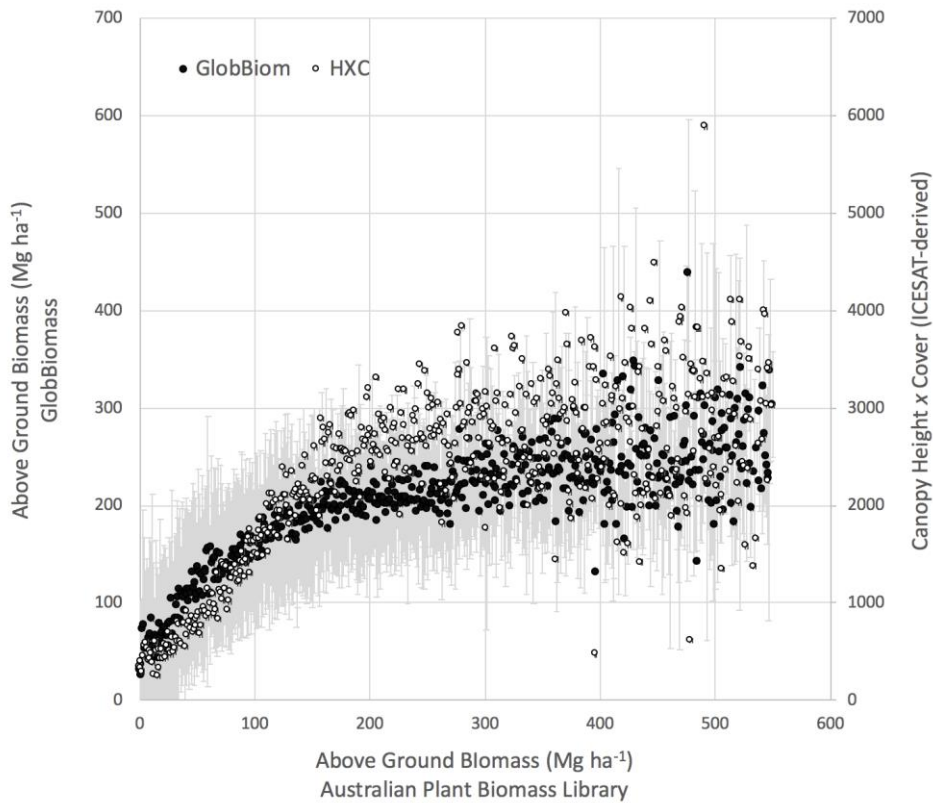


Figure 26: Comparison between the AGB estimated from in situ data (APBL) and the BIOMASAR algorithm. The correspondence between AGB and the product of canopy cover (%) and height (m) is also indicated.

1074

	Ref	CCI Biomass Product Validation and Algorithm Selection Report		
	Issue	Page	Date	
	1.0	57	10.02.2019	

1075 3.6 Summary and Considerations

1076 On the basis of the assessment of the GlobBiomass product against in situ data and other
1077 maps of AGB, consideration of the following is recommended:

1078

1079 a) Preferred access to the unprocessed ALOS PALSAR and ALOS-2 PALSAR-2 (including
1080 ScanSAR) data, thereby allowing optimal selection of images (e.g., during the
1081 selection of dry season images), implementation of selected pre-processing
1082 algorithms (e.g., for topographic slope correction) as demonstrated by Carreiras et
1083 al. (2012), Motohka et al. (2014) and Gou (2017).

1084 b) The issues in using Wood density and BCEF based on existing databases (in general
1085 established for single tree species) cannot be resolved to better account for the 100
1086 m spatial variability of AGB of the product. Consideration should be given to direct
1087 retrieval of AGB rather than estimation through conversion from GSV.

1088 c) Better taking into account the effects of soil moisture at the time of the satellite data
1089 acquisition. Consideration might be given to the soil moisture data from SMOS,
1090 GCOM-W, CCI-Soil Moisture, or the Worldclim Bioclimatic Variables.

1091 d) Using an informed approach to the global classification of forest types based on
1092 structure, function and floristics that builds on the CCI land cover but also provides
1093 more information relevant to forests and land covers (e.g., urban, water) with which
1094 they are often associated. Such knowledge can improve the parameterisation of the
1095 WCM and targeting of where to apply variations of this or new algorithms. This could
1096 be obtained by referencing optical and LiDAR data (e.g., as descriptors of canopy
1097 height and cover).

1098 e) Considering the use of higher spatial resolution to account for mixed forests,
1099 croplands and complex land covers, with consideration given to segmentation of
1100 landscapes (e.g., using Landsat or Sentinel data).

1101 4 Improvements to the GlobBiomass Algorithm

1102 A number of generic and biome-specific improvements are proposed based on the previous
1103 analysis of the GlobBiomass product, with these focusing on refinement of the WCM,
1104 primarily concerning parameterisations relevant to vegetation, the ground surface, surface
1105 states and conditions and surface and within-volume environmental conditions. The use of
1106 *in situ* data in the parameterisation is also considered.

	Ref	CCI Biomass Product Validation and Algorithm Selection Report		
	Issue	Page	Date	
	1.0	58	10.02.2019	

1107 4.1 Improving Soil Moisture component

1108 Moisture in and on the soil and vegetation at the time of the image acquisition leads to
1109 discrepancies in the retrieval of GSV from the WCM, particularly in the dry tropics and
1110 subtropics. However, the BIOMASAR-L algorithm could be adapted to consider soil moisture
1111 or scenes could be selected such that moisture effects are minimised (Lucas et al., 2010;
1112 Bouvet et al., 2018), particularly as consideration of soil moisture effects may reduce some,
1113 but not all, of the artefacts evident in the Japanese L-band SAR mosaic data (Gou, 2017; and
1114 see section below on eWCM-sm).

1115
1116 Potential sources of data are the SMOS or GCOM-W and CCI Soil Moisture products, which
1117 are already publicly accessible and could be used to support adjustment of the WCM-with-
1118 gaps model (Prevot et al., 1993; Xu et al., 1996; Kumar et al., 2012) as the backscatter of bare
1119 ground is often modelled as a linear function of soil moisture. However, the data needs to
1120 be relevant in terms of timeliness and spatial resolution.

1121
1122 For boreal regions, the retrieval of GSV could be based solely on winter imagery. Water
1123 molecules act as dipoles which, during this frozen period, are deactivated and are not able
1124 to follow the oscillations of an electromagnetic field. Hence, the radar backscatter will be less
1125 sensitive to moisture and more so to AGB. In summer, under wetter environmental
1126 conditions, the radar backscatter in these regions will certainly contain information related
1127 to the water content of the surface.

1128
1129

1130

1131 eWCM-sm

1132 Here, we propose a new algorithm, an empirically calibrated L-band WCM with soil moisture
1133 adjustment (eWCM-sm). The goal of this algorithm is to:

- 1134 a) Reduce the soil moisture effects that are particularly prevalent in the GlobBiomass
1135 estimates at low ($<100 \text{ Mg ha}^{-1}$) AGB (see Section 2.3), visible as banding between
1136 different acquisition dates (Lucas et al., 2010), and high AGB estimates in areas with
1137 wet soil (Kasischke et al., 2011)

	Ref	CCI Biomass Product Validation and Algorithm Selection Report		
	Issue	Page	Date	
	1.0	59	10.02.2019	

1138 b) Address the overestimation and lack of sensitivity at low AGB identified in this
1139 document as affecting the dry tropics and sparsely vegetated areas.

1140

1141 The outputs of the eWCM-sm can be used within the GlobBiomass approach by providing a
1142 third input layer (alongside the BIOMASAR-L and -C) to the weighting algorithm, which can
1143 be assessed and weighted using the current criteria [RD-5]. The eWCM-sm is based on an
1144 empirical calibration of the WCM which allows us to relax some of the assumptions inherent
1145 to the GlobBiomass algorithm, particularly those associated with the self-calibration of the
1146 WCM. The advantages of the approach are as follows.

1147 1. There is no need for σ_{gr}^0 to be estimated from low canopy cover pixels within the
1148 search radius. This reduces the dependence on the canopy cover product, which is
1149 known to be inaccurate at low canopy cover and in mixed tree-grass ecosystems
1150 (Gaughan *et al.*, 2013; Amarnath *et al.*, 2017; McNicol *et al.*, 2018a), and avoids
1151 assumptions of homogeneity in the search area.

1152 2. Similar assumptions about the representativeness of the properties of high canopy
1153 cover pixels in the search area are no longer needed

1154 3. The assumption that σ_{gr}^0 in open areas is the same as σ_{gr}^0 below vegetation (i.e., in
1155 forested pixels) is not needed. This is important as the soil moisture conditions in
1156 open areas are often different to wooded areas in ecosystems where the tree layer
1157 is sensitive to water logging (e.g., Woollen *et al.*, 2012)

1158 4. The eWCM makes no assumptions about the relationship between canopy cover (fill
1159 factor, eta) and AGB.

1160

1161 In place of these assumptions are new dependencies on *in situ* and remotely sensed data for
1162 the parameterisation, and new assumptions about the representativeness of the calibration
1163 sites, and the effectiveness of the spatial interpolation.

1164

1165 eWCM-sm is based on a simplified formulation of the WCM.

$$1166 \sigma^0 = A \cdot \cos \theta \cdot \left[1 - e^{\left(\frac{-2B \cdot V2}{\cos \theta}\right)} \right] + e^{\left(\frac{-2B \cdot V2}{\cos \theta}\right)} (C + D \cdot m_s) \quad (4)$$

1167 a) It follows Xu *et al.* 1996 in representing σ_{gr}^0 as a linear function of soil moisture, and
1168 thus ignores other contributors leading to variation of σ_{gr}^0 associated with, for
1169 example, surface roughness

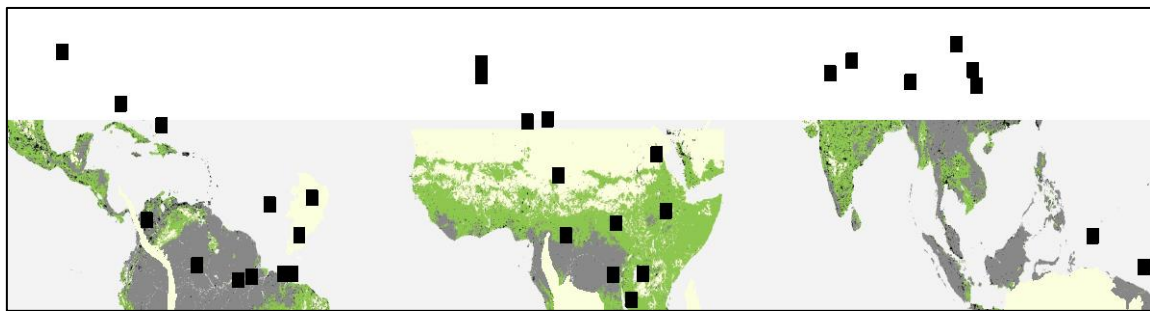
1170 b) V2 is interpreted as woody AGB, not GSV (see discussion below)

1171 c) V1 is ignored (assuming only volume scattering)

	Ref	CCI Biomass Product Validation and Algorithm Selection Report		
	Issue	Page	Date	
	1.0	60	10.02.2019	

1172
1173
1174
1175
1176
1177
1178

A,B,C and D are estimated empirically using a non-linear regression approach implemented in R. This is performed at calibration sites where there are contemporaneous observations of AGB, σ^0 and soil moisture. AGB is known from forest mensuration and the application of suitable allometric equations (e.g. Chave *et al.* (2014) in the tropics); σ^0 is known from ALOS PALSAR 1 or 2 observations and Ms is estimated from e.g. SMOS or ESA CCI soil moisture.



1179

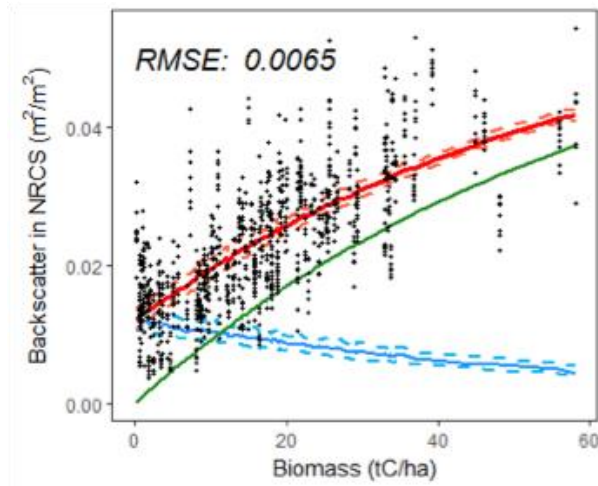
1180 Figure 27: Proposed calibration sites for eWCM-sm in the dry tropics. Calibration sites (□) combines two
1181 regional networks (SEOSAW and DRYFLOR) with data from 22 project partners. At each site plots have already
1182 been established and data collected in the ALOS1 and 2 epochs. Green areas with AGB < 150 t/ha; yellow = arid;
1183 grey = wet tropics. Source:(Avitabile et al., 2015).

1184
1185
1186
1187
1188
1189
1190
1191
1192
1193
1194
1195

A proof of concept using the southern African sites has been conducted (Gou, 2017), which provides an indication of the extent to which the eWCM can achieve the goals set out above. Figure 28 shows the eWCM, parameterised using data from Mozambique, Malawi and Tanzania and illustrates how eWCM partitions the observed σ^0 between the veg and ground contributions. It shows the expected decrease in the soil moisture contribution as woody biomass increases and also (as expected) that at zero biomass, all of the observed σ^0 is attributed to soil. Figure 29 shows the predicted interacting effects of soil moisture and woody biomass on observed σ^0 . An example application of the algorithm, inverting and solving Equation 4 for AGB, shows that the eWCM is able to reduce the banding associated with different acquisition dates of ALOS imagery. This is assumed to be caused by different soil moisture conditions on different dates.

	Ref	CCI Biomass Product Validation and Algorithm Selection Report	
	Issue	Page	Date
	1.0	61	10.02.2019



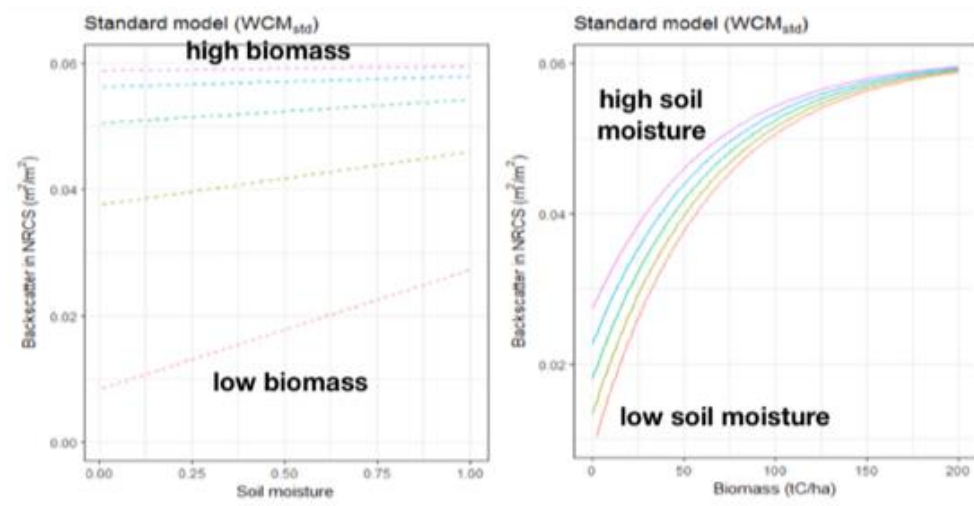


1196

1197 Figure 28: Results of the application of the eWCM in southern Africa. Black dots show observed σ^0 at
 1198 calibration plots. The estimated contribution from the soil is shown in blue and from vegetation in green, with
 1199 the sum (σ^0) in red. Two features consistent with WCM theory are the zero contribution of σ_{veg} at zero
 1200 biomass and the decline in σ_{soil} with increasing biomass. Source: (Gou, 2017)

1201

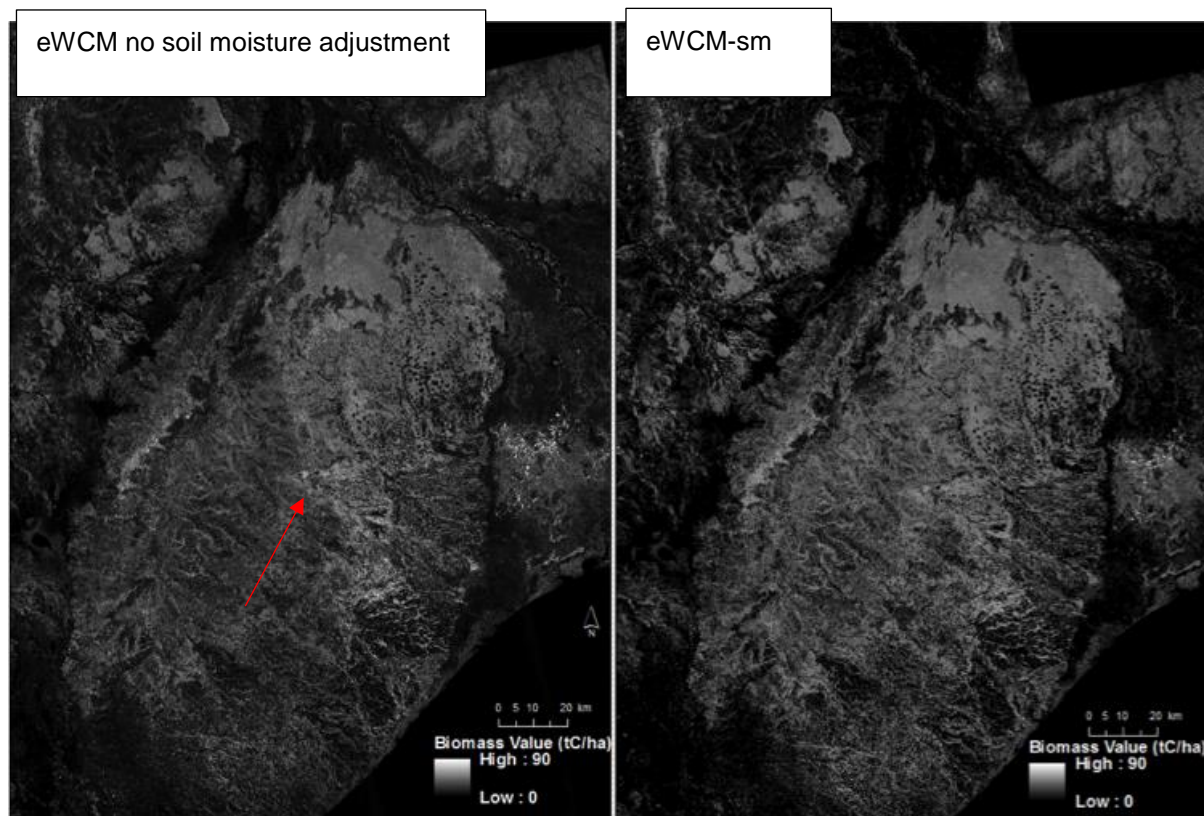
1202



1203

1204 Figure 29: Model predictions of σ^0 for quintiles of biomass (0-200 tC/ha) and soil moisture (0-100%). Source:
 1205 (Gou, 2017)

	Ref	CCI Biomass Product Validation and Algorithm Selection Report		
	Issue	Page	Date	
	1.0	62	10.02.2019	



1206

1207 Figure 30: Example of the application of the eWCM-sm over the Zambezi delta in Marrameu, Mozambique using
 1208 ALOS-1 HV data and ESA's ECV soil moisture product. The soil moisture correction is able to remove the banding
 1209 visible with the eWCM is used with no soil moisture correction. The AOI is 100 km N-S and 70 km E-W. Source:
 1210 (Gou, 2017)

1211

1212 For the pan-tropical (or global) application of the eWCM-sm, a next step is to conduct similar
 1213 analyses as those presented in Figure 28 at a range of sites depicted in Figure 27, to establish
 1214 how consistent the parameter estimates are at each site. This will be achieved using a
 1215 hierarchical (mixed effects) regression model with site nesting within FAO ecozones as
 1216 random effects. This will increase understanding of the extent to which variation between
 1217 and within sites and ecozones contribute to variation in parameter estimation, which can be
 1218 used to guide an effective interpolation scheme.

1219

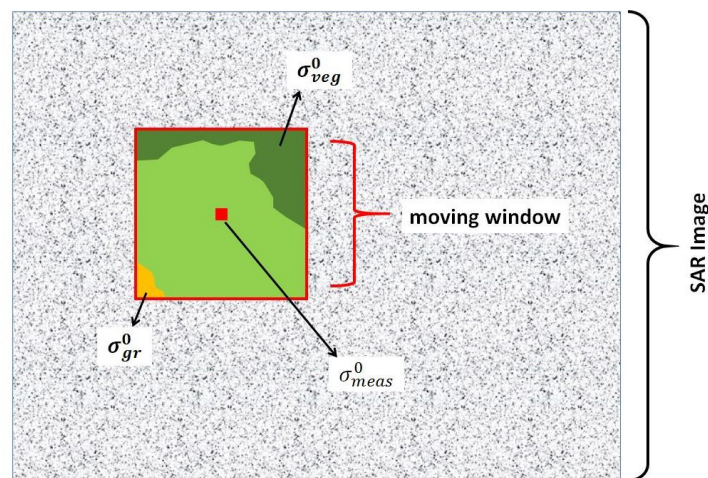
1220 Application of eWCM-sm in boreal and use of moving window

1221 The water content component in σ_{gr}^0 is assumed to cause the overestimation of the GSV and
 1222 has already been validated for dry tropical forests (see above). This assumption can be tested
 1223 in different locations in the boreal biome.

1224

	Ref	CCI Biomass Product Validation and Algorithm Selection Report		
	Issue	Page	Date	
	1.0	63	10.02.2019	

1225 As this method involves multi-temporal data analysis, only multi-temporal C-band data
1226 (ENVISAT for historic studies or Sentinel-1) can be used. This provides a possible answer for
1227 the further development of the BIOMASAR-C algorithm, which accounts for 50-60 % of the
1228 AGB estimation in low-density forest. Upon verification of the above stated assumption, the
1229 following analysis is forseen. In the current BIOMASAR-C algorithm, a moving window
1230 centred at a certain location characterized by the backscatter σ_{meas}^0 , a corresponding σ_{gr}^0 is
1231 estimated (Figure 31). Considering a time series of SAR data, several
1232 σ_{gr}^0 values corresponding to several σ_{meas}^0 values for this specific location will be obtained
1233 with these varying between a minimum and maximum σ_{gr}^0 (Figure 32). For each SAR data
1234 acquisition, a corresponding GSV is estimated. For the final GSV estimate, the BIOMASAR-C
1235 model applies a multi-temporal combination of all GSV values estimated for each SAR data
1236 acquisition over time.
1237
1238



1239
1240 Figure 31: BIOMASAR Retrieval Principle

1241
1242

	Ref	CCI Biomass Product Validation and Algorithm Selection Report		
	Issue	Page	Date	
	1.0	64	10.02.2019	

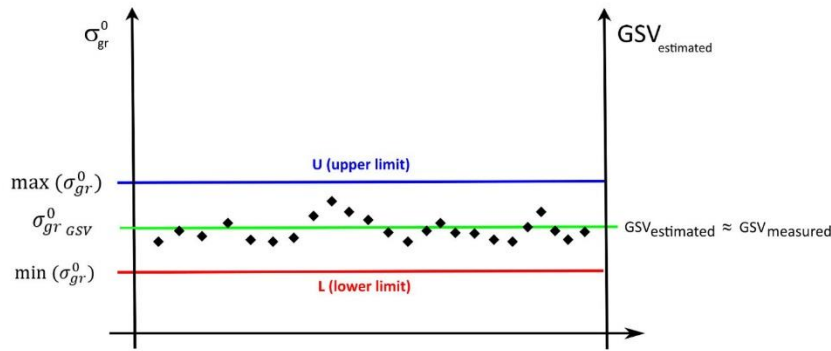


Figure 32: Temporal variation of σ_{gr}^0

1243
1244

1245 Using in-situ GSV data and soil moisture information, for each acquisition and estimated
 1246 σ_{gr}^0 , a comparison will be undertaken to investigate whether the estimated GSV value is close
 1247 to in-situ GSV and (using multivariate statistics) how σ_{gr}^0 , σ_{meas}^0 and soil moisture are
 1248 interrelated. As mentioned before, any difference between estimated GSV and in-situ GSV
 1249 at a specific time is expected to be related to soil moisture and its influence on σ_{gr}^0 . The goal
 1250 of the proposed modification to the algorithm is to analyse the connection between the
 1251 backscatter model parameter σ_{gr}^0 and σ_{meas}^0 , thus estimated GSV, at different soil moisture
 1252 conditions. Subsequently, a correction factor (Table 3) can then be introduced to σ_{gr}^0 in order
 1253 to compensate for over- or underestimation of GSV.

1254
1255

Table 3: Correction factor for σ_{gr}^0

Case:	Underestimation of GSV/AGB	Estimated GSV/AGB close the in-situ GSV/AGB	Overestimation of GSV/AGB
Correction factor:	>1	1	<1
σ_{gr}^0 :	$\min(\sigma_{gr}^0)$	$\sigma_{gr}^0_{GSV}$	$\max(\sigma_{gr}^0)$

1256

1257 4.2 Inundated forests - Temporal trend of ALOS-2 PALSAR-2 1258 backscatter

1259 Backscatter intensity from the L-band PALSAR-2 mosaics can have artificially higher returns
 1260 in forest areas (Figure 33) for several reasons including:

- 1261 • Partial inundation of the forest areas around rivers, due to double bounce
- 1262 scattering.
- 1263 • High soil/vegetation moisture, associated with increased dielectric constant

	Ref	CCI Biomass Product Validation and Algorithm Selection Report		
	Issue	Page	Date	
	1.0	65	10.02.2019	

- 1264
- 1265
- 1266
- 1267
- 1268
- 1269
- 1270
- 1271
- Recently harvested sites with logs still lying on site leading again to increased double bounce scattering.
 - Recent fire scars under wet conditions, leading to an enhanced contribution of the ground component and increased dielectric constant
 - Striping effects observed in ALOS PALSAR-2 mosaics in areas with continuous forest cover, such as the Amazon or Congo Basin, with this associated with the incidence angle dependence of backscatter (see ATBD)

1272 These effects lead to an erroneous estimation of AGB by the BIOMASAR algorithm on those

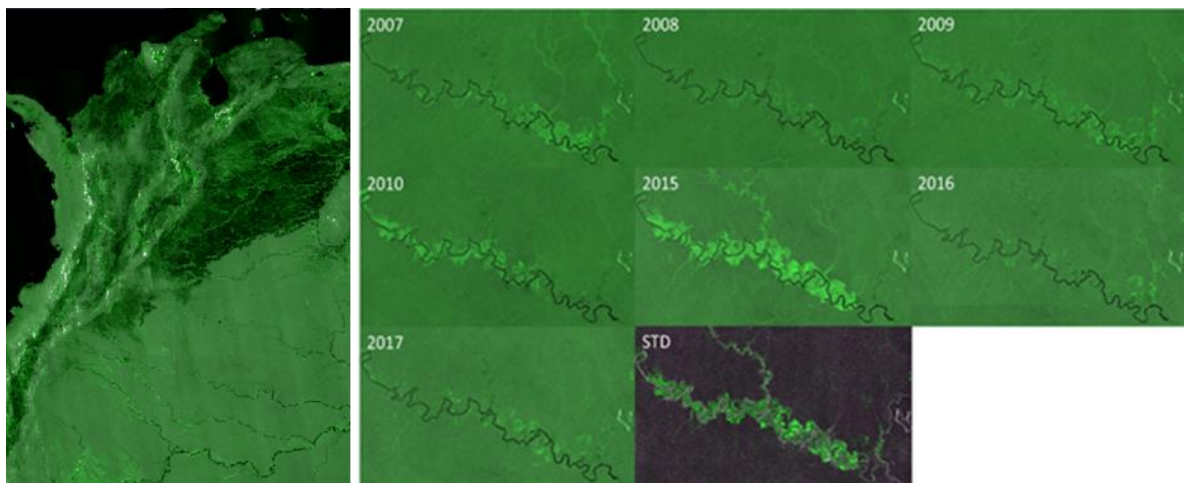
1273 areas. Whilst the integration of L-band HH have value in identifying where flooded areas

1274 occur, as demonstrated for the Amazon (e.g., Rosenqvist et al., 2002; Arneson et al., 2013),

1275 and the Congo (Mayaux et al., 2002; using a combination of ERS-2 SAR and JERS-2 SAR), it

1276 might not be so useful for the other cases.

1277



1278

1279 Figure 33 Left: PALSAR-2 composite showing striping effects. Right: Annual mosaics from PALSAR/PALSAR-2

1280 over a river area in the Colombian amazon showing the variability of backscatter due to inundation of riparian

1281 vegetation

1282 A solution is to make use of the temporal trend of the radar backscatter, or alternatively an

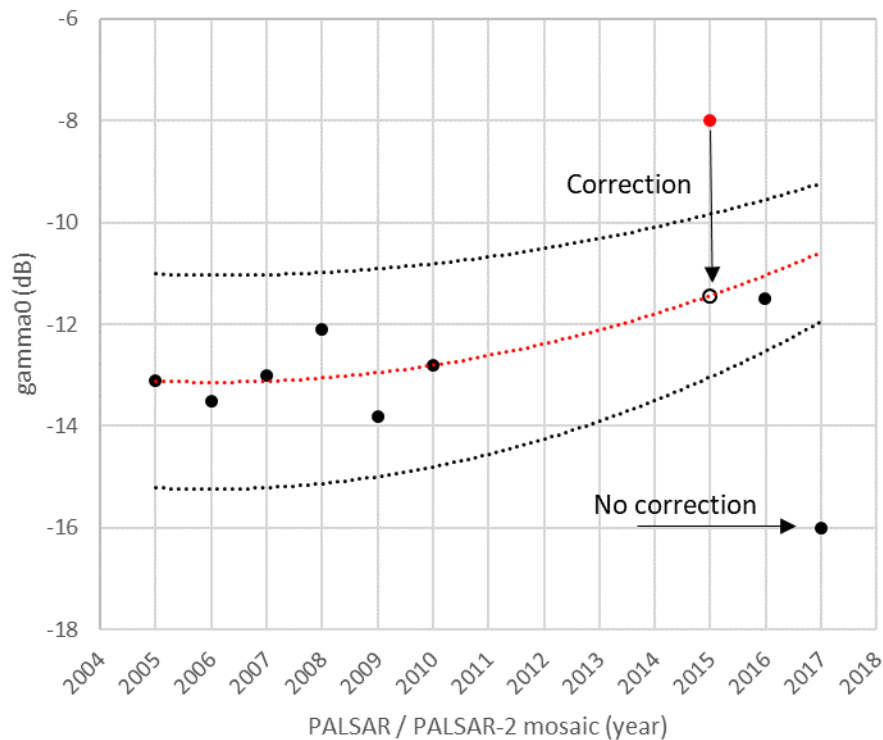
1283 outlier detection approach to identify those areas with artificially higher returns. Unaffected

1284 pixels from previous acquisitions or the expected return based on the calculated trend can

1285 then be used instead (see Figure 34).

	Ref	CCI Biomass Product Validation and Algorithm Selection Report	
	Issue	Page	Date
	1.0	66	10.02.2019





1286

1287 Figure 34. PALSAR-2 mosaic correction for a given pixel. The red dot corresponds to an artificially high
 1288 backscatter return. Red line is the temporal trend of the signal (excluding large outliers), and the black lines
 1289 correspond to twice the standard deviation. Note that the backscatter return observed in the year 2015 is
 1290 artificially high so it is corrected. However, the large drop in backscatter return observed in 2017 is not
 1291 corrected, because it is potentially related to a disturbance event

1292

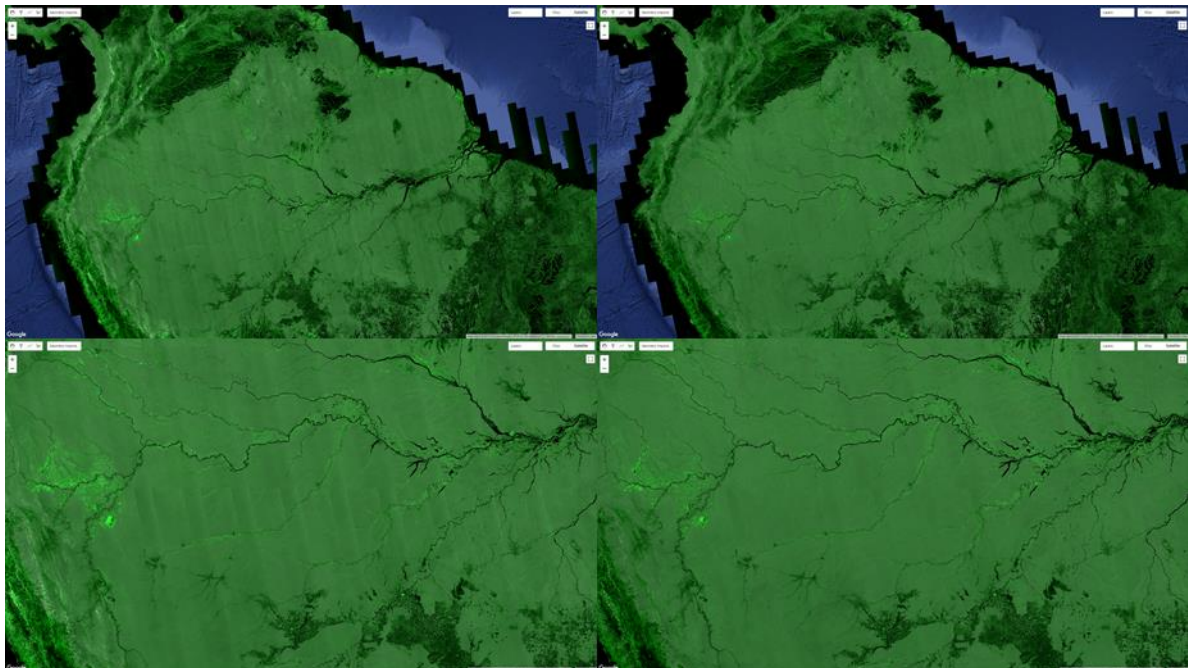
1293 An early and simplified implementation of the method (computationally low) uses temporal
 1294 statistics from PALSAR mosaics and simple linear regression for outlier detection, following
 1295 these steps:

- 1296 • Preparation of PALSAR mosaics 2007-2010 (removing invalid pixels based on QA layer,
 1297 calibration, multi-temporal filtering).
- 1298 • Preparation of PALSAR-2 mosaics 2015-2017 (removing invalid pixels based on QA
 1299 layer, calibration, multi-temporal filtering).
- 1300 • Generation of a master composite based on PALSAR median and standard deviation
 1301 pixel values for the period 2007-2010.
- 1302 • Histogram matching (normalization) of PALSAR-2 mosaics to the PALSAR master
 1303 composite (if needed).
- 1304 • Generation of three models with the form: $\gamma_t = f(\gamma_m)$, where γ_t is the gamma backscatter
 1305 intensity of the PALSAR-2 mosaic for a given year t (2015, 2016 or 2017), and γ_m is the

	Ref	CCI Biomass Product Validation and Algorithm Selection Report		
	Issue	Page	Date	
	1.0	67	10.02.2019	

- 1306 gamma backscatter intensity of the master PALSAR composite (2007-2010). Models
1307 were developed using an extensive random sample over forest areas only.
- 1308 • Pixels where the value of the PALSAR-2 mosaic (2015, 2016 or 2017) exceed the
1309 estimated value (using the γ_t models) beyond a given buffer (e.g. 2 x standard
1310 deviation) are identified as anomalous.
 - 1311 • The anomalous pixel values are changed to either values from previous mosaics, or to
1312 the values estimated by the corresponding γ_t models.
 - 1313 • Additional gap filing is performed using several passes of a 3x3 focal mean moving
1314 window

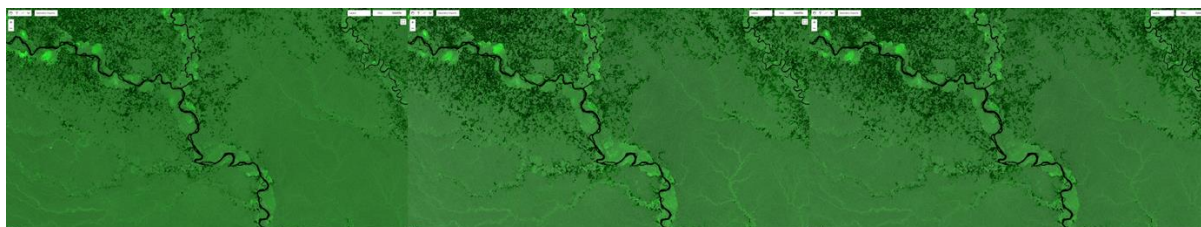
1315
1316 Examples of the simplified implementation are shown in Figure 35 and Figure 36



1317
1318 Figure 35 Example of the early implementation of the method over the Amazon region. Left: PALSAR-2 original
1319 mosaic. Right: PALSAR-2 corrected version (right)

1320

	Ref	CCI Biomass Product Validation and Algorithm Selection Report		
	Issue	Page	Date	
	1.0	68	10.02.2019	



1321

1322 Figure 36 Left: PALSAR mosaic 2007-10. Centre: PALSAR-2 original mosaic 2015-17. Right: PALSAR-2 corrected
 1323 mosaic 2015-17. Note that only artificially high backscatter returns (compared to PALSAR mosaic),
 1324 while deforestation events (backscatter drop) are not corrected

1325 4.3 Direct retrieval of AGB using the WCM.

1326 4.3.1 The WCM

1327 The current retrieval makes use of the WCM with gaps (Attema and Ulaby, 1978, Pulliainen
 1328 et al. 1994; Askne et al., 1997) and exploits the relationship with C-band (in BIOMASAR-C)
 1329 and L-band (in BIOMASAR-L) SAR backscatter. The model expresses the total forest
 1330 backscatter as the sum of a) direct scattering from the ground through gaps in the canopy,
 1331 b) ground scattering attenuated by the canopy and c) direct scattering from the vegetation:

$$1332 \quad \sigma_{for}^0 = (1 - \eta)\sigma_{gr}^0 + \eta\sigma_{gr}^0 T_{tree} + \eta\sigma_{veg}^0(1 - T_{tree}) \quad (5)$$

1333 Here η is the area-fill or tree cover factor, representing the fraction of the area covered by
 1334 vegetation, σ_{gr}^0 and σ_{veg}^0 , are the backscattering coefficients of the ground and vegetation
 1335 layer respectively. T_{tree} is the two-way tree transmissivity, which can be expressed as $e^{-\alpha h}$
 1336 where α is the two-way attenuation per meter through the tree canopy and h is the depth
 1337 of the attenuating layer. In GlobBiomass, the backscatter was described as a function of GSV
 1338 and V , as in Pulliainen et al. (1994):

$$1339 \quad \sigma_{for}^0 = \sigma_{gr}^0 e^{-\beta V} + \sigma_{veg}^0(1 - e^{-\beta V}) \quad (6)$$

1340 where β is an empirically defined coefficient expressed in ha m^{-3} . The link between η , α and
 1341 β is given by Santoro et al. (2002):

$$1342 \quad \eta = \frac{1 - e^{-\beta V}}{1 - e^{-\alpha h}} \quad (7)$$

1343

	Ref	CCI Biomass Product Validation and Algorithm Selection Report		
	Issue	Page	Date	
	1.0	69	10.02.2019	

1344 A limitation of the current implementation based on retrieval of GSV from the WCM is that
1345 errors are introduced in the subsequent conversion to AGB through use of wood density
1346 values and BCEF. Hence there is the option to retrieve AGB directly.

1347 4.3.2 Formulation of the WCM for Volume Retrieval

1348 To discuss the use of the WCM to retrieve Vegetation Stock Volume (VSV), a review of the
1349 Vegetation WCM, as formulated by Attema and Ulaby (1978) and later by Pulliainen et al.
1350 (1994), and Askne et al. (1997), is necessary.

1351
1352 The microwave dielectric constant of dry vegetative matter is much smaller (by an order of
1353 magnitude or more) than that of water and is usually composed of more than 99 % air by
1354 volume. Attema and Ulaby (1978) therefore proposed that the canopy could be modelled as
1355 a water cloud whose droplets were held in place by the vegetation matter. A model was
1356 therefore developed that assumed that the canopy “cloud” contains identical water droplets
1357 that are distributed randomly within the canopy. By integrating the scattering and
1358 attenuation cross-section contribution of N droplets per unit volume over the signal path
1359 length through the canopy, an expression was derived for the backscattering coefficient as a
1360 function of three target parameters: a) the volumetric water content (W ; kg m^{-3}) of the
1361 vegetation, b) the volumetric moisture content of the soil under the canopy and c) plant
1362 height. The model was applied to agricultural crops, at several angles of incidence (0° – 70°)
1363 and frequencies (8–18 GHz) for HH and VV polarizations. The formulation was not intended
1364 for application to the cross-polarisation (HV or VH) as multiple scattering is neglected.

1365
1366 Where individual scatterers are located far from each other (in terms of wavelength; 8-18
1367 Ghz in the case of Attema and Ulaby (1978)), radiative transfer theory is applicable such that
1368 the reflectivity and attenuation factors are a linear function of the number density of water
1369 particles. The reflectivity factor (ρ ; or radar cross section per unit volume, $\text{m}^2 \text{m}^{-3}$) and the
1370 power attenuation coefficient per unit length (α) can then be expressed as:

$$1371 \quad \rho = N\sigma \text{ [m}^{-1}\text{]}$$

$$1372 \quad \alpha = NQ \text{ [m}^{-1}\text{]}$$

1373
1374
1375 where N is the number of water particles per unit volume and σ and Q are the radar cross
1376 section and the total attenuation cross section for one single particle respectively.

1377

	Ref	CCI Biomass Product Validation and Algorithm Selection Report		
	Issue	Page	Date	
	1.0	70	10.02.2019	

1378 The average backscatter power from the vegetation resulting from an incident radar beam
1379 is:
1380

$$1381 \quad \sigma_{veg}^0 = \left(\frac{\sigma}{2Q}\right) \left(1 - e^{\frac{-2NQ.h}{\cos\theta}}\right) \cos\theta \quad (8)$$

1382
1383 where θ is the incidence angle and h (m) represents the height of the vegetation layer
1384 involved in the interaction. Since all water particles are assumed identical in shape and size,
1385 σ and Q are constants at a given frequency, $\sigma/2Q$ can be replaced by a parameter C. As N is
1386 proportional to the volumetric water content W_v (kg m^{-3}), $2NQ$ is replaced by DW_v , where D
1387 is a parameter.
1388

$$1389 \quad \sigma_{veg}^0 = C \left(1 - e^{\frac{-DW.h}{\cos\theta}}\right) \cos\theta \quad (9)$$

1390
1391 In this formulation, the vegetation physical variable is:

$$1392 \quad W = W_v \times h \quad (10)$$

1393
1394
1395 which represents the water content per unit area (kg m^{-2}) of the vegetation layer involved in
1396 the interaction. For agricultural crops, the wave penetration depth usually exceeds the
1397 vegetation canopy height and so the vegetation variable is the water content per unit area
1398 of the whole canopy. As the water content per unit area is not a vegetation variable of
1399 interest in many applications, studies have been conducted to relate the variable which can
1400 be retrieved from radar data (i.e., the water content per unit area of the interacting layer) to
1401 the main variables of interest (i.e., vegetation biomass and indirectly LAI) to be used in
1402 estimation or modelling of the crop productivity. By adding a term for the attenuated ground
1403 backscatter, the model by Attema and Ulaby (1978) has been used widely for the retrieval of
1404 agricultural crop biomass and LAI, mostly using X- and C-band SAR data.
1405

1406 The model was first applied to pine forests in Finland by Pulliainen et al. (1994) but instead
1407 of expressing the attenuation in terms of biomass (or LAI), the objective was to retrieve stem
1408 (or timber) volume as this parameter was of most relevance to forest management and
1409 inventory and, in Finland, field measurements of stem volume were widely available for
1410 validation. Hence, for a single tree, the stem volume was related to other variables through
1411 the expression of the fresh biomass of the stem such that:

1412

	Ref	CCI Biomass Product Validation and Algorithm Selection Report		
	Issue	Page	Date	
	1.0	71	10.02.2019	

1413
$$M_B = c \times \rho_d \times V = M_d + W \quad (11)$$

1414

1415 where the above-ground fresh biomass (M_B , kg) was considered to be a product of stem
1416 volume (V , m³), wood density (km m⁻³, with a value of 0.4 assigned for pine) and c (a
1417 parameter, similar to the BECF, relating the measured stem volume to AGB, with the range
1418 1.4-2.1 dependent upon on the tree age), as well as the sum of the above-ground dry biomass
1419 (M_d ; kg) and the above-ground water content (W , kg).

1420

1421 In order to understand the assumptions underlying the use of volume in Pulliainen et al.
1422 (1994), the stem volume for a unit area (at the pixel scale) comprising n trees can be
1423 expressed as a function of water content and dry biomass (in the attenuating layer):

1424
$$\sum_{i=0}^n \text{Stem volume} = \sum_{i=0}^n \left[\frac{\text{dry biomass} + \text{water content}}{\text{wood density} \times \text{BECF}} \right] \quad (12)$$

1425 The sum of the dry biomass and water is the wet or fresh biomass and, as with wood density
1426 and BCEF, varies as a function of tree species and age. Hence, if we assume that:

1427

- 1428 1) The n trees in the pixel are of the same species type and BCEF.
- 1429 2) In the attenuating layer, the water content (kg m⁻²) is proportional to dry biomass (kg
1430 m⁻²),
- 1431 3) A strong correlation exists between the parameters of the attenuation layer (the
1432 water content and dry biomass) and that of the whole forest layer
- 1433 4) The stem volume and the wet biomass are strongly correlated,

1434

1435 Then the water content can be considered to be proportional to stem volume, which then
1436 means that the attenuation can be formulated as a function of stem volume.

1437

1438 Some forests (e.g., in the boreal zone and in some wooded savannas) are dominated by one
1439 or a few species with similar characteristics and hence these assumptions are valid.
1440 However, many forests are of mixed composition, particularly if the density is high. In these
1441 cases, it is difficult to convert volume into AGB as a wide range of wood density and BCEF
1442 apply and are often not available.

1443

1444 Askne et al. (1997) applied the WCM to forest canopy with gaps, which considers backscatter
1445 from the forest (σ_{for}^0), the ground floor (σ_{gr}^0) and the vegetation layer (σ_{veg}^0 ; Equation 5).
1446 Each can be measured separately (e.g., using a ground-based or airborne scatterometer) and
1447 the two-way attenuation (T_{tree}) retrieved. From T_{tree} , vegetation parameters of interest can

	Ref	CCI Biomass Product Validation and Algorithm Selection Report		
	Issue	Page	Date	
	1.0	72	10.02.2019	

1448 be derived. Pulliainen et al. (1999) and Santoro et al. (2002) introduced the empirical
 1449 coefficient β to model the two-way forest transmissivity, where V represents the stem
 1450 volume. The coefficient β depends on forest structure and the dielectric properties of the
 1451 canopy.

1452
 1453 The assumptions used in the formulation of the WCM could apply to forests of the same
 1454 structure and dielectric constant. However, translating this for global application can be
 1455 problematic and difficult to validate, particularly as the definition of GSV varies between and
 1456 often within countries. As examples, some consider GSV to include the branches exceeding
 1457 a certain diameter as well as the stems or estimate this only for tree species with commercial
 1458 value (e.g., as in many temperate and boreal regions). **Hence, a more direct retrieval of AGB**
 1459 **rather than GSV is beneficial** as the additional errors introduced in the conversion of GSV to
 1460 AGB (because of variable use of wood density and BCEF) is avoided.

1461 4.3.3 Reformulation of the WCM for AGB retrieval

1462 To reformulate the WCM so that AGB is retrieved through consideration of forest
 1463 transmissivity will require the use of unknown parameters (e.g., C and D in Equation 5, plus
 1464 another that accounts for scattering from the ground surface outside of the canopy area).
 1465 These parameters need to be fitted using available *in situ* data from selected inventories and
 1466 LiDAR-derived AGB maps. Using reference datasets available in this project, including data
 1467 from the *in situ* database by the Laboratoire Evolution et Diversite Biologique (EDB), the first
 1468 step is to establish how consistent the parameter estimates are, at each reference site used
 1469 in the previous analysis (mainly Lidar maps), at eco-regions, biomes and globally. Many
 1470 datasets are not distributed globally but there is increasing effort to collate and collect new
 1471 data and, with this in mind and the expectation of newer and more diverse satellite datasets
 1472 (e.g., NISAR), it is better to start the formulation of a model in preparation. This then
 1473 facilitates upgrading the AGB map products when more reference data become available.
 1474 The development of such capacity is particularly needed to support AGB retrieval in the dry
 1475 tropics of lower biomass ($< 100 \text{ Mg ha}^{-1}$) and regions of intermediate biomass ($100\text{-}200 \text{ Mg}$
 1476 ha^{-1}). Upon this first assessment, the sets of parameters to be used will be proposed, for
 1477 different 'regions' where the same parameters apply.

1478 4.4 Summary

1479 Options for refining the GlobBiomass algorithm are as follows:

	Ref	CCI Biomass Product Validation and Algorithm Selection Report		
	Issue	Page	Date	
	1.0	73	10.02.2019	

- 1480
- 1481
- 1482
- 1483
- 1484
- 1485
- 1486
- 1487
- 1488
- 1489
- 1490
- 1491
- 1492
- 1493
- 1494
- Reformulating the WCM to relate the radar backscatter to AGB
 - Parameterising the WCM with *in situ* data and making greater use of available *in situ* and LiDAR-derived AGB data to derive fitting parameters.
 - Using remotely sensed soil moisture information to inform the estimation of σ_{gr}^0
 - Incorporating the temporal trend of ALOS PALSAR backscatter in inundated forests
 - Applying corrections for terrain effects through pre-processing of the original Japanese L-band SAR data.
 - Generating a global classification of land covers according to the FAO LCCS taxonomy to replace or complement the Global Ecological Zones (GEZ), to improve the parameterisation of the WCM (e.g., transmissivity, values for σ_{diff}^0 , maximum GSV).

1495 5 Complementary Approaches

1496 Complementary approaches have also been considered, where the BIOMASAR algorithm
 1497 results in over or underestimation of AGB, namely those that indicate greater sensitivity to
 1498 AGB within the upper ranges (e.g., in the wet tropics) or where underestimation is ubiquitous
 1499 (e.g., mangroves):

- 1500
- 1501 a) Decreasing trend of L-band PALSAR backscatter with AGB (Mermoz et al., 2015)
- 1502 b) Use of the Vegetation Optical Depth (VOD from the SMOS sensor.
- 1503 c) Combinations of structural measures (primarily height and cover) to explore and
 1504 exploit their sensitivity to the full range of AGB.
- 1505 d) Use of CHMs, including that derived from the Tandem-X for retrieving the AGB of
 1506 mangroves.

1507

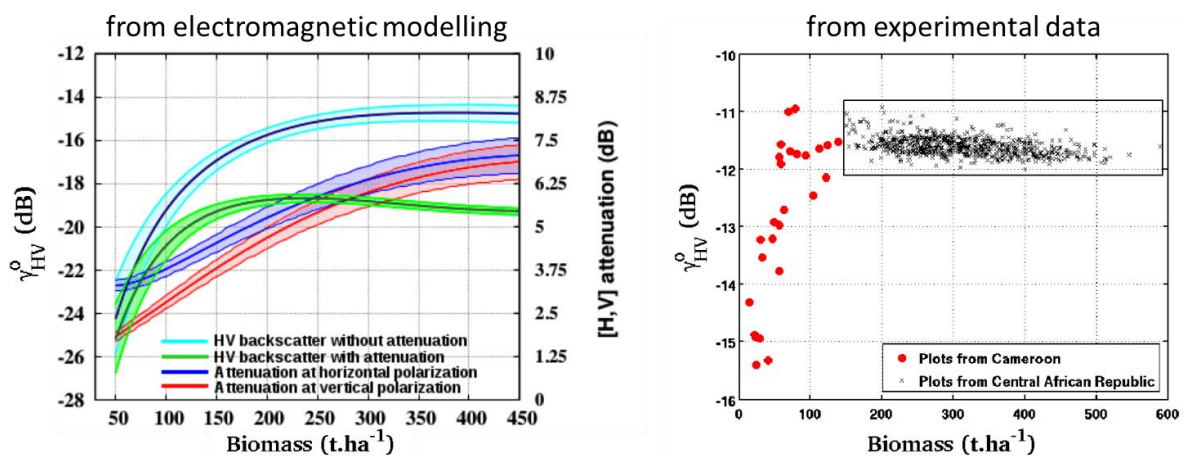
1508 The following provides an overview of these approaches.

1509 5.1 Backscatter decreasing trend

1510 Within many forests, and particularly in the wet tropics, different levels of AGB were unable
 1511 to be discerned using the BIOMASAR algorithm, largely because of saturation of the L-band

	Ref	CCI Biomass Product Validation and Algorithm Selection Report		
	Issue	Page	Date	
	1.0	74	10.02.2019	

1512 HV backscatter above relatively low levels. However, Mermoz et al. (2015) established a
1513 decreasing trend in the denser forests of Central African Republic and the DRC. The
1514 decreasing trend has also been observed over mangrove forests (Lucas et al., 2007) and is
1515 interpreted as a signal attenuation from the forest canopy as the canopy becomes denser
1516 (leading to higher volumic fraction) as AGB increases. This finding is illustrated in Figure 37,
1517 using electromagnetic results from the MIPERS model (Villard et al., 2009) and experimental
1518 data in Central African Republic based on the ALOS PALSAR mosaic 2010 and *in situ* data.



1519 Figure 37: (Left) Left axis: Simulated HV backscatters versus AGB, plotted in green (with attenuation from the
1520 vegetation) and cyan (without attenuation from the vegetation). Right axis: Simulated attenuations at
1521 horizontal (blue) and vertical (red) polarizations, accounting for the signal loss (in dB) due to the wave
1522 propagation forth and back. The uncertainties related to wood density variations (3.5% around mean value of
1523 $0.58 \text{ g} \cdot \text{cm}^{-3}$) are represented by the filled colour domains surrounding the curves. (Right): SAR backscatter at
1524 HV polarization versus *in situ* above ground biomass (AGB) after the selection process. Twenty-one savanna
1525 and 5 forest 1-ha field plots, acquired from the REDDAF project (Haeusler et al., 2012), in 2011 in the Adamawa
1526 Province, Cameroon and in 2013 in the Central Province, Cameroon, were added.
1527

1528 The sensitivity of backscatter to AGB is smaller at higher levels of AGB. In order to
1529 experimentally observe the decreasing trend of the backscatter, given such a small
1530 sensitivity, the analyses require a reduction of the perturbing factors effects, which are
1531 related to the forest structure and environment and to the uncertainties in the radar data
1532 and *in situ* AGB data, by reducing the spatial resolution to 500m.
1533

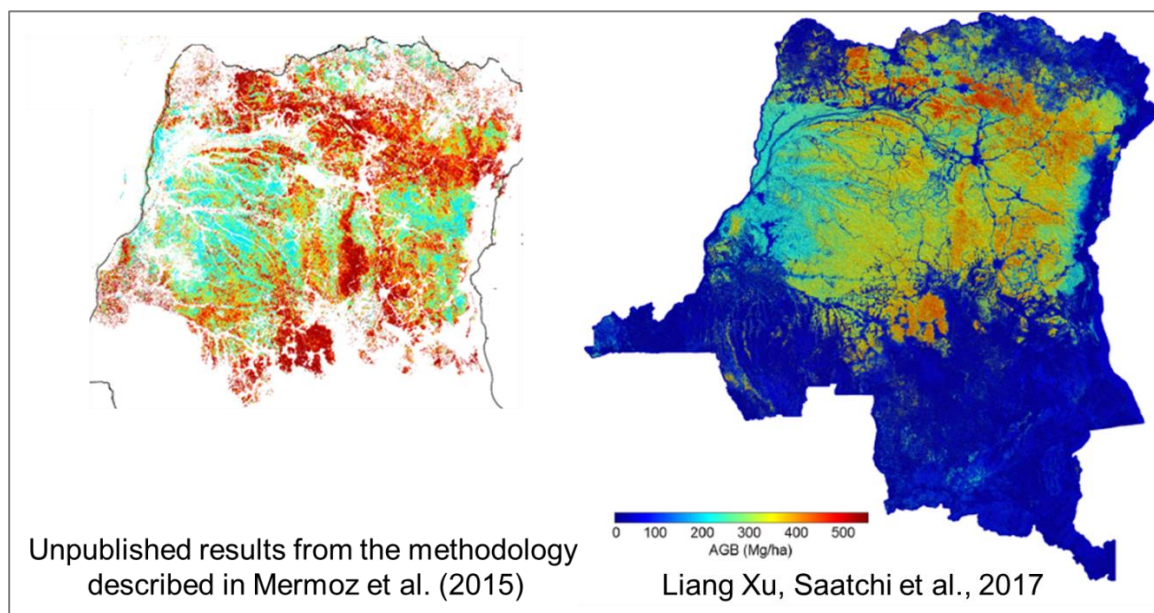
1534 The AGB of dense forests was estimated in DRC using the decreasing trend described in
1535 Mermoz et al. (2015). The CCI land cover 2010 was used to discriminate dense forest from
1536 other land cover classes. AGB estimates at 500m resolution are shown in Figure 38 (left) and
1537 compared to the LiDAR-derived AGB map of Xu et al. (2017) at 100m resolution (right) (as
1538

	Ref	CCI Biomass Product Validation and Algorithm Selection Report		
	Issue	Page	Date	
	1.0	75	10.02.2019	

1539 previously noted the LiDAR-derived AGB map was calibrated using a total of 216 LiDAR
1540 transects evenly distributed in dense forests, providing more than 432,000 ha of forest
1541 samples. The figure shows that similar patterns are clearly visible in the two maps. This result
1542 is to be compared with the GlobBiomass map of DRC (in Figure 11), which shows no visible
1543 spatial patterns. A comparison study between ALOS PALSAR mosaic data and the LiDAR-
1544 derived AGB map confirmed the decreasing trend over the DRC dense forests. However,
1545 further improvements are needed to apply the methods in high AGB forest in the tropics:
1546

- 1547 • In addition to volumic fraction, the decreasing trend is probably related to other
1548 forest structural characteristics. Joshi et al. (2017) showed using *in situ* data in
1549 Spain and Denmark that a decrease in stem numbers with increasing AGB (e.g.
1550 taller, larger and sparser trees) would contribute to the decreasing trend. A
1551 similar study using an extensive reference dataset, available in the project, should
1552 be conducted in the tropics to better understand and generalize this decreasing
1553 trend,
- 1554 • Ancillary datasets at the global scale are needed to know where the decreasing
1555 trend is valid. The structural classification developed by Scarth et al. (2019) and
1556 extended at the global scale by Aberystwyth University could contribute to this
1557 task.

	Ref	CCI Biomass Product Validation and Algorithm Selection Report		
	Issue	Page	Date	
	1.0	76	10.02.2019	



1558

1559 Figure 38 (left) AGB estimates at 500m resolution, compared to (right) the LiDAR-derived AGB map of Xu et al.
 1560 (2017) at 100m resolution

1561 CESBIO and EDB (Jerôme Chave) teams are in contact with Sassan Saatchi's team, which is
 1562 keen to share the LiDAR dataset used in Xu et al. (2017). The LiDAR data over Brazil by Micheal
 1563 Keller with plots set up and Lidar coverages within the framework of the Sustainable
 1564 Landscapes Brazil project. Those unique datasets, providing information on forest structure,
 1565 are well adapted for a better understanding of the relationships between forest structure
 1566 and SAR backscatter. A part of this dataset would also contribute to validating the AGB
 1567 estimation method based on the decreasing trend.

1568

1569 When fully validated across a range of dense forests, there is potential to interface the
 1570 algorithm with GlobBiomass although, because the sensitivity of the L-band backscatter to
 1571 AGB is weak, there is a need to degrade the spatial resolution (e.g. to 500 m).

1572

1573 5.2 Use of L-Band VOD

1574 The use of SMOS VOD (downscaled to 1km resolution) to overcome the saturation of SAR in
 1575 very dense forest and high ranges of AGB, can improve AGB retrieval mainly in dense forest
 1576 but can be applied to all forest types for a global approach.

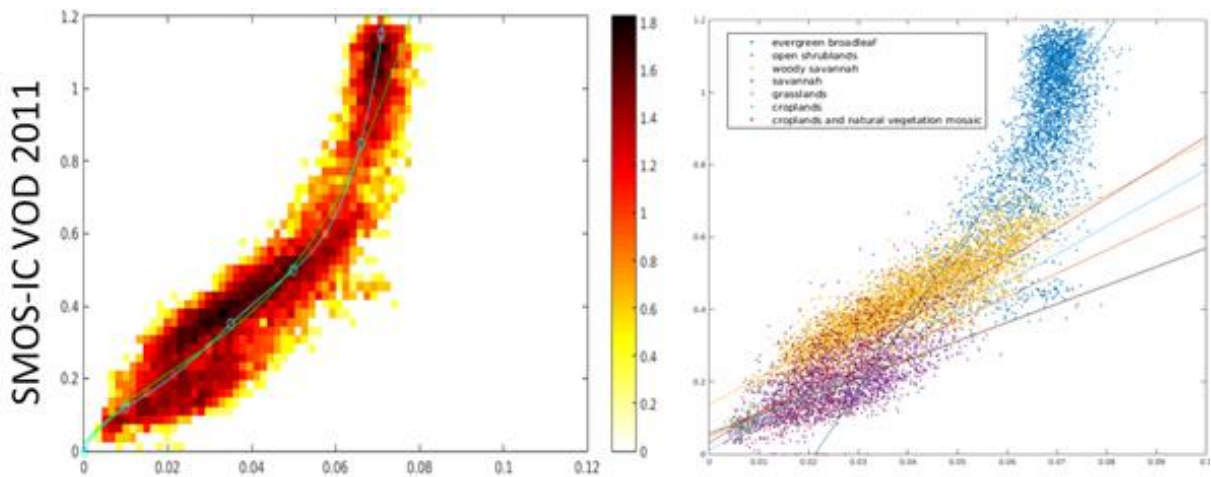
1577

	Ref	CCI Biomass Product Validation and Algorithm Selection Report		
	Issue	Page	Date	
	1.0	77	10.02.2019	

1578 The VOD, as measured at L-Band by the SMOS satellite, is linked to vegetation water content
1579 and to vegetation structure both of which relate to AGB and yearly maps have been
1580 generated for a 20 year period using these data from different satellites (Liu et al., 2015).
1581 Nevertheless, the relatively coarse spatial resolution (40 km) is a limiting factor for retrieval
1582 but there is potential to downscale the spatial resolution of SMOS L-VOD to generate a target
1583 AGB product at 1 km. The VOD also varies seasonally and is dependent on forest structure
1584 and moisture (dielectric properties), which can introduce errors in its use for AGB retrieval.
1585 Hence, despite the very high temporal frequency of the data, only one yearly VOD/AGB map
1586 is proposed.

1587
1588

1589 Launched by ESA in 2009, the SMOS satellite (Kerr et al., 2010) performs passive microwave
1590 observations at L-Band (1.4 GHz, 21 cm). Its full-polarization and multi-angular capabilities
1591 allow the simultaneous retrieval of soil moisture content and VOD. At the same frequency,
1592 L-band, the passive measurement has one-way attenuation, whereas the SAR measurements
1593 have two-way attenuation satellites, resulting in little saturation of SMOS-IC VOD for high
1594 AGB values in dense forests (Rodriguez-Fernandez et al., 2018) as compared to the ALOS-
1595 PALSAR backscatter (Figure 39).
1596



ALOS mosaic HV backscatter 2010

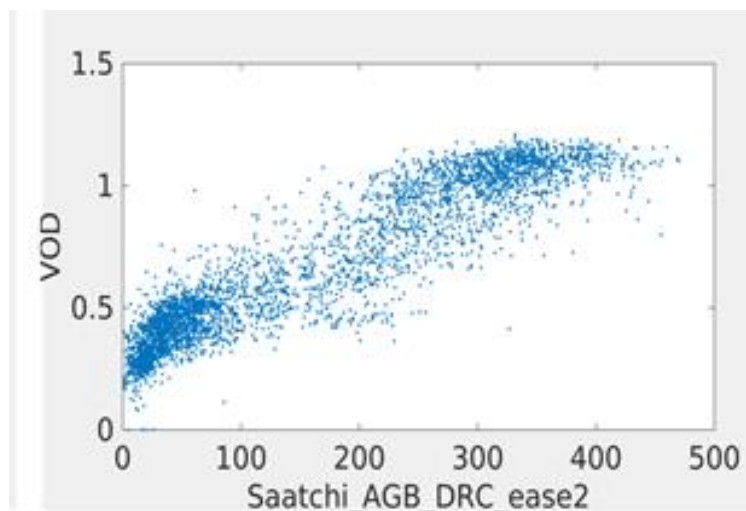
1597

1598 Figure 39: SMOS L-VOD plotted with respect to ALOS HV backscatter at low resolution over the Congo basin
1599 (Left) and for each biome/ecosystem (Right). Various regression models (log, exp and linear) were tested for
1600 relating VOD to SAR backscatter

1601

	Ref	CCI Biomass Product Validation and Algorithm Selection Report		
	Issue	Page	Date	
	1.0	78	10.02.2019	

1602 A linear relationship (similar slope) between VOD and the backscatter for low biomass
1603 savanna (violet) and woody savanna (orange) was evident. Where the backscatter for
1604 evergreen broad-leaved forest (blue) saturates (at 0.07; about -11.5 dB), VOD increases from
1605 0.6 to 1.2 for the full range of AGB. This sensitivity can be exploited for AGB estimation,
1606 particularly for dense forests. For example, a close correspondence between VOD and AGB
1607 (derived based on LiDAR data; Xu et al., 2017) was observed for the Congo Basin (Figure 40).



1608
1609 Figure 40: SMOS VOD as a function of AGB in the DRC, as derived from the DRC map by Xu et al. (2017).
1610

1611 In addition, the evolution of the moisture content within vegetation can be studied using the
1612 SMOS because of the high revisit frequency (three days) since 2009. However, downscaling
1613 the spatial resolution (e.g., to 1 km) is essential to maximize use of the VOD for retrieving the
1614 AGB of dense forests. For downscaling, other global datasets with sensitivity to AGB across
1615 the full range are needed. As a first test, the 25 m ALOS PALSAR mosaic data from 2010 for
1616 the Congo Basin were considered, despite lack of sensitivity to AGB at high AGB. The L-VOD
1617 data used in this study were computed using the SMOS-IC (INRA-CESBIO) algorithm
1618 (Rodriguez-Fernandez et al. 2018) in a 25 km EASE-Grid 2.0. The data were averaged over
1619 the whole year 2011 to remove seasonal variations in the vegetation water content. The
1620 ALOS mosaics at HV polarization averaged to 1 km were used to disaggregate the SMOS L-
1621 VOD using the following equation, which was originally developed to disaggregate SMOS soil
1622 moisture (Oiha et al. 2018).

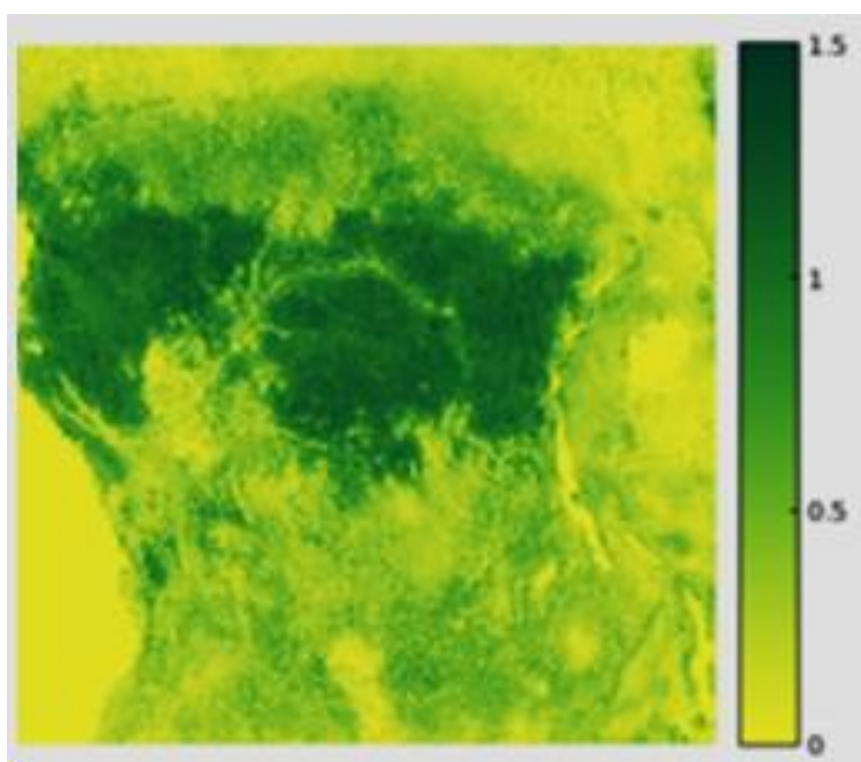
1623
1624

$$1625 \quad VOD_{HR} = VOD_{LR} \left(\frac{\partial VOD_{LR}}{\partial \gamma_{LR}} \right) \cdot (\gamma_{HR} - \gamma_{LR}) \quad (13)$$

	Ref	CCI Biomass Product Validation and Algorithm Selection Report		
	Issue	Page	Date	
	1.0	79	10.02.2019	

1626
1627
1628
1629
1630
1631
1632

VOD_{HR} and VOD_{LR} represent the SMOS L-VOD in the final 1 km resolution and in the original 25 km resolution grids respectively, γ_{HR} is the ALOS backscatter averaged at 1 km and γ_{LR} is the ALOS backscatter averaged in the 25 km EASE-Grid 2.0 of SMOS products. The derivative of a third-order polynomial regression describing the VOD-L-band backscatter relationship was developed to compute the disaggregated VOD_{HR} (Figure 41).



1633
1634

Figure 41: Disaggregated SMOS L-VOD at 1 km resolution over the Congo Basin

1635 As expected from the use of ALOS L-band data for downscaling, improvement was observed
1636 for the range of AGB < 150 Mg ha⁻¹.

1637
1638
1639
1640

Validation has been undertaken for the DRC map (Saatchi et al 2017) but this needs to be extended to encompass different regions for a global assessment. Research is being undertaken to:

1641
1642
1643
1644
1645

- Compare the VOD map with datasets in different regions, and compare the biomass from SMOS with LiDAR and field data (start with Geocarbon datasets)
- Define the auxiliary data for downscaling (other than ALOS L-band)
- Determine the optimal spatial resolution (1 km - 5 km?) for global AGB mapping based on the trade-off between spatial resolution and accuracy

	Ref	CCI Biomass Product Validation and Algorithm Selection Report		
	Issue	Page	Date	
	1.0	80	10.02.2019	

- 1646
- 1647
- 1648
- 1649
- 1650
- 1651
- Interface with the GlobBiomass algorithm at high resolution (100 m) and VOD at low resolution (1 km; where GlobBlomass is currently limited).
 - Synergy between different AGB indicators: BIOMASAR-C, BIOMASAR-L, VOD and Structure need to be investigated to decide the best solution for the different biomes and forest types.

1652 Expected improvements from this method include:

- 1653
- 1654
- 1655
- 1656
- 1657
- 1658
- Overcoming the SAR saturation in dense forests, but application as well to all forest types.
 - Possibility to provide maps of AGB for over 20 years (SMOS and other passive microwave satellites).
 - Possibility of using SMOS VOD datasets for annual biomass change at a global scale.

1659 To pursue this work in the CCI Biomass frame we need to involve the CESBIO SMOS team in

1660 the project.

1661 **5.3 Use of Structural information as a New Global Indicator**

1662 As ICESAT-derived height and cover inputs to the MLA provided a good representation of

1663 AGB across Australia, the use of these two variables at was also considered at a global level.

1664 As ICESAT footprints are relatively sparse across the forested landscape, reference was made

1665 instead to the global tree canopy density layer of Hansen et al. (2013) and canopy height

1666 estimate of Simard et al. (2013), with both resampled to 100 m spatial resolution. A cross

1667 tabulation of these data was then undertaken to produce a globally applicable taxonomy

1668 (Figure 42) and classification (Figure 43) of forest structure based on 5 m height and 10 %

1669 canopy cover intervals. Of note was that variability in the structure (height and cover) within

1670 the higher AGB of the wet tropics

1671

	Ref	CCI Biomass Product Validation and Algorithm Selection Report		
	Issue	Page	Date	
	1.0	81	10.02.2019	

A0		A1	A2	A3	A4	A5	A6	A7	A8	A9
V. Sparse (< 10 %)		>10-20	>20-30	>30-40	>40-50	>50-60	>60-70	>70-80	>80-90	>90-100
Canopy Height (m)	2-5	1	2	3	4	5	6	7	8	9
	>5-10	10	11	12	13	14	15	16	17	18
	>10-15	20	21	22	23	24	25	26	27	28
	>15-20	30	31	32	33	34	35	36	37	38
	>20-25	40	41	42	43	44	45	46	47	48
	>25-30	50	51	52	53	54	55	56	57	58
	>30-35	60	61	62	63	64	65	66	67	68
	>35-40	70	71	72	73	74	75	76	77	78
	>40-45	80	81	82	83	84	85	86	87	88
	>45-50	90	91	92	93	94	95	96	97	98
>50	100	101	102	103	104	105	106	107	108	

Figure 42: Colour scheme and legend for the classification based on height and cover categories placed at intervals of 2-5 m and 5 m thereafter and >10 % and 10 % thereafter.

1672

1673 As an example, in the Democratic Republic of the Congo (DRC), classes 48, 58, 68, 78 were
 1674 associated with forests of higher AGB, as determined through comparison with the map of
 1675 Saatchi et al. (2011; Figure 44)

1676

1677

1678

1679

1680

1681

1682

1683

1684

1685

1686

1687

1688

1689

1690

1691

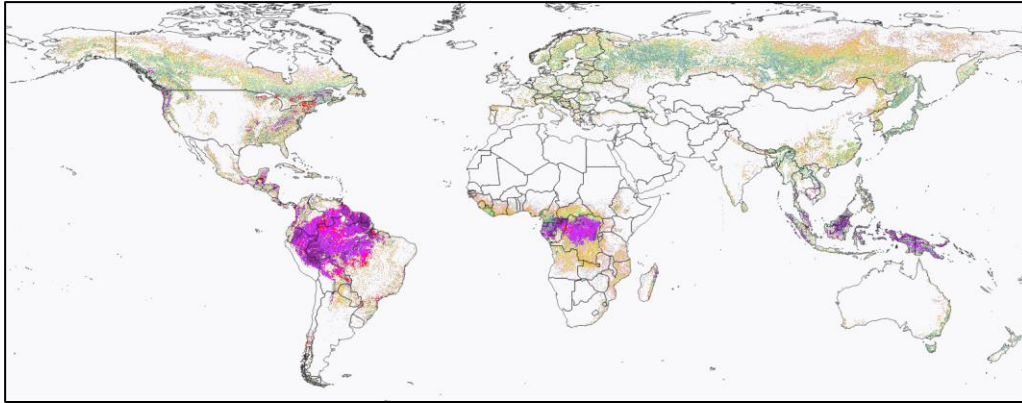
1692

1693

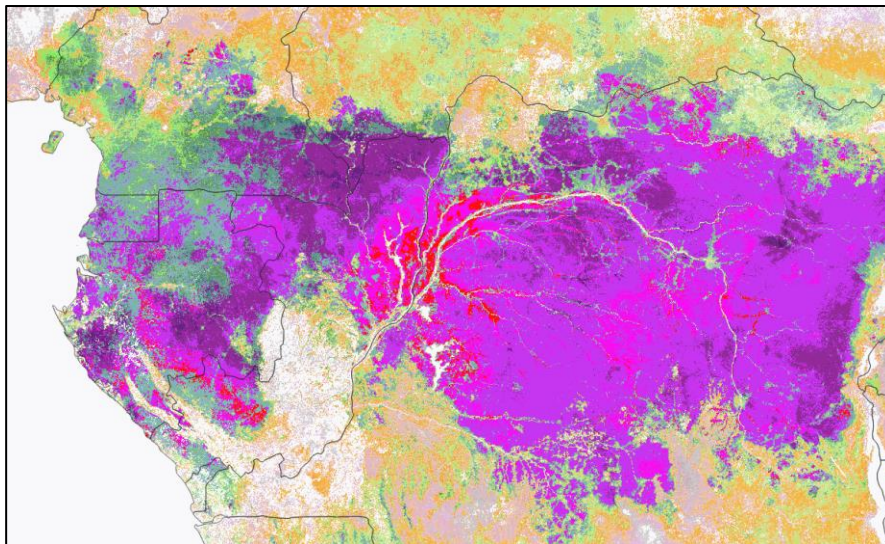
1694

	Ref	CCI Biomass Product Validation and Algorithm Selection Report		
	Issue	Page	Date	
	1.0	82	10.02.2019	

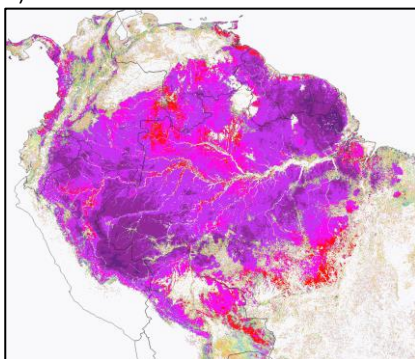
a)



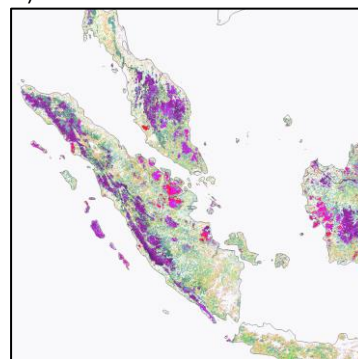
a)



c)

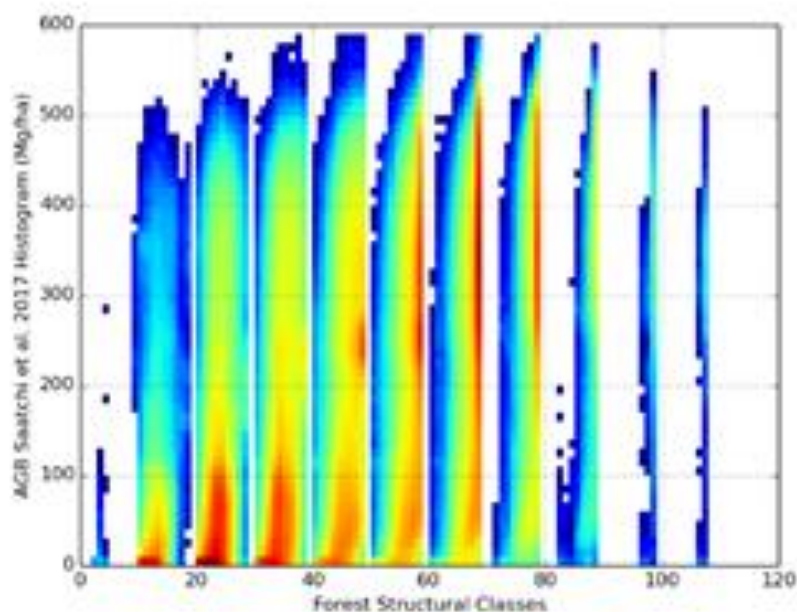


d)



1695 Figure 43: Structural classification based on cross tabulation of the Hansen et al. (2013) canopy cover and
 1696 Simard et al. (2013) canopy height layers for a) the World, b) central Africa, c) Amazonia and d) Peninsular
 1697 Malaysia and Indonesia. The legend is shown in Figure 41.

	Ref	CCI Biomass Product Validation and Algorithm Selection Report		
	Issue	Page	Date	
	1.0	83	10.02.2019	



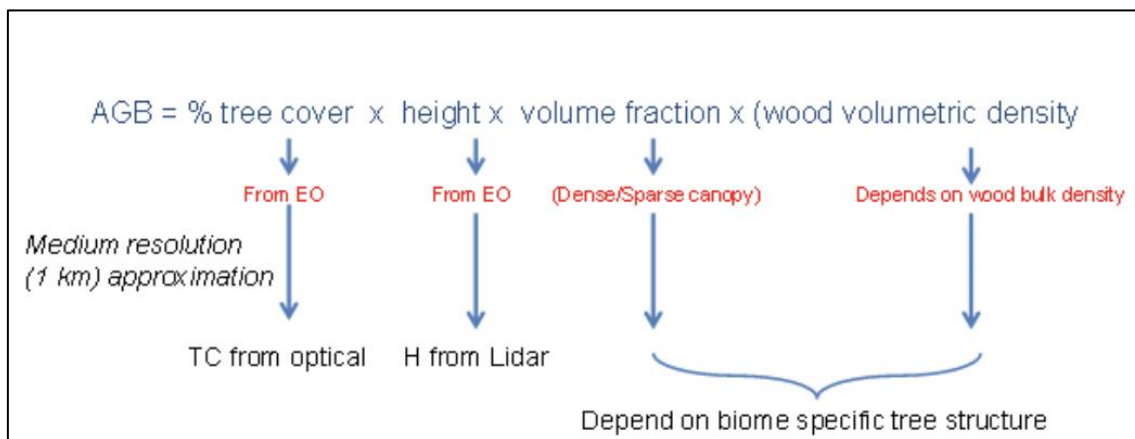
1698
1699 Figure 44: The association of forest structural classes in the Democratic Republic of Congo (DRC) with AGB
1700 (estimated by Xu et al., (2017). Dense forests are associated with classes 58, 68, 78 (TC>90%, H>25-30 m;
1701 TC>90%, H>30-35 m, TC>90%, H>35-40 m), with these also supporting a higher AGB.

1702
1703 To generate a quantitative assessment, AGB was expressed as a function of tree cover,
1704 height, volume fraction and wood volumetric density (Figure 45) where:

- 1705
- 1706 • $TC \times H$ represent the scattering volume in the pixel.
 - 1707 • The volume fraction represents the scatterers distribution inside the scattering
 - 1708 volume.
 - 1709 • The wood volumetric density expresses the relation between AGB and the volume
 - 1710 fraction of the scatters.

1711
1712

	Ref	CCI Biomass Product Validation and Algorithm Selection Report		
	Issue	Page	Date	
	1.0	84	10.02.2019	



1713

1714 Figure 45: An approach to establishing the relationship between AGB to tree cover (%), canopy height (m),
1715 volume fraction and wood volumetric density.

1716

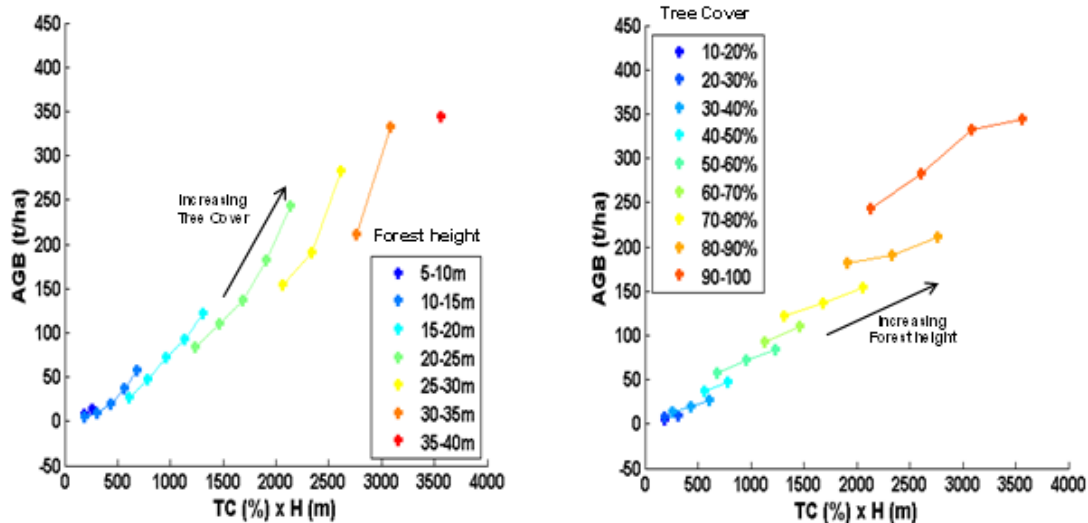
1717 For monospecific forest, both the volume fraction and the wood volumetric density can be
1718 estimated with greater confidence but, for forests comprised of different species and age
1719 classes, the conversion to AGB is more problematic and limits global application. However,
1720 when the spatial resolution was degraded to 1 km (as when using the canopy height layer
1721 from Simard et al., 2011), the volume fraction and wood volumetric density become
1722 indicators of tree structure specific to the biome or forest type. In this condition, $AGB = f(TC \times H)$
1723 for each structural class. The sensitivity of AGB to tree cover and height is indicated in
1724 Figure 46 (left), where the data points with the greatest AGB correspond to classes 48, 58,
1725 68 and 78 in the structural classification (i.e., dense forest with a TC > 90 %). Both the TC
1726 and H increase with the AGB.

1727

1728

	Ref	CCI Biomass Product Validation and Algorithm Selection Report	
	Issue	Page	Date
	1.0	85	10.02.2019





1729

1730

1731

Figure 46: Sensitivity to Tree cover where the color denotes the forest height (left). On the right with colour expressing different TC

1732

1733

1734

1735

1736

1737

1738

1739

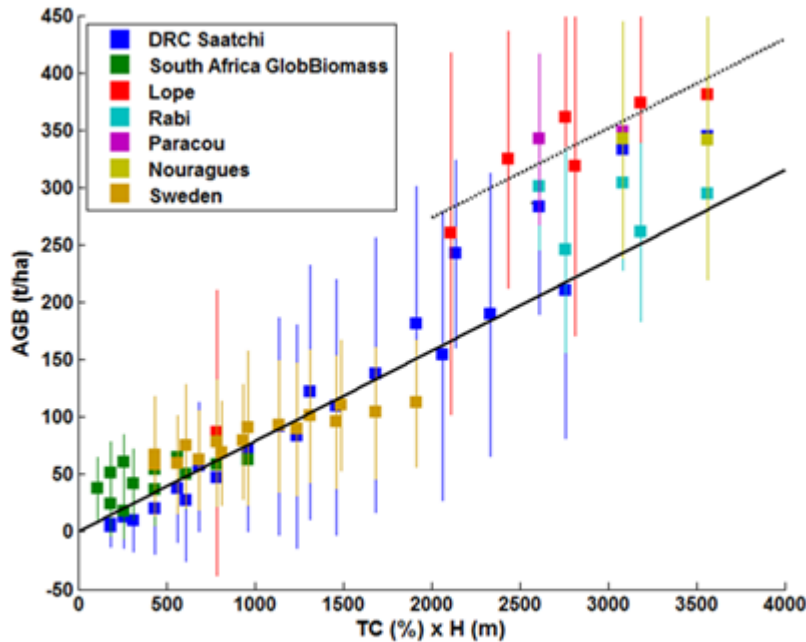
To test the relevance of the findings, the association of different levels of AGB with the structural classes in South Africa, French Guiana (Paracou, Nouragues), Gabon (Lope, Rabi) and Sweden (Nilsson et al., 2016) was investigated (Figure 47). For each structural class, the AGB distribution was represented by the standard deviation. The most striking observation is that, despite a diversity of forests and a large range of AGB, using $TC \times H$ allows 2 main types of canopy to be discriminated at 1 km resolution, with this term high tree cover (> 90 %; with this representing many dense tropical forests), and lower tree cover (< 90 %).

1740

1741

1742

The ability to retrieve AGB in across the range of AGB (including higher levels in the wet tropics) was supported by the correspondence in the AGB estimated using these biophysical variables and based on the VOD (Figure 48).



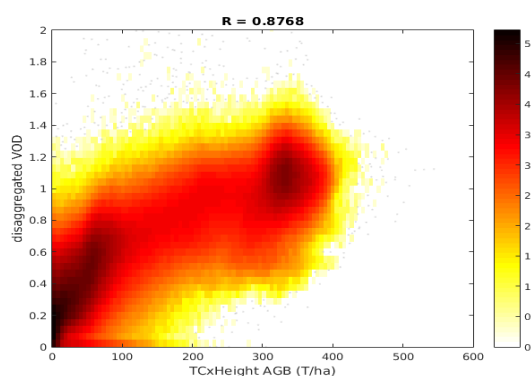
1743

1744

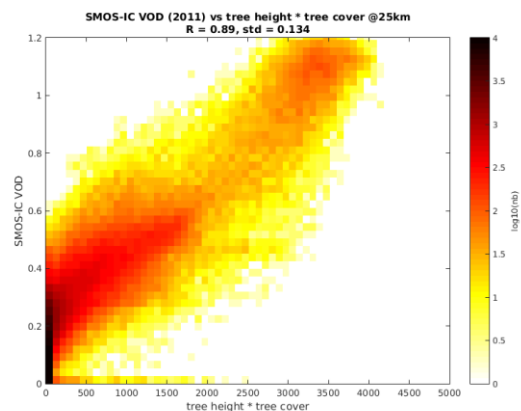
Figure 47: AGB versus volumetric indicator TC(%) x H (m)

1745

a)



b)



1746

Figure 48: The correspondence between VOD (left) and AGB (right) and tree canopy cover (TC, %) x canopy height (H, m) for a) the Congo Basin and b) globally.

1747

1748

By using two regressions relating the product of TC and H to AGB, a global map was produced

1749

(Figure 49a), with subsets generated for South America (Figure 49b) and the DRC (Figure

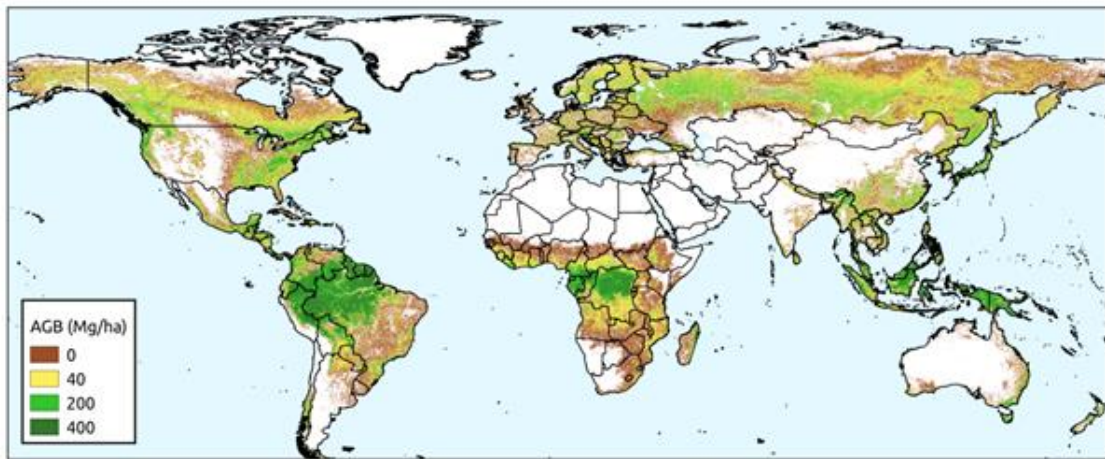
1750

49c). The comparison of the AGB generated from TC and H and by Saatchi et al. (2011; Figure

	Ref	CCI Biomass Product Validation and Algorithm Selection Report		
	Issue	Page	Date	
	1.0	87	10.02.2019	

1751 50) indicated a reduction and increase in that areas previously over and underestimated
1752 using the BIOMASAR algorithm.
1753

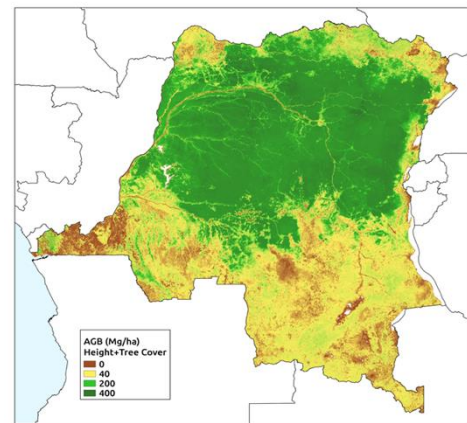
a)



b)



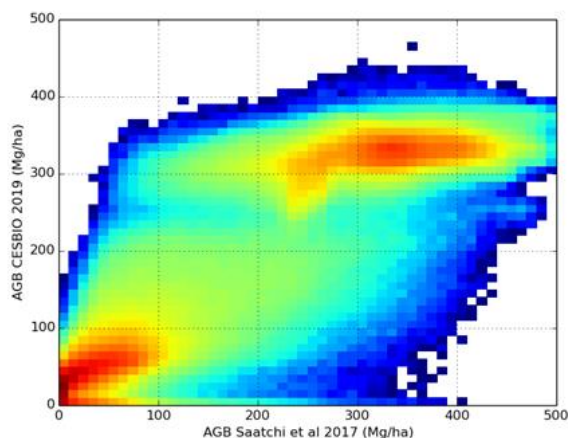
c)



1754 Figure 49: Estimates of AGB generated a) globally and for b) South America and c) the Congo Basin based on
1755 TC and H.

	Ref	CCI Biomass Product Validation and Algorithm Selection Report	
	Issue	Page	Date
	1.0	88	10.02.2019





1756
1757 Figure 50: AGB comparison between TCxH AGB map and the Xu et al. (2017) AGB map obtained for the DRC.

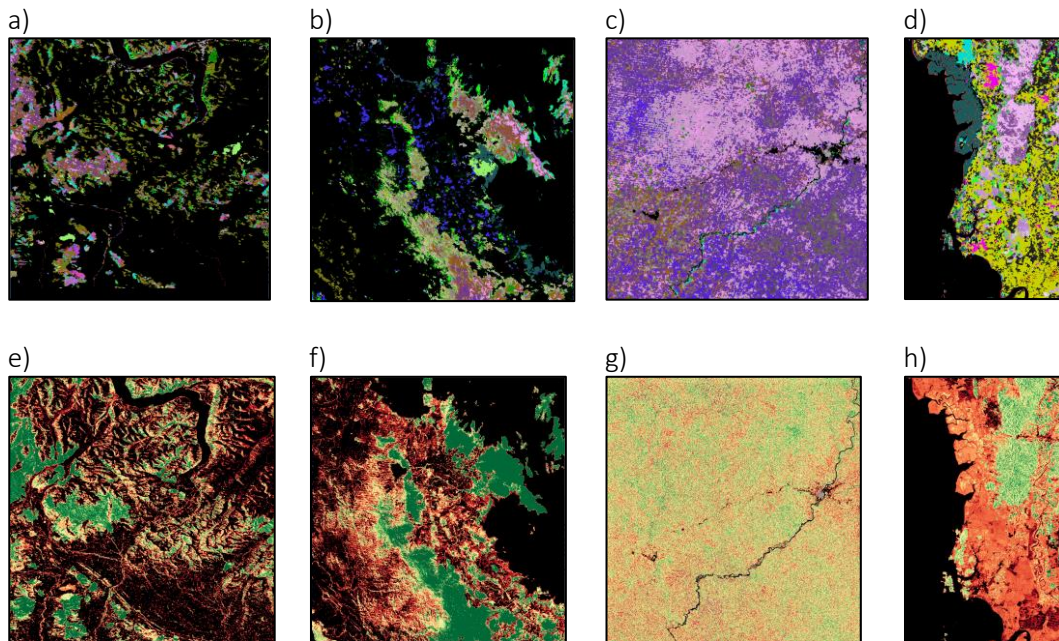
1758 The classification of the global forest area, presented here, relied on data layers derived from
1759 a range of sensors and sources (e.g., Hansen et al., 2013; Simard et al., 2013). However, and
1760 as with Scarth et al. (2018), the classification could be improved by retrieving height and
1761 cover directly from spaceborne LiDAR (i.e., GEDI, ICESAT, ICESAT-2 and/or MOLI) and cover
1762 (also directly) from these same sensors (Scarth et al., 2019). By using spaceborne LiDAR data,
1763 information on the vertical distribution of plant material contained within the volume space
1764 of forests might also be included. Alternative sources of cover information might be the
1765 Sentinel-2 and Landsat-8 optical sensors.

1766
1767 An advancement of approach is to integrate additional environmental information within the
1768 framework of the Food and Agriculture Organisation (FAO) Land Cover Classification System
1769 (LCCS). provides the capacity to describe forests on the basis of their structure (height and
1770 cover) but also other characteristics such as leaf type, phenology and the number and
1771 structural diversity of understorey layers. Lucas and Mitchell (2017) illustrated how such
1772 classifications can be generated for forests and a range of other land covers from a range of
1773 environmental layers (including canopy height and cover) across multiple spatial and
1774 temporal scales. Furthermore, they showed that further descriptions (e.g., tidal or
1775 freshwater inundation) could be provided by introducing additional environmental variables
1776 that were not directly used in the LCCS taxonomy, including plant species, Leaf Area Index
1777 (LAI) and water inundation frequency. The method also allows for the detection and
1778 description of change based on the FAO LCCS taxonomy.

1779

	Ref	CCI Biomass Product Validation and Algorithm Selection Report		
	Issue	Page	Date	
	1.0	89	10.02.2019	

1780 Classifications of the forest area according to LCCS Level 4 are provided in Figure 51 for
1781 selected 1° x 1° tiles, with these conveying a more detailed class description obtained by
1782 combining the information on lifeform, canopy height and cover, and phenology according
1783 to the FAO LCCS Level 4 (modular) taxonomy. All forested segments were provided with a
1784 comprehensive description of the forest and segments with a similar classification were able
1785 to be merged although this compromises the allocation of additional environmental variables
1786 (e.g., burnt area) and leads to loss of information. The classification can be applied at a global
1787 level.
1788



1789 Figure 51. Land cover classification of selected 1 x 1° latitude/longitude tiles for a) Tasmania, b) central north
1790 coastal Queensland, c) central Gabon and d) Perak State, Malaysia with e), f), g) and h) representing the
1791 GlobBiomass AGB maps for 2010. Note that in Malaysia, mangroves are depicted as one class but biophysical
1792 information is contained within the attribute table.

1793
1794
1795
1796
1797
1798
1799

	Ref	CCI Biomass Product Validation and Algorithm Selection Report		
	Issue	Page	Date	
	1.0	90	10.02.2019	

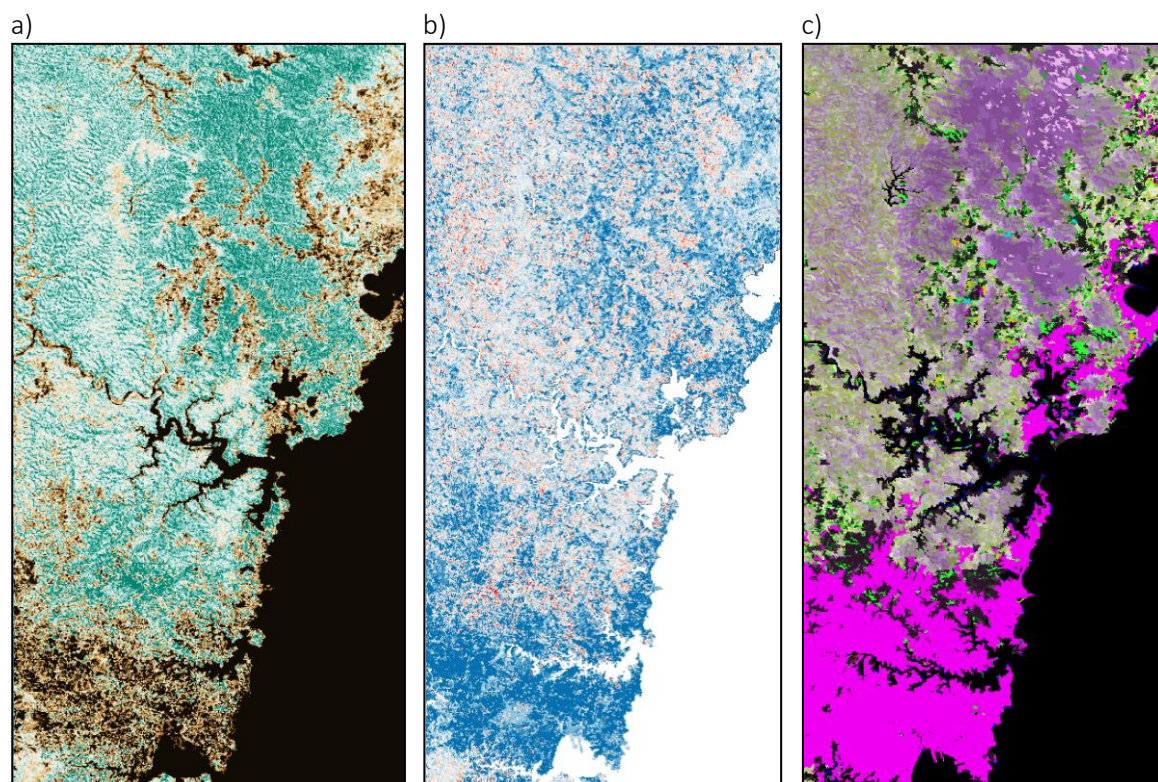
1800 Table 4. List of data layers for reclassification of the global landscape and informing retrieval of AGB.

Layer	SPATIAL		TEMPORAL	
	Extent	Resolution	Frequency	Timing
WWF Biomes	Global	Vector	One date	No year
WWF Ecoregions	Global	Vector	One date	No year
CCI Land Cover	Global	300 m	Annual	
Canopy height (m)	Global	1 km	One date	2005
Canopy cover (%)	Global	30m	One date	2000, 2010, 2015
AG biomass (Mg ha ⁻¹)	Global	50 m	One date	2010
Impervious surface probability (%)	Global	30 m	One date	
Built-up area probability	Global	30m	One date	2010
Elevation	Global	30 m	One date	2007-2010
Slope/Aspect	Global	30 m	One date	2007-2010
Terrain Ruggedness	Global	30 m	One date	2007-2010
Global mangrove extent	Global	25m	Annual-decadal	1996, 2007-10 (annually) and 20015/16
Surface water occurrence	Global	30 m	Summarised	1984-2015
Water seasonality	Global	30m	Summarised	2014-2015
Burn occurrence	Global	250 m	Monthly summary	2000-2012
Snow occurrence	Global	500m	Monthly summary	2000-2012

1801
1802
1803
1804
1805
1806
1807
1808
1809
1810
1811
1812
1813
1814
1815
1816
1817

The value of the FAO LCCS classification is indicated in Figure 52, which illustrate a higher AGB in the forests north of Sydney, Australia, with this corresponding approximately to that obtained through machine learning and with the taller and denser (more closed canopy) forests classified using the FAO LCCS taxonomy. Such classifications can be generated for any location, hence informing the development of the GlobBiomass algorithm. The classes defined according to the FAO LCCS are also relevant in a physical sense with respect to the radar backscatter, as compared to classes such as those associated with GEZ (Simons, 2001), and are relevant to the information provided by optical and LiDAR sensors. More details of the procedures followed are outlined in Lucas et al. (in preparation).

	Ref	CCI Biomass Product Validation and Algorithm Selection Report		
	Issue	Page	Date	
	1.0	91	10.02.2019	



1818 Figure 52. a) GlobBiomass estimate of AGB for Sydney NSW and the northern forests, b) the difference in AGB
1819 estimated using the GlobBiomass product and through machine learning (height and cover) and c) the FAO
1820 LCCS classification indicating areas of taller and denser (closed canopy) forests (dark purple), with these typically
1821 associated with higher AGB in the GlobBiomass product.

1822 5.4 Use of canopy height for mangroves

1823 Using SRTM Digital Surface Model (DSM) data, which was translated to a CHM for mangroves
1824 at sea level, (Simard et al., 2019) produced a global estimate of the AGB of mangrove for
1825 2000. The map was generated by first developing regional and global models (Table 5)
1826 relating field-measured stand (plot) level canopy height to AGB (Mg ha^{-1}), with these fitted
1827 using a regression model of the form:

$$1828 \quad \text{AGB} = a \times H_x^b \quad (14)$$

1830 where H_x represented either H_{ba} (height weighted basal area) or H_{max} (maximum canopy
1831 height) and a and b were allometric parameters. The global model was based on 331 plots
1832 and H_{ba} and regional models were generated for the Americas (n=81), East Africa (n=101)
1833

	Ref	CCI Biomass Product Validation and Algorithm Selection Report		
	Issue	Page	Date	
	1.0	92	10.02.2019	

1834 and South Asia (n=149). Whilst H_x generally explained most variability, the inclusion of stem
1835 density or basal area (as in the case of H_{ba}) improved the region-specific regressions. The
1836 RMSE of the global and regional allometric models for AGB was 54.3 and 103.4 Mg ha⁻¹
1837 respectively.

1838
1839 From these relationships, a global map of AGB was generated by converting the SRTM data
1840 to $SRTMH_{max}$ or $SRTMH_{ba}$ (using field-based measurements; Table 6) and then to AGB,
1841 providing an accuracy of 84.2 Mg ha⁻¹ at the plot level (Figure 53). Aslan et al. (2016) also
1842 provided a conversion from the SRTM H to $SRTM_{HCHM}$. The estimation model was then applied
1843 to mangroves mapped by Giri et al. (2011), who used 2000 Landsat sensor data to produce
1844 a global baseline of mangrove extent (with this corresponding in time with the SRTM
1845 acquisition).

1846
1847 Table 5: Allometric models relating mangrove canopy height metrics (Hx; either Hmax or Hba) to AGB. Simard
1848 et al (2019) used the power equations that did not use Hmax.

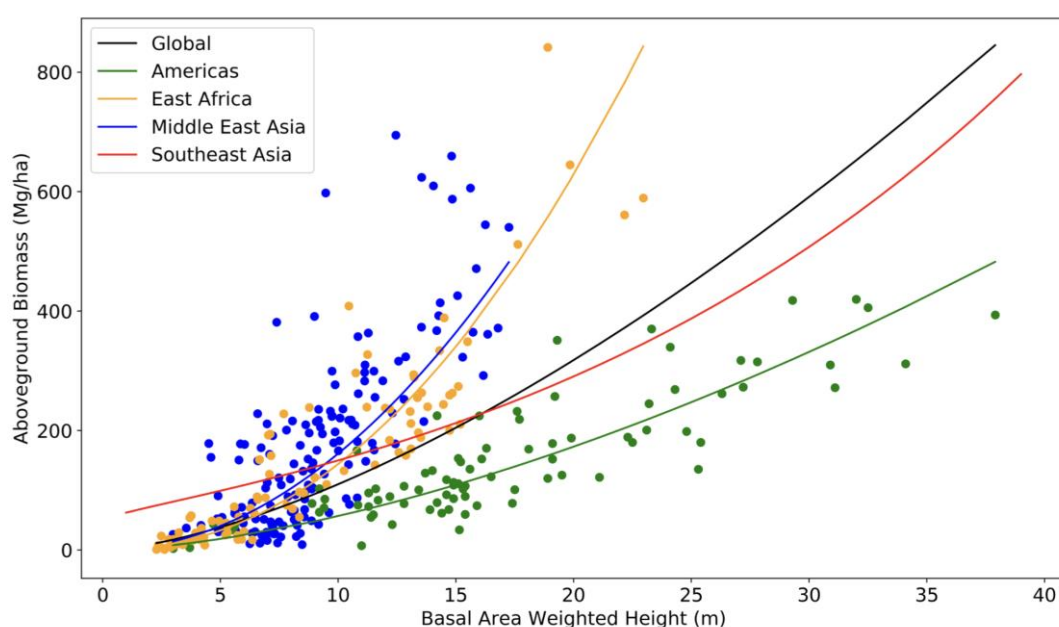
Allometric model	R^2	RMSE (Mg ha ⁻¹)	Allometry name	Region Covered by Model
$AGB = 3.254 \times H_{ba}^{1.5295}$	0.55	134.3	Global generic power	Global
$AGB = 1.066 \times H_{ba}^{2.1295}$	0.84	72.0	East Africa generic power	Somalia to South Africa
$AGB = 1.418 \times H_{ba}^{1.6038}$	0.71	54.3	Americas generic power	North, Central and South America
$AGB = 1.589 \times H_{ba}^{2.0067}$	0.46	103.4	Middle East Asia generic power	Djibouti to Bangladesh
$AGB = \exp(3.9042 + 0.0858 \times H_{CHM})$	0.55	148.0	South East Asia generic power ²	Myanmar to Hawaii
$AGB = 2.572 \times H_{max}^{1.5191}$	0.70	180.0	Global Hmax power	Global
$AGB = 0.440 \times H_{max}^{2.1578}$	0.85	66	East Africa Hmax power	Somalia to South Africa
$AGB = 0.745 \times H_{max}^{1.6228}$	0.70	65	Americas Hmax power	North, Central and South America

1849
1850
1851
1852

1853 Table 6: Allometric equations relating SRTM height data to mangrove canopy height metrics.

Metric	Equation	RMSE	Source
H_{BA}	$SRTM_{Hba} = 1.0754 \times H_{SRTM}$	3.6 m	Simard et al. (2019)
H_{MAX}	$SRTM_{Hmax} = 1.697 \times H_{SRTM}$	5.7 m	
H_{CHM}	$SRTM_{Hchm} = 1.697 \times H_{SRTM}^{0.676}$	3.7 m	Aslan et al. (2016).

1854
1855



1856
1857
1858

Figure 53: The relationship between H_{ba} and AGB (Mg ha⁻¹) established at a global and regional levels (Simard et al., 2019)

1859 A new global baseline of mangrove extent has recently been generated for 2010 using a
 1860 combination of ALOS PALSAR and Landsat sensor data (Bunting et al., 2018; Figure 54).
 1861 Furthermore, changes from this baseline have been mapped using JERS-1 SAR data (for
 1862 1996), ALOS PALSAR (2007, 2008 and 2009) and ALOS-2 PALSAR-2 data (2015/16 with
 1863 additional mapping proposed for 2017/18) and added to or removed from the original
 1864 baseline map to provide new mapping for these years.
 1865
 1866
 1867

	Ref	CCI Biomass Product Validation and Algorithm Selection Report		
	Issue	Page	Date	
	1.0	94	10.02.2019	

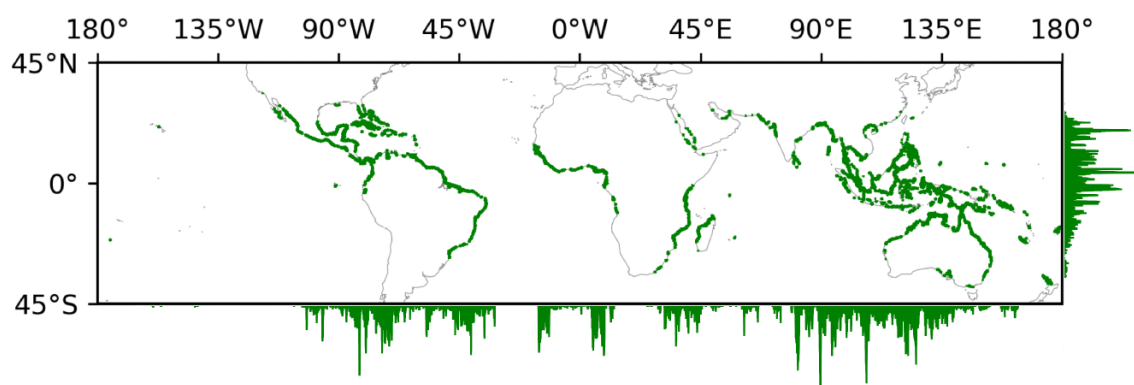


Figure 54: GMW mangrove baseline for 2010 and distribution of mangroves in longitude and latitude (WGS-84; epsg:4326) (Bunting et al., 2010).

1868

1869 These maps are more up-to-date and accurate compared to previous estimates (e.g., Giri et
 1870 al., 2011). As the JAXA 25 m global mosaics were used in their generation, the extent of
 1871 mangroves (for 2010) mapped through the GMW aligns with GlobBiomass product for the
 1872 same year. Future planned iterations (2017, 2018 and 2019) will also align with the CCI
 1873 BIOMASS maps for these years. Changes in mangrove extent between years have also been
 1874 quantified through the GMW and can be used to support the detection of change in AGB (to
 1875 be conducted in Phase 3 of CCI BIOMASS).

1876

1877 To support the global mapping of AGB with CCI BIOMASS, the method of Simard et al. (2019)
 1878 has been reapplied to the SRTM data but within the area defined by the GMW (for 1996)
 1879 with this leading to a revised global AGB estimate. Comparison with the map generated by
 1880 Simard et al. (2019) confirmed production of the same values. Comparison with the existing
 1881 GlobBiomass AGB product within the area mapped in the GMW (in 2010) indicated a
 1882 reasonable correspondence for mangroves below 100 Mg ha^{-1} (Figure 56; which represents
 1883 approximately 50 % of the global estate) but an under representation for those above this
 1884 level (with up to 400 Mg ha^{-1} being typical for most regions with substantive areas of
 1885 mangroves; Figure 56).

1886

1887 The underestimation of AGB is important to address, particularly in countries such as Gabon,
 1888 Equatorial Guinea and the Pacific coast of Columbia, where mangroves support some of the
 1889 highest AGB globally ($> 800 \text{ Mg ha}^{-1}$, with trees approaching or exceeding 60 m in height) as
 1890 a consequence of greater rainfall and lower cyclone activity. Between region and country
 1891 differences were also evident. In Australia and Southeast Asia (Figure 56; b-e), AGB was

	Ref	CCI Biomass Product Validation and Algorithm Selection Report		
	Issue	Page	Date	
	1.0	95	10.02.2019	

1892 consistently underestimated above 100 Mg ha⁻¹ whilst in Africa (f-i) and South America (j-m),
1893 substantial overestimate of AGB was also evident (by several 100 Mg ha⁻¹).

1894

1895 The Australian studies indicate that the reduced L-band HH and, to a lesser extent, HV
1896 backscatter is typically associated with taller ($\geq \sim 10$ m) mangroves dominated by *Rhizophora*
1897 species and that L-band backscatter decreases in proportion to AGB. Hence, one approach
1898 to estimating the AGB of mangroves is to exploit the increase in L-band HH and HV
1899 backscatter with AGB for forests lower than 10 m and the decrease for forests ≥ 10 m using
1900 CHMs generated from interferometric SAR or spaceborne LiDAR (e.g., ICESAT, ICESAT-2 or
1901 GEDI). Knowledge of the distribution of mangroves with and without prop root systems
1902 would be beneficial and could be inferred from the combination of the two datasets.
1903 However, differences in the acquisitions of the required spaceborne datasets together with
1904 variability in the L-band response (particularly in mixed species forests) complicates retrieval.
1905 Hence, the approach recommended here is to use the CHMs directly.

1906

1907

1908

1909

1910

1911

1912

1913

1914

1915

1916

1917

1918

1919

1920

1921

1922

1923

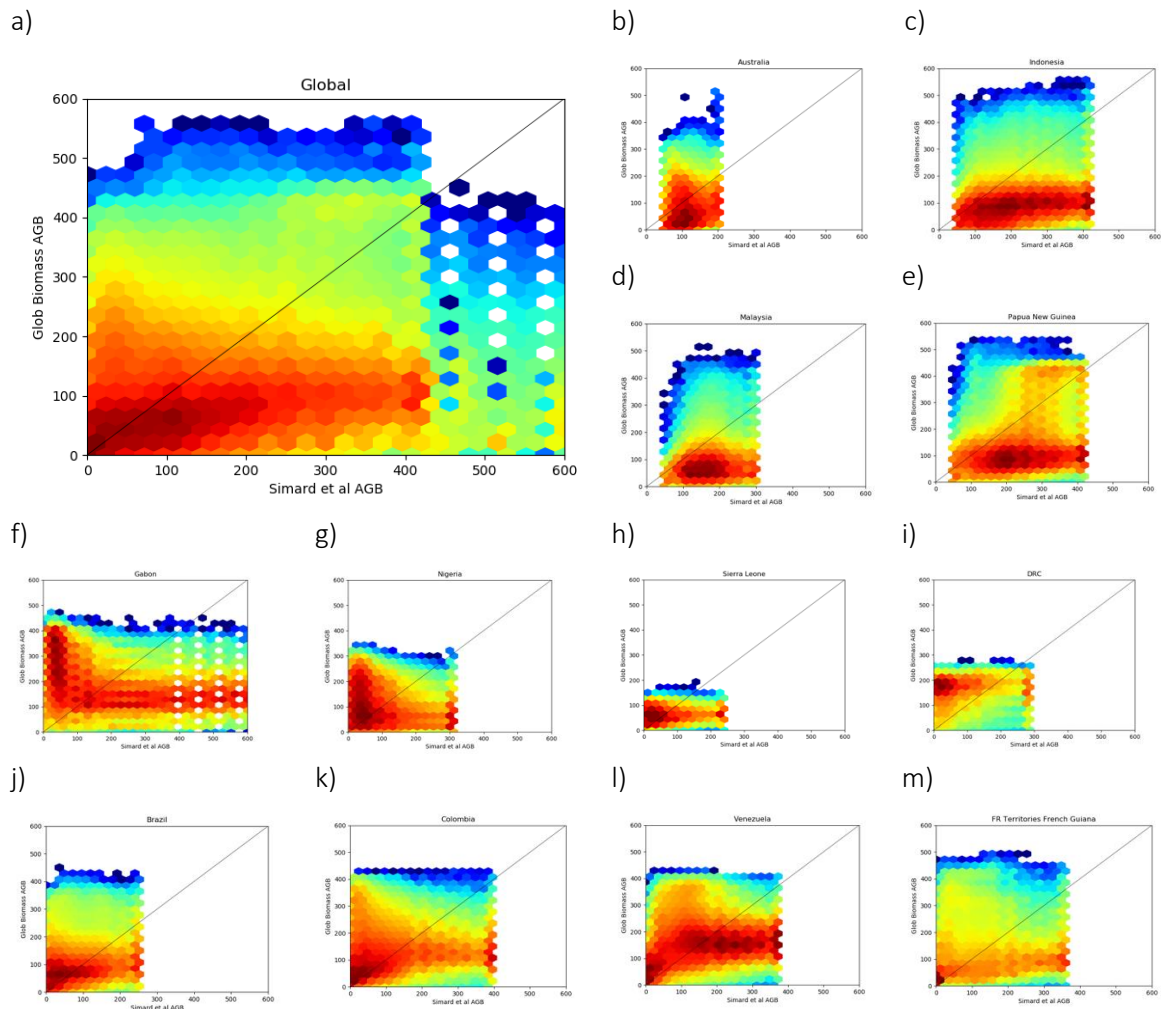
1924

1925

1926

1927

	Ref	CCI Biomass Product Validation and Algorithm Selection Report		
	Issue	Page	Date	
	1.0	96	10.02.2019	



1928 Figure 55: The correspondence between AGB estimated using the BIOMASAR algorithm (GlobBiomass) and
1929 CHMs generated from Shuttle Radar Topographic Mission (SRTM) interferometric SAR (Simard et al., 2019) a)
1930 across their global range (as mapped through the GMW; Bunting et al., 2018) and for b) Australia, c) Indonesia,
1931 d) Malaysia, e) Papua New Guinea, f) Gabon, g) Nigeria, h) Sierra Leone, i) the Democratic Republic of Congo,
1932 j) Brazil, k) Columbia, l) Venezuela and m) French Guyana.

1933
1934 For this reason, the approach suggested by Simard et al. (2019) for the retrieval of global
1935 AGB of mangroves with CCI BIOMASS is to use the estimates of H_{max} and H_{ba} generated using
1936 TanDEM-X (acquired between December 2010 and January 2015) and SRTM data (adjusted
1937 for 2010) and the global and regional equations for retrieving AGB, as developed by Simard
1938 et al. (2019; Table 5). The TanDEM-X Digital Elevation Model (DEM) has been generated
1939 through single pass interferometry using corresponding pairs of images acquired by the
1940 TerraSAR-X and TanDEM-X and is available globally at 90 m spatial resolution (3 arcsec). For

	Ref	CCI Biomass Product Validation and Algorithm Selection Report		
	Issue	Page	Date	
	1.0	97	10.02.2019	

1941 2010, the estimates would be generated within the area of mangroves in 1996 (from JERS-1
1942 SAR but adjusted by considering the 2007 coverage derived from ALOS PALSAR data) and for
1943 2017/18 (using maps generated from ALOS-2 PALSAR-2 data acquired in 2016, 2017 and
1944 2018 respectively when available). Before integration with the CCI Biomass product, a
1945 standard error needs to be calculated that corresponds to the measurement of standard
1946 error from the WCM creating a single unified product. The approach for this is still under
1947 investigation.

1948
1949 The main limitation is that the TanDEM-X and SRTM data were acquired 2/3-7/8 years and
1950 10 years and prior to 2017/18 and 2010 respectively during which growth and loss of
1951 mangroves would have occurred. To some degree, the expansion and clearance of
1952 mangroves (in terms of extent) is captured by the GMW layers generated for 1996, annually
1953 from 2007-10 and for 2015/17. However, growth within existing mangrove areas is less easily
1954 captured.

1955
1956 The approach would be applied only to those areas mapped as mangroves within the GMW
1957 (using data from the most recent year of mapping), with this information fully integrated
1958 within the revised forest classification based on the FAO LCCS approach. The AGB retrieval
1959 algorithm would be applied separately from the GlobBiomass algorithm. A significant
1960 improvement in the retrieval of AGB is expected, as illustrated for the MMFR in Figure 56,
1961 where under-estimation is avoided. The exaggeration of AGB might be, in part, because of
1962 regrowth of forests between 2010 and 2016.

1963

	Ref	CCI Biomass Product Validation and Algorithm Selection Report	
	Issue	Page	Date
	1.0	98	10.02.2019



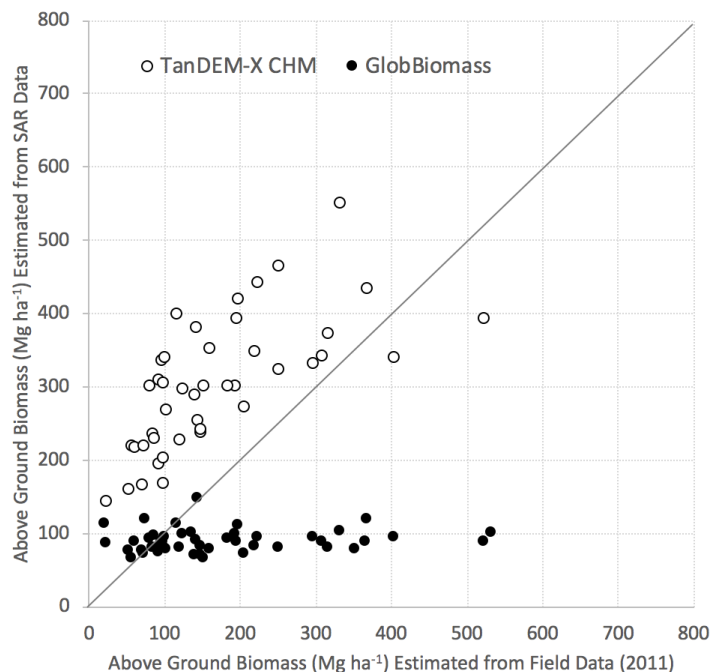


Figure 56: Comparison of field-based estimates of AGB (collected in 2010 and 2011 ; Hamden et al., 2014) and AGB estimated in 2016 from TanDEM and 2010 using the GlobBiomass algorithm.

1964

1965 6 Conclusions and recommendations

1966 To generate annual global estimates of AGB from 2017 to 2020, and refine the 2010
 1967 GlobBiomass AGB product, the ESA's CCI Biomass is advancing the GlobBiomass algorithm by
 1968 considering: the integration of data from other sensors (e.g., spaceborne LiDAR and optical
 1969 data), refining the WCM, incorporating alternative methods in specific areas and the use of
 1970 retrieved environmental variables to improve the characterisation of forests and hence
 1971 retrieval of AGB.

1972

1973 The main weaknesses in the GlobBiomass AGB product are over- and under-estimation of
 1974 AGB in forests with $AGB < 50 \text{ Mg ha}^{-1}$ and in taller denser forest ($> 150 \text{ Mg ha}^{-1}$) respectively,
 1975 associated with: a) variability in ambient conditions and ground surface conditions not taken
 1976 into account by the GlobBiomass algorithm and b) saturation of C- and L-band SAR data at
 1977 relatively low AGB. The broad global distribution of AGB compares well with other regional
 1978 and global estimates but large differences are evident across all forest types as a
 1979 consequence of the different datasets and methods used.

	Ref	CCI Biomass Product Validation and Algorithm Selection Report		
	Issue	Page	Date	
	1.0	99	10.02.2019	

1980

1981 The assumptions used in the current formulation of the WCM need to be reconsidered for
 1982 global applications and where possible, the GlobBiomass algorithm should be improved.

1983 Refinement of the GlobBiomass algorithm can be achieved by reformulating the WCM by
 1984 integrating a soil moisture component, using the temporal trend of ALOS PALSAR
 1985 backscatter, and/or adapting the WCM to retrieve AGB directly.

1986

1987 Alternative methods could also be implemented in areas of high biomass where the WCM is
 1988 under-estimating AGB due to saturation of the radar signals. CCI Biomass are hoping to
 1989 investigate several methods: the backscatter decreasing trend, using SMOS-VOD, applying
 1990 height and cover through structural classification and/or integrating canopy height for
 1991 mangroves.

1992

1993 The global maps of mangrove extent (for 1996, annually from 2007-2010, and 2016/18)
 1994 generated through the Global Mangrove Watch (GMW; Bunting et al., 2019) when used in
 1995 conjunction with Canopy Height Models (CHMs) generated from the SRTM (for 2000; Simard
 1996 et al., 2018) and Tandem-X (2012-2017), provide capacity for quantifying AGB from the CHM
 1997 directly or by combining with L-band backscatter data (particularly at L-band HH) through
 1998 capture of the decreasing trend with AGB for forests typically > 12 m in height.

1999

2000 In many areas of the wet tropics, the increase in woody debris following logging leads to an
 2001 increase in L-band HH and, to a lesser extent, HV σ^0 and hence an overestimation of AGB.
 2002 Whilst individual areas are often small, collectively these often surmount and the total global
 2003 area can be large. These areas are best identified by referencing forest change maps, such
 2004 as those generated through the Global Forest Watch.

2005

2006

2007 7 Appendix 1

2008 For the wet and dry tropics/subtropics and mangroves, *in situ* and LiDAR data were available
 2009 for a variety of sites, but the boreal and temperate forests were under-represented. The
 2010 methods for estimating AGB and the uncertainty of estimation were not always documented,
 2011 which compromised some analyses. For a number of forest inventory plots, the small
 2012 dimensions and the time interval between AGB data estimation and the GlobBiomass epoch
 2013 (2010) make it difficult to have reliable quantitative analysis. For AGB maps derived from *in*
 2014 *situ* and airborne LiDAR data used in this study, errors from different sources propagated in

	Ref	CCI Biomass Product Validation and Algorithm Selection Report		
	Issue	Page	Date	
	1.0	100	10.02.2019	

2015 the map generation procedures have been taken into account. Despite these issues
2016 qualitative analyses was undertaken to investigate causes of errors in the GlobBiomass map
2017 and quantitative assessments of error where possible. The following provides an overview
2018 of the datasets that have been used in the assessment of the GlobBiomass 2010 product.
2019

2020 Reference datasets provided by different groups to assess the performance of the 2010 GlobBiomass product
2021 for Wet Tropics, Dry Tropics, and Boreal /Temperate regions.

Wet Tropics	Dry Tropics and Subtropics	Boreal/Temperate
Mexico: National AGB map (2008) plus national forest inventory data (4-plot clusters, 0.16 ha per cluster) (Leicester University)	In situ data set for southern Africa (>1000 plots) (Edinburgh University)	Wales. 2000 plots available through agreement (Aberystwyth University)
Brazilian Amazon: Tapajos AGB map and field data (0.25 ha plots) (2009) (Leicester University)	South Africa: 1 ha plots LiDAR derived AGB maps (Cesbio, CSIR)	Sweden. Extensive network of plots across the country (Gamma)
Colombia: F2020/IDEAM 2015-16 AGB 30m national map + field data (0.25 ha plots) (Leicester University)	Cameroon: dry forest with 21 1 ha plots (Cesbio)	Finland: Plot data collected by the Natural Resources Institute Finland for 13 different regional forest districts throughout the country (data from 11th NFI measured in 2009-2013, NFI is sampling based, 82,781 plots in total, max. distance to trees in plot is 12.5 m, every 7th tree measured, plots arranged in clusters, avg. Distance between clusters 6-10 km); plot data not directly accessible, map products will be assessed by Natural Resources Institute Finland
Gabon: AfriSAR sites (2015/2016):	Kenya: 2015-16 AGB national map + national forest inventory	Canada: Plot data collected by Pacific Forestry Centre of Natural Resources Canada;

	Ref	CCI Biomass Product Validation and Algorithm Selection Report		
	Issue	Page	Date	
	1.0	101	10.02.2019	

Plots 1 ha at 4 sites (Rabi, Mondah, Mabounie, Lope), LiDAR-based AGB maps (Cesbio)	data (4-plot clusters, 0.28 ha per cluster) (Leicester University)	plot data not directly accessible, map products will be assessed Pacific Forestry Centre
French Guiana: TropiSAR sites (2009): field plots in Paracou (250 x 250 m, 500m x 500m) Nouragues (1 ha), - LiDAR based Paracou and Nouragues maps - P-band tomography-based AGB maps (Cesbio)	Brazil: Cerrado AGB map F2020, field data (~0.1 ha plots) (Leicester University)	Russia: state forest inventory data (FID), attributes of FID are GSV (m ³ /ha) for main stands (per species), regrowth and undergrowth layers attributed by density (pieces per ha), several plots near Krasnoyarsk (92°E,58°N/104°E, 52°N) (FSU)
Malaysia: MAMAForest mangrove sites in 2016. Drone maps of height for 8 1 ha plots (Aberystwyth University)	Guinea-Bissau: 2007-2012, 20-m radius plots (0.13 ha), n = 282, mix of open forest, closed forest, savanna and mangrove (Sheffield University and other contributing institutions)	
Australia: Over 16,000 plots available through the Australian Plant Biomass Facility http://qld.auscover.org.au/public/html/field/ (Aberystwyth University)		
Australia: High resolution LiDAR (< 0.5 m point spacing) and aerial imagery available for mangroves along the coast of Northern Australia (Gulf of Carpentaria) http://wiki.auscover.net.au/wiki/Targeted_Airborne_Data (Aberystwyth University)		
Thailand: Biomass map and 0.1 ha forest inventory plots (Leicester University)		

	Ref	CCI Biomass Product Validation and Algorithm Selection Report		
	Issue	Page	Date	
	1.0	102	10.02.2019	

2023 8 References

- 2024 Amarnath G, Babar S, Murthy MSR (2017) Evaluating MODIS-vegetation continuous field
2025 products to assess tree cover change and forest fragmentation in India – A multi-scale
2026 satellite remote sensing approach. *The Egyptian Journal of Remote Sensing and Space*
2027 *Science*, **20**, 157–168.
- 2028 Archibald, S., Scholes, R., 2007. Leaf green-up in a semi-arid African savanna-separating tree
2029 and grass responses to environmental cues. *Journal of Vegetation Science*, **18**, 583–594.
- 2030 Arnesen, Allan S., Thiago S.F. Silva, Laura L. Hess, Evelyn M.L.M. Novo, Conrado M. Rudorff,
2031 Bruce D. Chapman, Kyle C. McDonald, Monitoring flood extent in the lower Amazon
2032 River floodplain using ALOS/PALSAR ScanSAR images, *Remote Sensing of Environment*,
2033 **130**, 15 March 2013, Pages 51-61, ISSN 0034-4257, 10.1016/j.rse.2012.10.035.
- 2034 Asbridge, E., Lucas, R.M., Ticehurst, C. and Bunting, P. (2016). Mangrove response to
2035 environmental change in Australia’s Gulf of Carpentaria. *Ecology and Evolution*.
2036 10.1002/ece3.2140
- 2037 Askne, J. I., Dammert, P. B., Ulander, L. M., & Smith, G. (1997). C-band repeat-pass
2038 interferometric SAR observations of the forest. *IEEE Transactions on Geoscience and*
2039 *Remote Sensing*, **35**(1), 25-35.
- 2040 Attema, E. P. W., & Ulaby, F. T. (1978). Vegetation modeled as a water cloud. *Radio*
2041 *science*, **13**(2), 357-364.
- 2042 Avitabile V, Baccini A, Friedl MA, Schmillius C (2012) Capabilities and limitations of Landsat
2043 and land cover data for aboveground woody biomass estimation of Uganda. *Remote*
2044 *Sensing of Environment*, **117**, 366–380.
- 2045 Avitabile V, Herold M, Heuvelink GBM et al. (2016) An integrated pan-tropical biomass map
2046 using multiple reference datasets. *Global Change Biology*, **22**, 1406–1420.
- 2047 Böhme, B., Steinbruch, F., Gloaguen, R., Heilmeyer, H., Merkel, B., 2006. Geomorphology,
2048 hydrology, and ecology of Lake Urema, central Mozambique, with focus on lake extent
2049 changes. *Physics and Chemistry of the Earth, Parts A/B/C*, **31**, 745–752.
- 2050 Bouvet, A., Mermoz, S., Le Toan, T., Villard, L., Mathieu, R., Naidoo, L., Asner, G.P., 2018. An
2051 above-ground biomass map of African savannahs and woodlands at 25 m resolution
2052 derived from ALOS PALSAR. *Remote Sensing of Environment*, **206**, 156–173.
- 2053 Bunting, P., Clewley, D., Lucas, R.M. and Gillingham, S., 2014. The remote sensing and GIS
2054 software library (RSGISLib). *Computers & geosciences*, **62**, pp.216-226.
- 2055 Bunting, P., Rosenqvist, A., Lucas, R., Rebelo, L.-M., Hilarides, L., Thomas, N., Hardy, A., Itoh,
2056 T., Shimada, M. and Finlayson, C., 2018. The Global Mangrove Watch—A New 2010
2057 Global Baseline of Mangrove Extent. *Remote Sensing*, **10**(10), 1669.
2058 <http://doi.org/10.3390/rs10101669>
-

	Ref	CCI Biomass Product Validation and Algorithm Selection Report		
	Issue	Page	Date	
	1.0	103	10.02.2019	

- 2059 Bunting, P., Rosenqvist, A., Lucas, R.M., Rebelo, L.M., Hilarides, L., Thomas, N. (2019). How
2060 and Where have the Worlds Mangroves Changed . Nature. In Prep.
- 2061 Carreiras, J.M.B., Vasconcelos, M.J., Lucas, R.M., 2012. Understanding the relationship
2062 between aboveground biomass and ALOS PALSAR data in the forests of Guinea-Bissau
2063 (West Africa). *Remote Sensing of Environment*, 121, 426–442.
- 2064 Cartus, O., Santoro, M., Kellndorfer, J., 2012. Mapping forest aboveground biomass in the
2065 Northeastern United States with ALOS PALSAR dual-polarization L-band. *Remote
2066 Sensing of Environment*, 124, 466–478.
- 2067 Chave, J., Réjou-Méchain, M., Búrquez, A., Chidumayo, E., Colgan, M.S., Delitti, W.B., Duque,
2068 A., Eid, T., Fearnside, P.M., Goodman, R.C. and Henry, M., 2014. Improved allometric
2069 models to estimate the aboveground biomass of tropical trees. *Global Change Biology*,
2070 20, 3177–3190.
- 2071 Clewley, D., Bunting, B., Shepherd, J., Gillingham, S., Flood, N., Dymond, J., Lucas, R.,
2072 Armston, J. and Moghaddam, M. (2014). A python-based open source system for
2073 geographic object-based image analysis (GEOBIA) utilising raster attribute
2074 tables. *Remote Sensing*, 6.
- 2075 Dantas, V., Batalha, M.A. and Pausas, J.G., 2013. Fire drives functional thresholds on the
2076 savanna–forest transition. *Ecology*, 94(11), pp.2454-2463.
- 2077 DiMiceli, C., Carroll, M., Sohlberg, R., Kim, D. H., Kelly, M. and Townshend, J. R. G. (2015).
2078 MOD44B MODIS/Terra Vegetation Continuous Fields Yearly L3 Global 250m SIN Grid
2079 V006 [Data set]. NASA EOSDIS Land Processes DAAC.
- 2080 FAO, 2010. FAO global forest resource assessment 2010. Terms and Definitions. *Working
2081 paper* 144/E(140).
- 2082 Fatoyinbo, T., Feliciano, E., Lagomasino, D., Lee, S.K. and Trettin, C. (2018). Estimating
2083 mangrove above ground biomass from airborne LiDAR data: A case study from the
2084 Zambezi River delta. *Environmental Research Letters*, 13, 025012.
- 2085 Gaughan AE, Holdo RM, Anderson TM (2013) Using short-term MODIS time-series to quantify
2086 tree cover in a highly heterogeneous African savanna. *International Journal of Remote
2087 Sensing*, 34, 6865–6882.
- 2088 Giri, C., Ochieng, E., Tieszen, L.L., Zhu, Z., Singh, A., Loveland, T., Masek, J. and Duke, N., 2011.
2089 Status and distribution of mangrove forests of the world using earth observation
2090 satellite data. *Global Ecology and Biogeography*, 20(1), pp.154-159.
- 2091 Gou, Y., 2017. Analysing the spatial pattern of deforestation and degradation in miombo
2092 woodland: methodological issues and practical solutions. University of Edinburgh.
- 2093 Grace, J., José, J.S., Meir, P., Miranda, H.S. and Montes, R.A., 2006. Productivity and carbon
2094 fluxes of tropical savannas. *Journal of Biogeography*, 33(3), pp.387-400.
- 2095 Hansen, M.C., Potapov, P.V., Moore, R., Hancher, M., Turubanova, S.A.A., Tyukavina, A.,
-

	Ref	CCI Biomass Product Validation and Algorithm Selection Report		
	Issue	Page	Date	
	1.0	104	10.02.2019	

- 2096 Thau, D., Stehman, S.V., Goetz, S.J., Loveland, T.R. and Kommareddy, A., 2013. High-
2097 resolution global maps of 21st-century forest cover change. *science*, 342(6160), pp.850-
2098 853.
- 2099 Haeusler, T., Gomez, S., Siwe, R., Le Toan, T., Mermoz, S., Schardt, M., et al. (2012). Reducing
2100 emissions from deforestation and degradation in africa (reddaf). 7th Research
2101 Framework Programme publication EU Publication: Lets embrace space, 2, (pp. 118–
2102 125).
- 2103 Hu, T., Su, Y., Xue, B., Liu, J., Zhao, X., Fang, J. and Guo, Q. (2016). Mapping global forest
2104 aboveground biomass with spaceborne LiDAR, optical imagery and forest inventory
2105 data. *Remote Sensing*, 8 (565), doi:10.3390/rs8070565.
- 2106 IPCC, 2019. Refinement to the 2006 IPCC Guidelines for National Greenhouse Gas
2107 Inventories.
- 2108 Joshi, N., Mitchard, E. T., Brolly, M., Schumacher, J., Fernández-Landa, A., Johannsen, V. K.,
2109 ... & Fensholt, R. (2017). Understanding ‘saturation’ of radar signals over forests.
2110 *Scientific reports*, 7(1), 3505.
- 2111 Kasischke ES, Tanase MA, Bourgeau-Chavez LL, Borr M (2011) Soil moisture limitations on
2112 monitoring boreal forest regrowth using spaceborne L-band SAR data. *Remote Sensing
2113 of Environment*, **115**, 227–232.
- 2114 Kerr, Y. H., Waldteufel, P., Wigneron, J. P., Delwart, S., Cabot, F., Boutin, J., ... & Juglea, S. E.
2115 (2010). The SMOS mission: New tool for monitoring key elements of the global water
2116 cycle. *Proceedings of the IEEE*, 98(5), 666-687.
- 2117 Komiyama, A., Ong, J. E., & Pongpan, S. (2008). Allometry, biomass, and productivity of
2118 mangrove forests: A review. *Aquatic Botany*, 89, 128–137.
- 2119 Kumar, K., Hari Prasad, K.S., Arora, M.K., 2012. Estimation of water cloud model vegetation
2120 parameters using a genetic algorithm. *Hydrological Sciences Journal*, 57, 776–789.
- 2121 Labriere, N., Tao, S., Chave, J., Scipal, K., Le Toan, T., Abernethy, K., Alonso, A., Barbier, N.,
2122 Bissiengou, P., Casal, T. and Davies, S.J., 2018. *In situ* reference datasets from the
2123 TropiSAR and AfriSAR campaigns in support of upcoming spaceborne biomass
2124 missions. *IEEE Journal of Selected Topics in Applied Earth Observations and Remote
2125 Sensing*, (99), pp.1-11.
- 2126 Lefsky, M.A., 2010. A global forest canopy height map from the Moderate Resolution Imaging
2127 Spectroradiometer and the Geoscience Laser Altimeter System. *Geophysical Research
2128 Letters*, 37(15).
- 2129 Liu, Y. Y., van Dijk, A. I. J. M., de Jeu, R. A. M., Canadell, J. G., McCabe, M. F., Evans, J. P. and
2130 Wang, G. (2015). Recent reversal in loss of global terrestrial biomass. *Nature Climate
2131 Change*, 5, 470-474.
- 2132 Lucas, R.M., Moghaddam, M. and Cronin, N (2004). Microwave scattering from mixed
-

	Ref	CCI Biomass Product Validation and Algorithm Selection Report		
	Issue	Page	Date	
	1.0	105	10.02.2019	

- 2133 species woodlands, central Queensland, Australia. *IEEE Transactions on Geoscience*
2134 *and Remote Sensing*, 2142-2159, October 2004
- 2135 Lucas, R.M., Mitchell, A.L., Rosenqvist, A., Proisy, C., Melius, A. and Ticehurst, C. (2006) The
2136 potential of L-band SAR for quantifying mangrove characteristics and change, Case
2137 studies from the tropics and subtropics, *Aquatic conservation: marine and freshwater*
2138 *ecosystems* - Special Issue: Radar Applications for Wetlands Management 17, 245-264.
- 2139 Lucas R., Armston, J., Fairfax R., Fensham R., Accad A., Carreiras J., Kelley J., Bunting P.,
2140 Clewley D., Bray S., Metcalfe D., Dwyer J., Bowen M., Eyre T., Laidlaw M. and Shimada
2141 M. (2010). An evaluation of the ALOS PALSAR L-band backscatter-above ground
2142 biomass relationships over Queensland, *IEEE Journal of Selected Topics in Applied Earth*
2143 *Observations and Remote Sensing (IEEE JSTARS)* 3, 576- 593
- 2144 Lucas, R.M. and Mitchell, A. (2017). Integrated land cover and change classifications. In: *The*
2145 *Roles of Remote Sensing in Nature Conservation: A Practical Guide and Case*
2146 *Studies* (Eds. Díaz-Delgado, Richard Lucas and Clive Hurford), pp. 295-308.
- 2147 Mayaux, P., Grandi, G. D., Rauste, Y., Simard, M., & Saatchi, S. (2002). Large-scale vegetation
2148 maps derived from the combined L-band GRFM and C-band CAMP wide area radar
2149 mosaics of Central Africa. *International Journal of Remote Sensing*, 23(7), 1261-1282.
- 2150 McNicol, I.M., Ryan, C.M., Mitchard, E.T.A., 2018a. Carbon losses from deforestation and
2151 widespread degradation offset by extensive growth in African woodlands. *Nature*
2152 *Communications*, 9, 3045.
- 2153 McNicol, I.M., Ryan, C.M., Dexter, K.G., Ball, S.M.J., Williams, M., 2018b. Aboveground
2154 Carbon Storage and Its Links to Stand Structure, Tree Diversity and Floristic Composition
2155 in South-Eastern Tanzania. *Ecosystems*, 21, 740–754.
- 2156 Mermoz, S., Réjou-Méchain, M., Villard, L., Le Toan, T., Rossi, V. and Gourlet-Fleury, S., 2015.
2157 Decrease of L-band SAR backscatter with biomass of dense forests. *Remote Sensing of*
2158 *Environment*, 159, pp.307-317.
- 2159 Moncrieff, G.R., Lehmann, C.E., Schnitzler, J., Gambiza, J., Hiernaux, P., Ryan, C.M.,
2160 Shackleton, C.M., Williams, R.J. and Higgins, S.I., 2014. Contrasting architecture of key
2161 African and Australian savanna tree taxa drives intercontinental structural
2162 divergence. *Global ecology and biogeography*, 23(11), pp.1235-1244.
- 2163 Motohka, T., Shimada, M., Uryu, Y., Setiabudi, B., 2014. Remote Sensing of Environment
2164 Using time series PALSAR gamma nought mosaics for automatic detection of tropical
2165 deforestation : A test study in Riau , Indonesia. *Remote Sensing of Environment*, 155,
2166 79–88.
- 2167 Muledi, J.I., Bauman, D., Drouet, T., Vleminckx, J., Jacobs, A., Lejoly, J., Meerts, P. and
2168 Shutcha, M.N., 2016. Fine-scale habitats influence tree species assemblage in a miombo
2169 forest. *Journal of Plant Ecology*, 10(6), pp.958-969.
-

	Ref	CCI Biomass Product Validation and Algorithm Selection Report		
	Issue	Page	Date	
	1.0	106	10.02.2019	

- 2170 Nieto-Quintano, P., Mitchard, E.T.A., Odende, R., Batsa Mouwembe, M.A., Rayden, T., Ryan,
2171 C.M. 2018. The mesic savannas of the Bateke Plateau: carbon stocks and floristic
2172 composition. *Biotropica*.
- 2173 Oiha, N., Merlin, O., Molero, B., Sucre, C., Olivera, L., Rivalland, V. and Er-Raki, S., 2018, July.
2174 Sequential Downscaling of the SMOS Soil Moisture at 100 M Resolution Via a Variable
2175 Intermediate Spatial Resolution. In *IGARSS 2018-2018 IEEE International Geoscience
2176 and Remote Sensing Symposium* (pp. 3735-3738).
- 2177 Paul, K.I., Roxburgh, S.H., Chave, J., England, J.R., Zerihun, A., Specht, A., Lewis, T., Bennett,
2178 L.T., Baker, T.G., Adams, M.A. and Huxtable, D., 2016. Testing the generality of above-
2179 ground biomass allometry across plant functional types at the continent scale. *Global
2180 change biology*, 22(6), pp.2106-2124.
- 2181 Pekel, J.F., Cottam, A., Gorelick, N. and Belward, A.S., 2016. High-resolution mapping of global
2182 surface water and its long-term changes. *Nature*, 540(7633), p.418.
- 2183 Prevot, L., Dechambre, M., Taconet, O., Vidal-Madjar, D., Normand, M., Gallej, S., 1993.
2184 Estimating the characteristics of vegetation canopies with airborne radar
2185 measurements. *International Journal of Remote Sensing*, 14, 2803–2818.
- 2186 Pulliainen, J. T., Heiska, K., Hyyppä, J. and Hallikainen, M. T. (1994). Backscattering properties
2187 of boreal forests at the C- and X-bands. *IEEE Transactions on Geoscience and Remote
2188 Sensing*, 32 (5), 1041-1050.
- 2189 Pulliainen, J. T., Kurvonen, L. and Hallikainen, M. T. (1999). Multitemporal behavior of L- and
2190 C-band SAR observations of boreal forests. *IEEE Transactions on Geoscience and
2191 Remote Sensing*, 37 (2), 927-937.
- 2192 Rauste, Y., 2005. Multi-temporal JERS SAR data in boreal forest biomass mapping. *Remote
2193 Sensing of Environment* 97(2): 263-275.
- 2194 Rejou-Mechain, M., Mortier, F., Barbier, N., Bastin, J.F., Benedetti, C., Bry, X., Chave, J., Cornu,
2195 G., Dauby, G., Doucet, J.L. and Fayolle, A., 2016. Can we predict forest composition
2196 across space and time in Central Africa. ATBC.
- 2197 Rizzoli, P., Martone, M., Gonzalez, C., Wecklich, C., Tridon, D.B., Bräutigam, B., Bachmann,
2198 M., Schulze, D., Fritz, T., Huber, M. and Wessel, B., 2017. Generation and performance
2199 assessment of the global TanDEM-X digital elevation model. *ISPRS journal of
2200 photogrammetry and remote sensing*, 132, pp.119-139.
- 2201 Rodríguez-Fernández, N. J., Mialon, A., Mermoz, S., Bouvet, A., Richaume, P., Al Bitar, A., ...
2202 & Kerr, Y. H. (2018). An evaluation of SMOS L-band vegetation optical depth (L-VOD)
2203 data sets: high sensitivity of L-VOD to above-ground biomass in
2204 Africa. *Biogeosciences*, 15(14), 4627-4645.
- 2205 Rodríguez-Veiga, P., Quegan, S., Carreiras, J., Persson, H.J., Fransson, J.E., Hoscilo, A.,
2206 Ziólkowski, D., Stereńczak, K., Lohberger, S., Stängel, M. and Berninger, A., 2019. Forest
-

	Ref	CCI Biomass Product Validation and Algorithm Selection Report		
	Issue	Page	Date	
	1.0	107	10.02.2019	

- 2207 biomass retrieval approaches from earth observation in different biomes. *International*
2208 *Journal of Applied Earth Observation and Geoinformation*, 77, pp.53-68.
- 2209 Rosenqvist, Å., Forsberg, B. R., Pimentel, T., Rauste, Y. A., & Richey, J. E. (2002). The use of
2210 spaceborne radar data to model inundation patterns and trace gas emissions in the
2211 central Amazon floodplain. *International Journal of Remote Sensing*, 23(7), 1303-1328.
- 2212 Ryan, C.M., Williams, M., Grace, J., 2011. Above-and Belowground Carbon Stocks in a
2213 Miombo Woodland Landscape of Mozambique. *Biotropica*, 1–10.
- 2214 Saatchi, S.S., Harris, N.L., Brown, S., Lefsky, M., Mitchard, E.T., Salas, W., Zutta, B.R.,
2215 Buermann, W., Lewis, S.L., Hagen, S. and Petrova, S., 2011. Benchmark map of forest
2216 carbon stocks in tropical regions across three continents. *Proceedings of the national*
2217 *academy of sciences*, 108(24), pp.9899-9904.
- 2218 Santoro, M., Askne, J., Smith, G., Fransson, J.E.S., 2002. Stem volume retrieval in boreal
2219 forests from ERS-1 / 2 interferometry. *Remote Sensing of Environment*, 81(1), 19–35.
- 2220 Santoro, M., Beaudoin, A., Beer, C., Cartus, O., Fransson, J.E., Hall, R.J., Pathe, C., Schmullius,
2221 C., Schepaschenko, D., Shvidenko, A. and Thurner, M., 2015. Forest growing stock
2222 volume of the northern hemisphere: Spatially explicit estimates for 2010 derived from
2223 Envisat ASAR. *Remote Sensing of Environment*, 168, pp.316-334.
- 2224 Santoro, M., Beer, C., Cartus, O., Schmullius, C., Shvidenko, A., McCallum, I., Wegmüller, U.
2225 and Wiesmann, A., 2011. Retrieval of growing stock volume in boreal forest using hyper-
2226 temporal series of Envisat ASAR ScanSAR backscatter measurements. *Remote Sensing*
2227 *of Environment*, 115(2), pp.490-507.
- 2228 Satalino, G., Balenzano, A., Mattia, F. and Davidson, M.W., 2014. C-band SAR data for
2229 mapping crops dominated by surface or volume scattering. *IEEE Geoscience and Remote*
2230 *Sensing Letters*, 11(2), pp.384-388.
- 2231 Scarth, P., Armston, J., Lucas, R., & Bunting, P. (2019). A Structural Classification of Australian
2232 Vegetation Using ICESat/GLAS, ALOS PALSAR, and Landsat Sensor Data. *Remote Sensing*,
2233 11(2), 147.
- 2234 Sexton, J.O., Song, X.P., Feng, M., Noojipady, P., Anand, A., Huang, C., Kim, D.H., Collins, K.M.,
2235 Channan, S., DiMiceli, C. and Townshend, J.R., 2013. Global, 30-m resolution continuous
2236 fields of tree cover: Landsat-based rescaling of MODIS vegetation continuous fields with
2237 lidar-based estimates of error. *International Journal of Digital Earth*, 6(5), pp.427-448.
- 2238 Shimada, M., Ohtaki, T., 2010. Generating Large-Scale High-Quality SAR Mosaic Datasets:
2239 Application to PALSAR Data for Global Monitoring. *IEEE Journal of Selected Topics in*
2240 *Applied Earth Observations and Remote Sensing*, 3, 637–656.
- 2241 Shimada, M., Itoh, T., Motooka, T., Watanabe, M., Shiraishi, T., Thapa, R., Lucas, R., 2014.
2242 New global forest/non-forest maps from ALOS PALSAR data (2007–2010). *Remote*
2243 *Sensing of Environment*, 155, 13–31.
-

	Ref	CCI Biomass Product Validation and Algorithm Selection Report		
	Issue	Page	Date	
	1.0	108	10.02.2019	

2244 Simard, M., Pinto, N., Fisher, J.B. and Baccini, A., 2011. Mapping forest canopy height globally
2245 with spaceborne lidar. *Journal of Geophysical Research: Biogeosciences*, 116(G4).

2246 Simard, M., Fatoyinbo, L., Smetanka, C., Rivera-Monroy, V. H., Castañeda-Moya, E., Thomas,
2247 N., & Van der Stocken, T., 2019. Mangrove canopy height globally related to
2248 precipitation, temperature and cyclone frequency. *Nature Geoscience*, 12(1), 40–45.

2249 Simons, H. (2001). FRA 2000. Global ecological zoning for the Global Forest Resources
2250 Assessment 2000. FAO, Rome.

2251 Staver, A.C., Archibald, S., Levin, S.A., 2011. The global extent and determinants of savanna
2252 and forest as alternative biome states. *Science*, 334, 230–2.

2253 Thurner, M., Beer, C., Santoro, M., Carvalhais, N., Wutzler, T., Schepaschenko, D., Shvidenko,
2254 A., Kompter, E., Ahrens, B., Levick, S. R. and Schmillius, C. (2014). Carbon stock and
2255 density of northern boreal and temperate forests. *Global Ecology and Biogeography*, 23
2256 (3), 297-310.

2257 Villard, L. and Le Toan, T., 2015. Relating P-Band SAR Intensity to Biomass for Tropical Dense
2258 Forests in Hilly Terrain: *IEEE Journal of Selected Topics in Applied Earth Observations and*
2259 *Remote Sensing*, 8(1), pp.214-223.

2260 Woollen, E., Ryan, C.M., Williams, M., 2012. Carbon Stocks in an African Woodland
2261 Landscape: Spatial Distributions and Scales of Variation. *Ecosystems*.

2262 Xu, H., Steven, M.D., Jaggard, K.W., 1996. Monitoring leaf area of sugar beet using ERS-1 SAR
2263 data. *International Journal of Remote Sensing*, 17, 3401–3410.

2264 Xu, L., Saatchi, S.S., Shapiro, A., Meyer, V., Ferraz, A., Yang, Y., Bastin, J.F., Banks, N., Boeckx,
2265 P., Verbeeck, H. and Lewis, S.L., 2017. Spatial distribution of carbon stored in forests of
2266 the Democratic Republic of Congo. *Scientific reports*, 7(1), p.15030.

2267

2268

2269